TECHNISCHE UNIVERSITÄT WIEN

INSTITUT FÜR MECHANIK UND MECHATRONIK
Mechanics & Mechatronics

Diploma Thesis

Interaction control of a linear motor in a hardware-in-the-loop test rig

conducted in partial fulfilment of the requirements for the degree of a Diplom-Ingenieur
under supervision of

Univ.Prof. Dr. Stefan Jakubek
Institute of Mechanics and Mechatronics
Division for Control and Process Automation

submitted at the TU Wien

Faculty of Mechanical and Industrial Engineering

by

Daniel Duller
Matr.Nr.: 01026778
Missindorfstraße 3/15
1140 Wien

Wien, April 20, 2018   Daniel Duller

Danksagung

Die vorliegende Arbeit bildet den Abschluss meines Studiums an der TU Wien. Deshalb möchte ich an dieser Stelle meinen Dank an alle aussprechen, die mich während dieser Zeit unterstützt haben. Zuallererst danke ich Univ.Prof. Dipl.-Ing. Dr.techn. Stefan Jakubek, unter dessen Schirmherrschaft diese Arbeit entstanden ist.

Ein spezieller Dank gilt meinem Diplomarbeitsbetreuer Dipl.-Ing. Dr.techn. Alexander Schirrer für die inhaltliche Unterstützung während der gesamten Diplomarbeit, sowie Guilherme Aschauer für die Einarbeitung in die Prüfstandssoftware.

Ganz besonders bedanken möchte ich mich auch bei meiner Familie, die mir während des Studium immer den nötigen Rückhalt geboten hat.

Außerdem bedanke ich mich bei meinen Studienkolleginnen und -kollegen, mit denen ich die letzten Jahre über eine schöne Zeit verbringen durfte und die mich immer wieder aufs Neue motiviert haben. Das Forum Schweißkultur sei an dieser Stelle für den regen Input dankend erwähnt.

Zum Schluss möchte ich mich noch persönlich bei Nathalie, Manon, Marion und Wolfgang fürs Korrekturlesen und das wertvolle Feedback bedanken.

Kurzfassung

Diese Arbeit befasst sich mit der Interaktionsregelung eines Linearmotors in einem Hardware-in-the-Loop (HiL) Prüfstand, welcher mit steifen Umgebungen interagieren soll. Das mathematische Modell des Linearmotors berücksichtigt nichtlineare Reibung. In einer theoretischen Studie wurden gebräuchliche Regelalgorithmen auf ihre Realisierbarkeit in einer HiL Umgebung hin untersucht. Dies beinhaltet eine Gegenüberstellung von Impedanz- und Admittanzregelkonzepten mitsamt ihrer Vor- und Nachteile.

Der implementierte Regelalgorithmus besteht aus zwei Regelschleifen. Ein adaptiver Admittanzregler wurde entwickelt, welcher Onlineschätzung der Umgebungsdynamik nutzt, um die Zieldynamik unabhängig von Umgebungssteifigkeit und Abtastzeit zu erhalten. Dazu wurde ein *self-perturbing recursive least squares* Schätzer zur Umgebungsidentifikation implementiert. Der innere Positionsregelkreis wurde als Modellfolgeregler mit Reibungsfeedforward gewählt. Es stellte sich heraus, dass ein linearer Zustandsbeobachter in diesem Aufbau aufgrund der Reibung unzureichende Ergebnisse erzielt. Stattdessen wurde eine Sensorfusionsmethode implementiert, mit welcher eine virtuelle Messung der Geschwindigkeit des Linearmotors möglich ist. Der vorgestellte Ansatz erreicht eine hohe Güte in der Interaktionsregelung und ein vielversprechendes Stabilitätsverhalten und stellt minimale Anforderungen an die Dynamik der virtuellen Umgebung.

Abstract

This thesis deals with interaction control of a linear motor in a hardware-in-the-loop (HiL) test rig that should be able to interact with objects with high contact stiffness. The mathematical model of the linear motor includes nonlinear friction. In the course of a theoretical survey, common control algorithms are assessed for their practicability in a mechanical HiL environment. Impedance- and admittance control concepts are presented with a discussion of their advantages and disadvantages.

The implemented interaction control algorithm consists of two control loops. An adaptive admittance control strategy has been developed, which utilizes online estimation of the environment dynamics to preserve the desired dynamic behaviour independently of environment stiffness and sampling time. A self-perturbing recursive least squares estimator has been used for environment identification. For the inner position control loop, a reference model following controller with friction feedforward was chosen. It has been shown that a state observer delivers unsatisfactory results due to static friction. Instead a sensor fusion approach has been implemented to obtain a virtual velocity measurement with improved accuracy. The proposed approach shows good interaction performance as well as promising stability behaviour, while posing minimal constraints on the choice of virtual environment dynamics.

Contents

List of Figures

Chapter 1

Introduction

Meeting short development cycles and cost effectiveness despite ever increasing complexity of products are key challenges in today's industry. Modern systems engineering relies on concurrent development of different subsystems to address these requirements. Crucial for the success of this approach is the ability to test the interaction between different subsystems at any development step.

Hardware-in-the-loop (HiL) testing is an indispensable method that allows system engineers to evaluate performance and identify technical difficulties early in the development process. The term HiL refers to a procedure, in which the interfaces of a real unit under test are connected to a realtime simulation of its environment with the goal of subjecting the device to a dynamic environment equivalent to the actual operation [1]. By creating such realistic testing, operation states can be examined directly in the laboratory, saving time and costs. Historically, HiL simulations date back to the 1930s, when the first mechanical flight simulators were deployed to aid pilot training [2]. Popularity of the method increased with the evolution of information technologies. Due to the availability of cheap computing power, increasingly complex simulations could be run in real-time [3]. They became a standard tool used by the automotive industry for developing and testing control systems like the *engine control unit* (ECU) and driver assistance systems [4, 5]. Nowadays, HiL simulatons are widely used to emulate both, software and hardware components in the automotive [6, 7] and railway industries [8, 9, 10, 11] as well as in power electronics, robotics and aerospace [12, 13].

In mechanical HiL simulations, actuators are needed as an interface between the physical device and the simulation. It is important to note that the task of the controller is not to make the actuator follow a prescribed motion trajectory. Instead, the interaction between the actuator and the device is regulated. Thus, this control method is known as *interaction control*. The goal of this regulation scheme is to control both, the occurring forces at the contact point *and* the movement of the actuator, so that the interface is consistent with the virtual subsystem's simulation. In the ideal case,

the energy exchanged at the contact interface is exactly the same as in the real interaction scenario. This task turns out to be difficult in practice, especially if the actuator is not tightly coupled to the device, and therefore is only able to apply forces in one direction. Establishing contact can cause large force peaks if the actuator is not able to react swiftly enough, which may result in bouncing. Additionally, actuator dynamics, measurement delays as well as friction and the simulation model itself further complicate the interaction control task, causing undesired interaction and, in the worst case, instability. The challenge for interaction control in this case is to address the problems mentioned without employing an overly conservative system design. If stable interaction can be guaranteed but the actuator does not reflect the simulation anymore, the system loses its practicability in a HiL scenario.

The goal of this thesis is to develop an interaction control strategy for stiff mechanical contacts. In the course of a theoretical survey, the existing interaction control algorithms are evaluated for their practicability in a HiL testing scenario. Possible issues that compromise stability and fidelity of the interaction are identified. Based on the results of this survey, a suitable control strategy is developed with the goal of maximizing the interaction performance while maintaining contact stability. Additionally, the possibility of incorporating information of the environment into the control strategy is investigated. Finally, an adaptive control strategy is developed, which under certain assumptions guarantees stable interaction regardless of sampling time and environment stiffness. To underline the theoretical derivations with experimental data, the resulting control framework is implemented on a mechanical test rig, consisting of a linear motor which can be coupled to various, stiff environments.

1.1 Mechanical HiL Concept and Terminology

This section provides an introduction to the concept of mechanical HiL simulators and the terminology used throughout this thesis. HiL simulation always considers interaction between two or more individual systems, of which some might be replaced by a simulation. An example of a mechanical interaction scenario between a railway pantograph and a catenary is sketched in Figure 1.1a [1]. The contact point between pantograph and catenary forms the interface between the two subsystems. In Figure 1.1b, the real catenary is replaced by a mechanical HiL simulator. To simulate the catenary dynamics, a (dynamic) mathematical model of the real catenary, called the *virtual environment* (VE), must be known. The real device, in this case the pantograph, is referred to as the *unit under test* (UUT). The HiL simulator itself consists of mainly two parts. The first one is the manipulator, which provides the actual physical contact

---

[1]For actual HiL simulators for this scenario, see [14, 8, 9]

(a) Real interaction scenario   (b) HiL Simulation
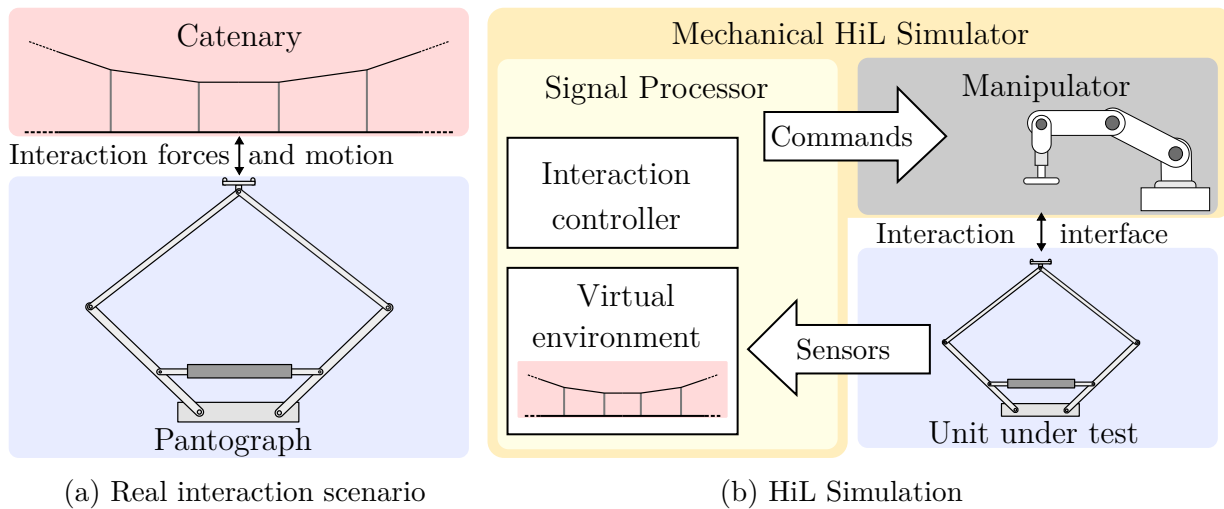
Figure 1.1: Example of a mechanical interaction scenario between a railway
pantograph and the catenary. The two colours in (a) indicate the
two mechanical subsystems involved. The control goal in (b) is to
regulate the manipulator in such a way that the interaction between
UUT and the manipulator behaves the same way as the situation
in (a).

with the UUT. Depending on the task, this can be an industrial robot, a motor, or
any other mechanical actuator. The second part is a signal processor, whose purpose
is to process sensor data, run the simulation of the VE, and control the manipulator
accordingly.

The field of interaction control takes a manipulator centred point of view, as this is
the part which is actually controlled. This perspective is reflected in the terminology
used. The UUT is simply referred to as the *environment* due to the fact that its dynamic
behaviour cannot be influenced by the control engineer. The desired dynamics of the
manipulator are called *virtual environment* in the HiL terminology or sometimes *target
dynamics*. As the focus of this thesis is on interaction control, the according terminology
is used in the following chapters.

1.2 Mechanical Test Rig

A schematic overview of the test rig which is used to perform the interaction experiments
in the course of this thesis is shown in Figure 1.2. A linear motor is used as manipulator.
It is mounted via a guide block to a frame made of aluminium profiles. The guide block
is equipped with ball bearings, allowing the linear motor shafts and the slider to move
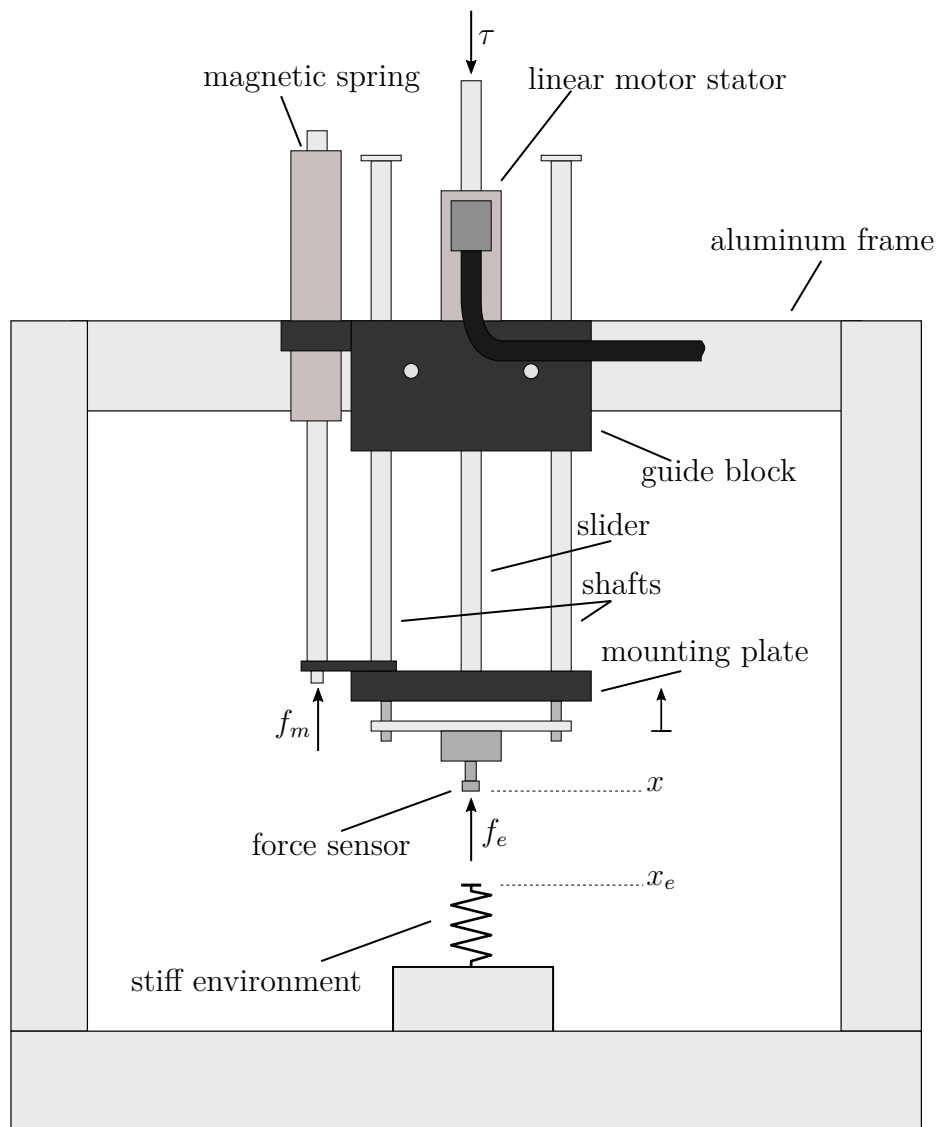
Figure 1.2: Schematic view of the interaction control test rig

in vertical direction. The linear motor can be controlled directly via a desired current that is sent to the motor control unit. The underlying current controller cannot be accessed by the user. A position measurement is provided by the linear motor, which is based on an emulated incremental encoder interface. The manipulator's counterpart is a small platform, on which different test objects like a steel spring can be placed as examples of elastic environments with various magnitudes of contact stiffness. In order to measure the contact force, a force sensor is attached to the linear motor via a mounting plate. Its tip is also the contact interface to the environment. In the next section, the structure of the thesis is outlined. System identification of the manipulator is the topic of the next chapter.

1.3 Outline of the Thesis

The remainder of this thesis is organized as follows. Chapter 2 deals with mathematical modelling and system identification and is divided into two sections. The first section covers identification of the linear motor, which is done offline. It turns out that it is subject to considerable friction forces. Selecting a practical model and describing the friction identification procedure makes up the majority of the section. The second part briefly deals with online estimation of the environment. Chapter 3 introduces the theoretical background of interaction control. Based on linear-dynamic models, the advantages and disadvantages of the existing impedance- and admittance control approaches are highlighted. Additionally, the effects of friction and sampling on the interaction control are analyzed. Based on the results, in Chapter 4 a position-based admittance control approach for linear linear-dynamic, virtual environments together with an underlying position controller based on a reference model following state space controller is developed. Additionally, a feedforward friction compensation method is derived according to the identification results of Chapter 2. To maximize the performance of the admittance control approach, an adaptive admittance control approach is presented, which utilizes online identification of the environment to shape the virtual environment transfer function accordingly. Chapter 5 deals with the implementation and shows a method to incorporate an acceleration sensor to the control approach to minimize friction influence. Experimental results for the position controller and for the admittance control loop are presented in Chapter 6. Additionally, the influence of different friction feedforward methods on the admittance control performance are highlighted. The thesis closes with an outlook and a listing of possible further improvements of the control method in Chapter 7.

Chapter 2

System Modelling and Identification

In this chapter, a mathematical model for the mechanical test rig, shown in Figure 1.2, is derived. At first a linear model for the manipulator is formulated. It is extended with a static friction model. As the environment's properties are a priori unknown, the second part of this chapter covers online identification.

2.1 Linear Motor Model

The manipulator is actuated by an electromagnetic direct drive linear motor. It consists of an electrical and a mechanical subsystem to be modelled. The motor is driven in *current command mode*, which means that a desired stator winding current i_d can be provided to the linear motor interface. An subsequent current control loop regulates the winding current i to the desired value. To derive the relationship between desired current and the force τ produced by the linear motor, two assumptions are made:

- The settling time of the internal current controller is much smaller than the time constant of the mechanical subsystem.

- The relationship between current and force is independent of the slider position and velocity.

As a result of the first assumption, the dynamics of the current control loop can be neglected, and $i \approx i_d$ holds. If the second assumption holds, the force results as a linear function of the desired current to $\tau = -K_i i_d$ with the linear motor constant K_i. Hence, the electric subsystem reduces to a simple proportional element [15].

All moving parts, the slider, shafts, mounting plate, the magnetic spring and the force sensor are screwed tightly together and can be modelled as a concentrated mass m. On the contact interface between the shafts and the ball bearings in the guide block naturally friction occurs. Its linear contribution is included in the lumped parameter
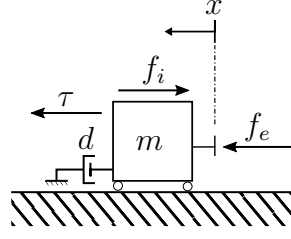
Figure 2.1: Lumped element model of the linear motor.

model as the viscous friction component d. The remaining forces acting on the manipulator are divided into the internal disturbance force f_i and the external force f_e that occurs on the contact interface with the environment. This distinction is made because f_e can be measured and compensated, while this is not the case for f_i. The internal disturbances are defined as

$$f_i = \underbrace{mg - f_{mag}}_{-f_g = \text{const}} + f_f \quad , \tag{2.1}$$

and include the constant gravitational force mg, the gravitation compensation f_{mag} and the nonlinear friction f_f. As f_{mag} does not exactly compensate mg, a constant difference $-f_g$ can be observed. As f_g is smaller than the static friction force, the linear motor does not move when $i_d = 0$. The equation of motion results to

$$m\ddot{x} = -dv - K_i i_d + f_e - f_i \quad , \tag{2.2}$$

which is illustrated using a lumped element model in Figure 2.1

Introducing the state vector $\mathbf{x}^{\mathrm{T}} = \begin{bmatrix} x & v \end{bmatrix}$, the state space representation

$$\dot{\mathbf{x}} = \underbrace{\begin{bmatrix} 0 & 1 \\ 0 & -\frac{d}{m} \end{bmatrix}}_{\mathbf{A}} \mathbf{x} + \underbrace{\begin{bmatrix} 0 \\ -\frac{K_i}{m} \end{bmatrix}}_{\mathbf{B}} \underbrace{i_d}_{u} + \underbrace{\begin{bmatrix} 0 \\ \frac{1}{m} \end{bmatrix}}_{\mathbf{E}} \underbrace{(f_e - f_i)}_{f_d} \quad , \tag{2.3}$$

is obtained. $\mathbf{A}$ denotes the system matrix, $\mathbf{B}$ is the input matrix, u represents the control input, $\mathbf{E}$ is the disturbance input matrix for the disturbance force f_d. (2.3) suggests that the linear motor can be described by a second-order linear model. The actual linear motor used in this thesis is subject to considerable friction forces, which makes it necessary to further refine its mathematical model. The selection of a suitable friction model is the subject of the following section.

2.1.1 Friction Models

When two mechanical components are in contact and move relative to each other, friction phenomena can be observed. It can cause undesirable effects in control loops

like tracking errors and limit cycles [16]. Although friction is dissipative, its presence can destabilize a force control loop under certain conditions [17]. Therefore special care has to be taken to minimize these negative effects on the control system.

The mechanisms that cause friction take place on a microscopic scale and are quite sophisticated [18, 11ff]. For control design exclusively macroscopic models are practicable. Literature mainly distinguishes between static and dynamic models [19]. The latter offer a better description of the effects in the low- and zero-velocity regime at the cost of introducing new states rendering parameter estimation more difficult [20, 21]. Additionally, the dynamic models often result in stiff differential equations. To solve them on the real-time hardware, special care must be taken [22]. These drawbacks outweigh the potential performance benefits of using a dynamic model. Therefore in this thesis static friction models are utilized. The most simple static model is the well known Coulomb friction model

$$f_f(v) = f_c \operatorname{sign}(v) \quad , \tag{2.4}$$

where the signum function $\operatorname{sign}(\cdot)$ is defined as

$$\operatorname{sign}(x) = \begin{cases} 1 & x > 0 \\ 0 & x = 0 \\ -1 & x < 0 \end{cases} \quad . \tag{2.5}$$

The Coulomb friction f_c depends on the normal force between the surfaces in contact and is also known as kinetic or dynamic friction. It has the distinct property that it is independent of the velocity. Despite being a very rough approximation of the phenomenon, the Coulomb friction model is successfully used to design feedforward compensators [23, 24].

It has been observed that a larger force than the Coulomb friction is necessary to initiate motion on a resting body. This phenomenon is called *static friction* or *stiction*. Additionally, for lubricated contacts the friction force decreases from the static friction force to the Coulomb friction if the velocity increases [25]. This is behaviour called the *Stribeck effect*. A common static model that incorporates the Stribeck effect is given with

$$f_f = \begin{cases} f(v) & v \neq 0 \\ f_e & (v = 0) \wedge (|f_e| < f_s) \\ f_s \operatorname{sign}(f_e) & \text{else} \end{cases} \tag{2.6a}$$

$$f(v) = \operatorname{sign}(v) \left(f_c + (f_s - f_c) e^{-\left| \frac{v}{v_s} \right|^\delta} \right) \quad , \tag{2.6b}$$

with f_s as the peak static friction force, v_s the Stribeck velocity and δ as form factor [20]. f_e in this case refers to the total external force exerted on the body. The last two lines in (2.6a) account for the fact that contrary to the suggestion of (2.4), the friction at zero velocity is not zero, but exactly compensates the external force f_e. Hence, a body does not start to move if a smaller force than the static friction force is applied [18, p. 39].

2.2 Identification Strategy

From the linear motor model (2.3), the corresponding transfer function from current input i_d to position output x can be immediately derived

$$G_m(s) = -\frac{K_i}{s\,(ms + d)} \quad . \tag{2.7}$$

The plant has integrating behaviour, which renders open loop identification a difficult task. Additionally, when exciting the linear motor in open loop, the plant dynamics are masked by friction. The influence of friction also leads to unsatisfactory identification results using closed-loop identification techniques. Instead, the approach was chosen to identify some plant parameters independently offline and then to use the partial knowledge to identify the rest of the system. The linear motor constant K_i can be directly found in the data sheet. m can also be determined offline, by weighing the moving components. The constant gravitational force f_f follows directly. Knowing these parameters, the friction parameters can be identified in closed-loop experiments.

2.2.1 Friction Identification

Before conducting closed loop experiments, the friction forces acting on the linear motor are investigated qualitatively. For this purpose, the force is measured with the sensor mounted on the manipulator while the linear motor is turned off and moved manually with approximately constant velocity. The equation of motion (2.2) with $i_d = 0$ can be rearranged to

$$f_e = m\ddot{x} + dv + f_i \quad . \tag{2.8}$$

Correcting the measured data for the inertia forces reveals the friction forces. Figure 2.2 shows the force needed to move the linear motor with approximately constant speed in the range $-5\ldots5\,\mathrm{cm}$. An asymmetric Coulomb friction component can be seen with a larger friction force when the linear motor is moved downwards. This can be contributed to the gravitational force f_f. Furthermore, a cogging force component with a periodicity
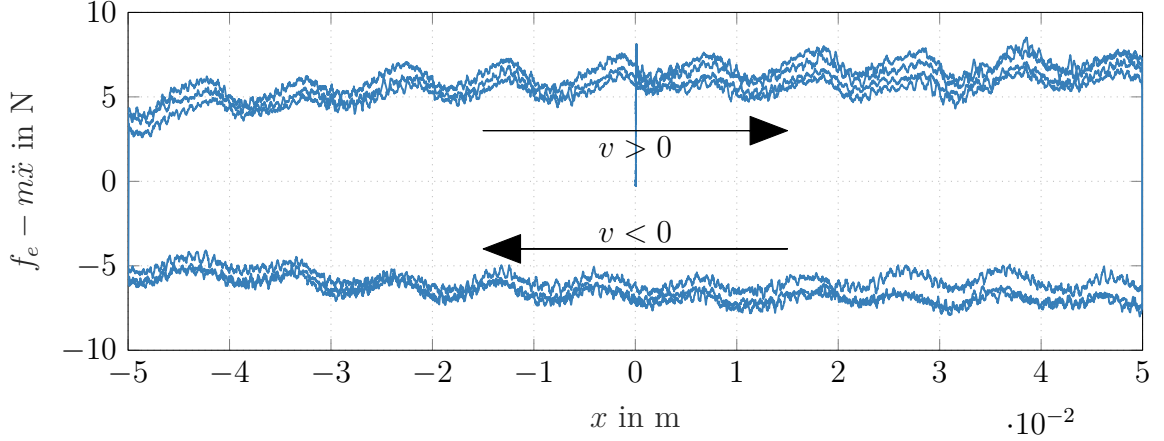
Figure 2.2: Inertia compensated force $f_e - m\ddot{x}$ as a function of the manipulator position x when the linear motor is moved by hand with approximately constant velocity.

of roughly $1\,\mathrm{cm}$ is observed. At last for $x < 0$, the maximum friction depends on the position. A possible explanation for this effect is found in the mechanical construction of the test rig. As the linear motor is moved upwards, the slider of the magnetic spring dips deeper into the stator, thus increasing the contact surface and therefore the friction.

In order to fit a static friction model, as a next step a friction-velocity map was recorded around the origin of the manipulator workspace. The position control loop was closed and the linear motor was commanded to move trajectories of piecewise constant velocities

$$x_d(t) = x_{triag}(t - kT) \quad \forall t \in [kT, (k+1)T) \quad , \tag{2.9}$$

around the origin of the workspace. T is the period of one triangle and $k = 0, 1, 2, \ldots$. One period of the triangle signal is defined as

$$x_{triag}(t) = \begin{cases} -\Delta x + \dfrac{4\Delta x t}{T} & t < \dfrac{T}{2} \\ \Delta x - \dfrac{4\Delta x t}{T} & t \geq \dfrac{T}{2} \end{cases} . \tag{2.10}$$

When assuming an ideal position control loop, the resulting velocity

$$v = \pm\frac{4\Delta x}{T} \tag{2.11}$$

is constant in each half of a period. It can be set to a specific value by choosing T appropriately. In this experiment, no external force acts on the manipulator. Hence,
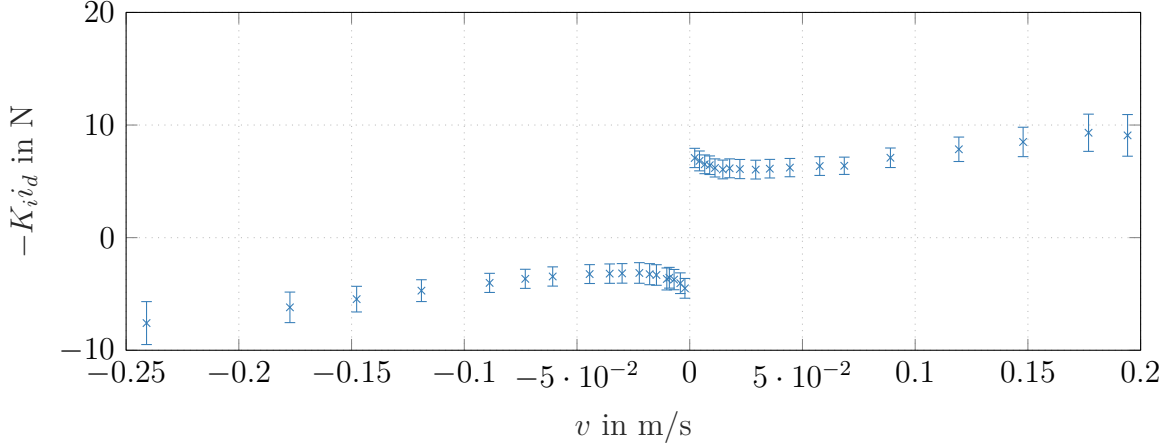
Figure 2.3: Disturbance force $K_i i_d$ and standard deviation for different constant velocities averaged over all positions in the interval $[-\Delta x, \Delta x]$ for $\Delta x = 4\,\mathrm{cm}$.

(2.2) reduces to

$$K_f i_d = -dv - f_g - f_f \quad , \tag{2.12}$$

where all unknown parameters appear on the right-hand side. Figure 2.3 shows the disturbance forces, averaged over the whole workspace, as well as their standard deviation, when the linear motor is made to follow triangle trajectories with different period lengths T. For small velocities the deviations arise mainly from cogging. Additionally, Stribeck and viscous friction components can be seen. The static friction model (2.6) is adapted to

$$f_f(v) = \left(f_c + f_{s,a} e^{-\left| \frac{v}{v_s} \right|} \right) \frac{2}{\pi} \arctan\left(k_{tan} v \right) \quad . \tag{2.13}$$

to describe the observed friction. To account for the exponential decay, seen in Figure 2.3, the form factor $\delta = 1$ is chosen in (2.13). The parameter $f_{s,a}$ is the amplitude of the Stribeck friction $f_s - f_c$. In order to obtain a continuous friction velocity map, the term $\frac{2}{\pi} \arctan(k_{tan} v)$ where $k_{tan} >> 1$ is introduced as an approximation of the sign$(\cdot)$. Substituting (2.13) into (2.12) yields

$$K_i i_d = -dv - f_g + - \left(f_c + f_{s,a} e^{-\left| \frac{v}{v_s} \right|} \right) \frac{2}{\pi} \arctan\left(k_{tan} v \right) \quad , \tag{2.14}$$

from which follows the parameter vector

$$\mathbf{p}_f^{\mathrm{T}} = \begin{bmatrix} d & f_g & f_c & f_{s,a} & v_s \end{bmatrix} \tag{2.15}$$
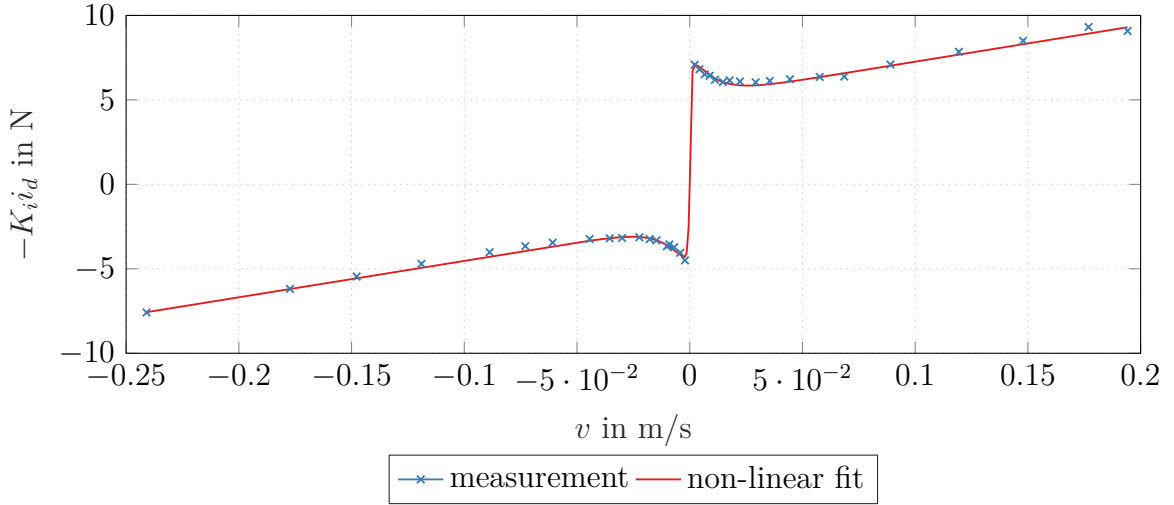
Figure 2.4: Average friction force for different velocities and fitted static friction model together with viscous friction and gravity terms (2.14). Result parameters can be found in Table B.2.

of the five unknowns to be estimated. In order to find a parameter set $\hat{\mathbf{p}}_f$ that minimizes the squared error between the measured linear motor force $K_i i_d$ and the disturbance forces

$$\min_{\mathbf{p}_f} J(\mathbf{p}_f) = \sum_{i=1}^{N_m} \left(f_{meas,i} - f_{mod}(v_i, \mathbf{p}_f) \right)^2 \tag{2.16}$$

can be formulated, where N_m is the number of measurements with different velocites v_i, $f_{meas,i} = K_f i_{d,i}$ from (2.12) and $f_{mod}(v_i, \mathbf{p}_f)$ is the right-hand side of (2.14). It is evident that (2.16) is nonlinear in the friction parameters. A local solution can be found, for example by using the Simplex algorithm [26]. The result is visualized in Figure 2.4, and the corresponding numerical values are listed in Table B.2.

2.3 Online Environment Identification

In order to optimize the interaction control strategy it is desirable to incorporate environment parameters into the control design. In typical interaction control scenarios, the environment dynamics are unknown beforehand or are subject to change in time, for example when a robot touches different surfaces. In these scenarios, online parameter estimation techniques may be employed to achieve this task. A suitable environment model must be taken as basis for identification. An approach often employed is to

model the contact forces

$$f_e = \begin{cases} k_e \left(x_e - x \right) - d_e v & x < x_e \\ 0 & \text{else} \end{cases} \quad . \tag{2.17}$$

with an ideal static stiffness k_e and a damping factor d_e [27, 28]. x_e is the position of the contact point to the environment, when it is in resting position. One limitation of the simple environment model (2.17) can be observed for $v > 0$ as the contact is loosened. In that case $f_e < 0$ is possible which can be interpreted in a way that environment damping prevents uncoupling. This behaviour does not conform with experimental data. To describe the contact force more accurately, including $f_e = 0$ for $x_e - x = 0$, the nonlinear *Hunt-Crossley model* can be used [29].

In order to select an appropriate environment model, contact experiments were performed between the position-controlled linear motor and a steel spring. Figure 2.5 shows that the force on the contact interface between linear motor and spring is in good approximation a linear function of the penetration depth $x_p = x_e - x$. Hence, the environment is modelled as a linear spring resulting from (2.17) with $d_e \approx 0$. This simplification has no impact on the difficulty of the identification problem, but simplifies theoretical considerations in the following chapters. Furthermore, a static stiffness as an environment is of special interest. From the interaction control point of view it represents a worst case environment due to the lack of damping, which is useful to dissipate excess energy from imperfect control behaviour. If x_e is known, the estimation problem for k_e at a time index k

$$y_k = s_k p_k \tag{2.18}$$

where

$$y_k = f_{e,k} \tag{2.19}$$

$$s_k = x_e - x_k \tag{2.20}$$

$$p_k = k_{e,k} \tag{2.21}$$

becomes linear. Hence, well established means of linear regression can be used to obtain an estimate $\hat{k}_e$ of the actual stiffness.

Values of k_e that occur in actual interaction tasks may differ in several orders of magnitude. The estimation algorithm should therefore be able to react reasonably fast if the manipulator touches stiff and soft surfaces. A possibility to meet this requirement
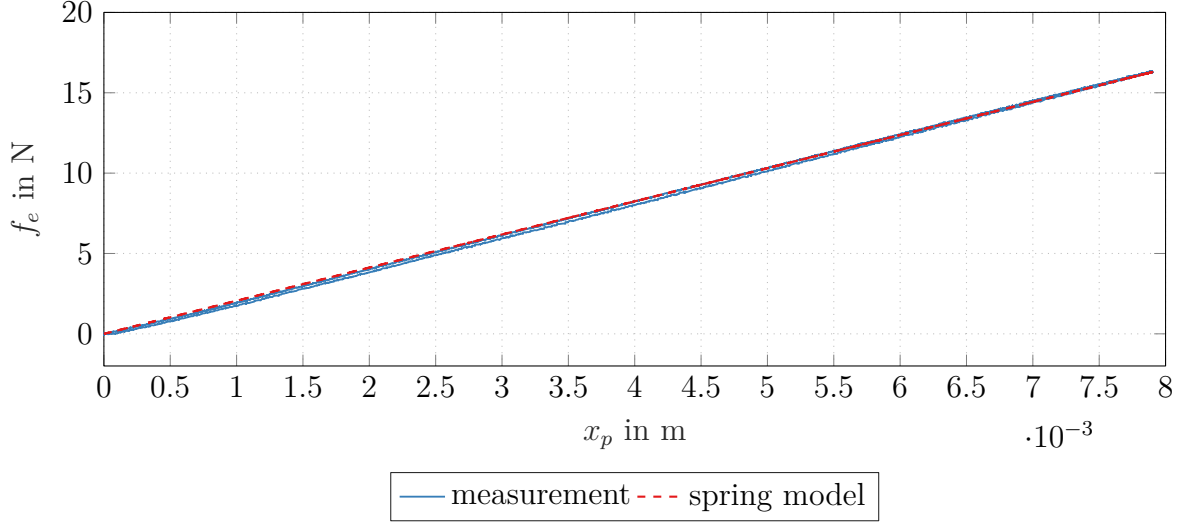
Figure 2.5: Measured force over penetration depth $x_p = x_e - x$ for a steel spring compared to a contact model consisting of an ideal stiffness $k_e = 2061.18\,\text{N/m}$ only.

is the *selfperturbing recursive least squares* (SPRLS) algorithm

$$\mathbf{k}_k = \frac{\mathbf{P}_{k-1}\mathbf{s}_k}{1 + \mathbf{s}_k^{\mathrm{T}}\mathbf{P}_{k-1}\mathbf{s}_k} \tag{2.22a}$$

$$\mathbf{P}_k = \left(\mathbf{P}_{k-1} - \mathbf{k}_k\mathbf{s}_k^{\mathrm{T}}\mathbf{P}_{k-1}\right) + \beta\left[\gamma e_{k-1}^2\right]\mathbf{I} \tag{2.22b}$$

$$\hat{\mathbf{p}}_k = \hat{\mathbf{p}}_{k-1} + \mathbf{k}_k\left(y_k - \mathbf{s}_k^{\mathrm{T}}\hat{\mathbf{p}}_{k-1}\right) \tag{2.22c}$$

proposed by Park and Jun [30]. $\mathbf{P}_k$ and $\mathbf{k}_k$ represent the estimation covariance matrix and the estimation update vector respectively. $\hat{\mathbf{p}}_k$ is the estimate of the parameter vector $\mathbf{p}_k$ at the current time index. The parameters β and γ are design constants, e_k is the *a posteriori error*, defined as

$$e_k = y_k - \mathbf{s}_k^{\mathrm{T}}\hat{\mathbf{p}}_k \tag{2.23}$$

and $\mathbf{I}$ is the identity matrix. The rounding operator $[\alpha]$ returns the nearest integer value of α. Thus (2.22b) shows that $\mathbf{P}_k$ is increased by the factor $\beta\left[\gamma e_{k-1}^2\right]$, if the weighted squared estimation error γe_{k-1}^2 rises above 0.5. Compared to the traditional RLS algorithm with a forgetting factor, $\mathbf{P}_k$ is only increased once the estimation error grows too large, resulting in a better noise rejection when $\mathbf{p}_k$ is constant over time. Figure 2.6 shows the effectiveness of the SPRLS algorithm to adapt to parameter changes. In this experiment the manipulator is position-controlled to approach two objects of different stiffness. The evolution of the online estimate of k_e is shown and compared to
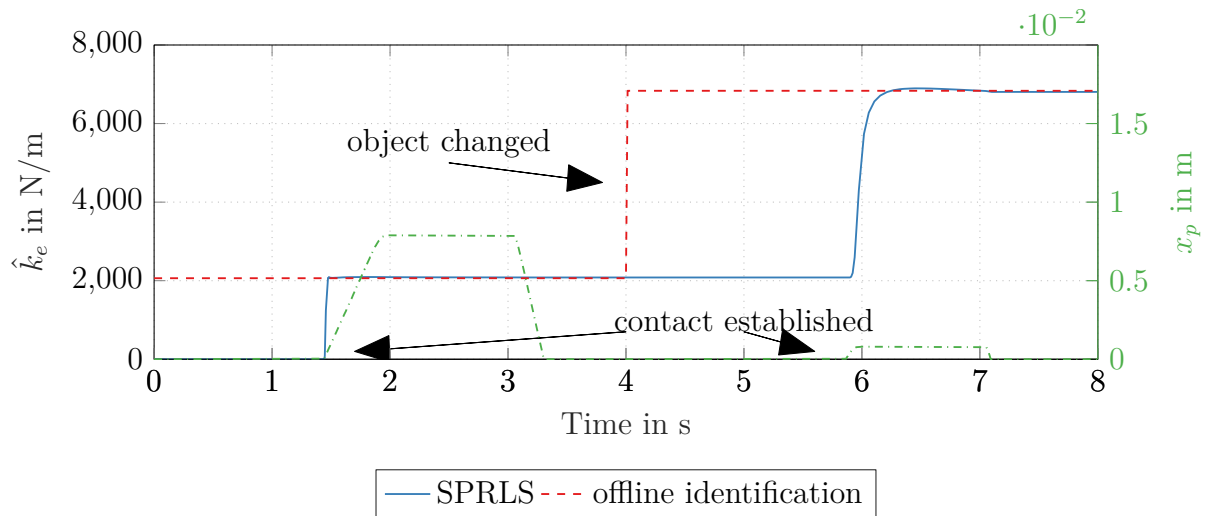
Figure 2.6: Online identification of the environment stiffness k_e and tracking of parameter changes utilizing the SPRLS algorithm. The red dashed line indicates the stiffness values that are obtained via offline identification. The penetration depth $x_p = x_e - x$ together with the estimation results show that the estimated stiffness approaches the real value soon after establishing contact.

the offline identification result. The overshoot of the online estimate at $t = 6.4\,\text{s}$ can be contributed to unmodelled dynamics of the second test object.

Chapter 3

Introduction to Interaction Control

The following chapter briefly introduces the principles of interaction control. Fundamental properties of common approaches are highlighted. Next the advantages and disadvantages of the different strategies are examined with special regard to the physical properties of the system identified in Chapter 2. This includes the manipulator which is subject to considerable nonlinear friction forces and stiff, spring-like environments. As an outcome, this chapter provides the basis for the control design in Chapter 4.

3.1 Overview of Interaction Control

Interaction control always involves the control of forces between the manipulator and the environment. Therefore it is worthwhile to take a look on the different force control approaches. Figure 3.1 shows a classification according to [31, pp. 161]. A preliminary distinction can be made between direct and indirect force control approaches.

3.1.1 Direct Force Control

In *direct* force control, the interaction force is the controlled variable and the goal is to make it follow a reference via a force feedback loop. *Hybrid* force/motion control
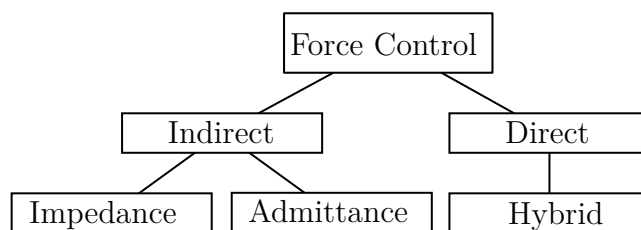
Figure 3.1: Schematic overview of different force control strategies.

is a special case for manipulators with several degrees of freedom. A subspace of the manipulators' workspace is force-controlled, and the remaining degrees of freedom are motion controlled [32, 33]. Example applications for hybrid force control include milling or grinding tasks where a distinct contact force is desired, while a manipulator moves along the work piece.

3.1.2 Indirect Force Control

In the indirect interaction control approaches, the force between the manipulator and the environment is not regulated to a fixed setpoint. Instead, the relationship between the contact force and the movement of the manipulator relative to a virtual equilibrium trajectory is defined. Subsequently, the manipulator is controlled to reproduce the modelled behaviour.

As an example the model

$$k_t \underbrace{(x - x_r)}_{x_p} = f_e \tag{3.1}$$

describes the relationship between the position deviation of the manipulator from a reference position $x_p = x - x_r$ and the force exerted on the manipulator f_e, with compliant behaviour. k_t is the target stiffness. The task of the interaction controller is to control the manipulator such that (3.1) is fulfilled. It was originally proposed by Salisbury [34] as *active stiffness control*.

Thinking of a mechanical interface, it is not possible to determine x and f_e independently. Only one variable can be regulated, the other results from the interaction. Consequently, there are two different control approaches to implement the desired interaction characteristic. The first approach is to determine x_p and evaluate (3.1) to obtain a desired force f_e, to which the manipulator is regulated subsequently. The second possibility is to measure the force f_e, determine the desired position

$$x_d = x_r + \frac{f_e}{k_t} \tag{3.2}$$

that fulfils the target model (3.1) and move the manipulator to this position. The two control approaches refer to *impedance* and *admittance* control, respectively. They are discussed in detail in the next section.
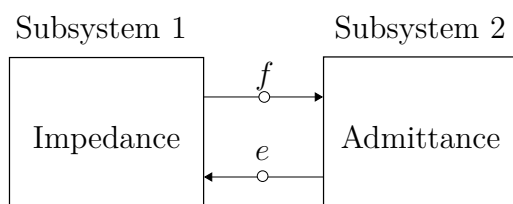
Figure 3.2: Impedance and admittance, connected via a power port consisting of a pair (e, f) of effort and flow variables. The arrows indicate the causality relations between the two subsystems.

3.2 Fundamentals of Impedance and Admittance Control

Impedance and admittance controllers are two possible implementations of the indirect force control strategy. However, both approaches have significantly different properties, which should be considered in order to select the best strategy for a given task. Before going into detail, the terms *impedance* and *admittance* should be defined. In electrical engineering, both terms are well known, as they describe the relationship between electric voltage and current. By introducing power ports this concept can be generalized.

3.2.1 Power Ports

Describing energy exchange between subsystems can be formalized independently of the physical domain by the concept of power ports. Figure 3.2 shows an example of two physical subsystems connected via a pair (e, f) of an *effort*- and a *flow*-variable. The product $P = ef$ has the physical unit of power and describes the instantaneous energy flow from one subsystem into another. Thus, the pair (e, f) is called a *power port*. Table 3.1 lists effort- and flow-variables for different physical domains.

Physical Domain	Effort	Flow
Mechanics linear)	Force	Velocity
Mechanics (angular)	Torque	Angular velocity
Electromagnetics	Voltage	Current
Hydraulics	Pressure	Flow rate
Thermodynamics	Temperature	Entropy

Table 3.1: Effort- and flow-variables for different physical domains [35, p. 239]

In linear electric systems, the electric impedance

$$Z = v/i \tag{3.3}$$

is defined as the relation between the electric voltage v and the current i. Using Table 3.1 the term impedance can be generalized and defined as a map

$$e = \mathcal{Z}(f) \tag{3.4}$$

from a flow- to an effort variable. Conversely, an admittance is a map

$$f = \mathcal{Y}(e) \tag{3.5}$$

from effort to flow.

According to the derivations above, for mechanical systems the term impedance refers to relationships between force and velocity. In literature though it is common practice to extend the definition to relationships between force and *motion* in general (see for example [8], [36] and [37]). This is convenient because it also includes compliant behaviour as in (3.1). Therefore this definition is adopted throughout this thesis as well. The same conventions apply to mechanical admittances.

3.2.2 Causality

A system which accepts a flow variable as input and yields an effort is said to be of *impedance causality*, hereby following the conventions of the last section. Conversely, a system is of *admittance causality* if its input variable is an effort and its output a flow. This leads finally to the definitions of the impedance controller for mechanical systems. An *impedance control law* maps a motion difference around an equilibrium to a desired force, while an admittance control law has force or torque as an input variable and yields a desired motion of the manipulator.

Linear static impedances and admittances can be converted into each other. As an example, the relationship between voltage and current at an electric resistor

$$u = \underbrace{R}_{\mathcal{Z}}\, i \quad \Leftrightarrow \quad i = \underbrace{\frac{1}{R}}_{\mathcal{Y}}\, u \tag{3.6}$$

can be described either with impedance- or with admittance causality, and there is no reason to prefer one form over the other. For general nonlinear systems, the conversion is not always possible [38].

Causality plays an important role when considering interaction of two systems. As indicated in Figure 3.2 systems can only be connected to their causal complement. If

(a) Lumped element model

(b) Equivalent Bond graph

(c) Bond graph causality relations
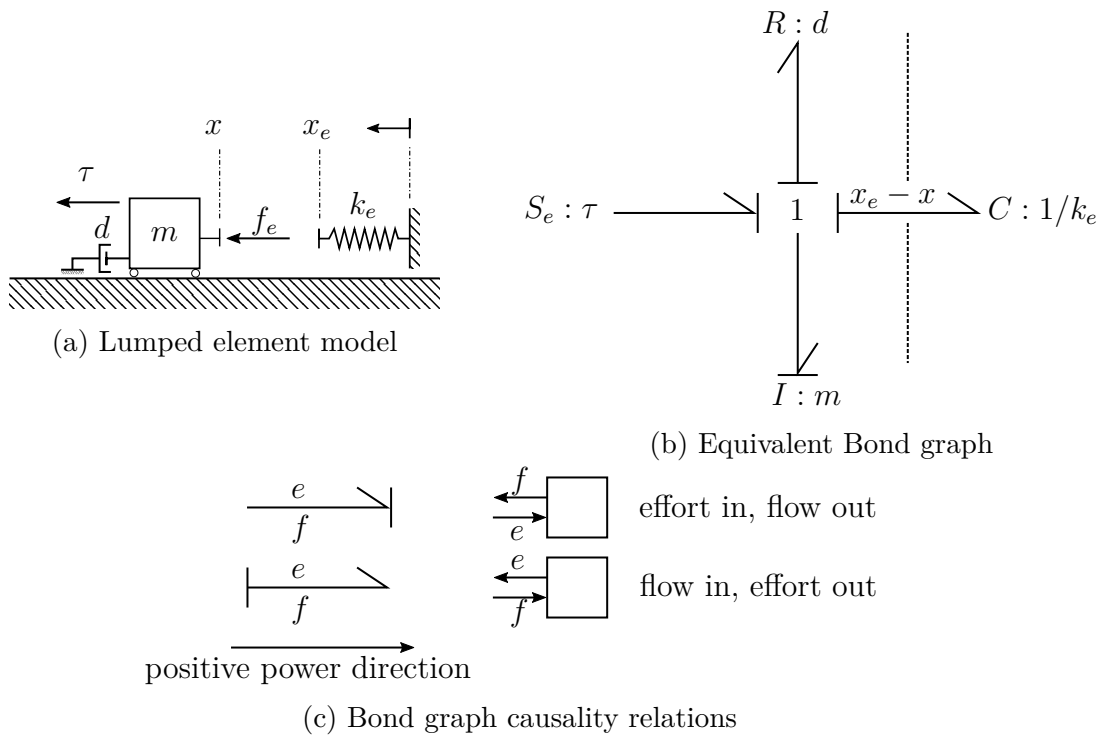
Figure 3.3: Lumped element model for an interaction scenario of a manipulator with a compliant environment (a) and equivalent bond graph representation (b). (c) shows the convention for causality and the direction of the positive power $P = ef$.

one system is of impedance causality, its counterpart must be an admittance and vice versa [38].

Figure 3.3a shows a simple lumped element model of a manipulator and an environment, consisting of an ideal spring k_e. Naturally, a linear motor does not start to move before a force is applied. To reflect this causality relation it is modelled as admittance. The environment must therefore be of impedance causality. For simple modelling of these relationships, bond graphs have proven to be an effective tool. Figure 3.3c shows the equivalent bond graph representation of the lumped element model together with causality relations and positive power direction (see Figure 3.3c) [35, pp. 237].

The theoretical considerations made so far have practical relevance for control design. As the manipulator is an admittance, only an impedance control law can be directly applied to it. In order to operate an admittance controller with the setup in Figure 3.3a, an additional *translating element* is needed, as it is impossible for two admittances to directly interact with each other. The detailed derivation of such a control structure is covered in the next section.

3.3 Simplified Interaction Control Example

To compare the impedance- and admittance control approaches, an illustrative example is developed in this section. The basis for this example is the situation pictured in Figure 3.3a. As a simplification $d = 0$ is assumed in the initial derivations. The influence of nonlinear friction is studied later in this section. By summation of the remaining forces acting on the manipulator, the equation of motion

$$m\ddot{x} = f_e + \tau \quad , \tag{3.7}$$

is obtained, where τ is the control input. The environment is assumed as a pure stiffness with fixed connection to the manipulator. The force follows to

$$f_e = -k_e x \quad . \tag{3.8}$$

Compared with the unilateral contact (2.17), the coupled system in this example is linear, which allows application of linear control theory for stability considerations. Proving stability for the full hybrid system with unilateral constraint is much more complex (see for example [39, 40, 41] for approaches) and out of the scope of this thesis. Nonetheless it is possible to draw conclusions from the simplified view for practical control design. It is also a reasonable approach to describe the coupled system behaviour around an equilibrium point characterized by point $f_R = k_e(x_e - x_R)$ while assuming that the manipulator does not lose contact i.e. $x < x_e \quad \forall t > 0$ does not occur. (3.8) can be written as transfer function $G_e(s) = -k_e$.

The goal of the interaction control in this example is to establish the manipulator response to an external force by the second-order dynamics

$$m_t \left(\ddot{x} - \ddot{x}_r \right) + d_t \left(\dot{x} - \dot{x}_r \right) + k_t \left(x - x_r \right) = f_e \quad , \tag{3.9}$$

where the parameters m_t, d_t and k_t represent virtual target mass, damping and stiffness respectively. This choice of parameters is arbitrary but allows easy interpretation of the behaviour. x_r is called the virtual equilibrium position. The target dynamics (3.9) are also named *virtual environment* (VE) in the following chapters. The transfer function from force to position deviation becomes

$$G_{ve}(s) = \frac{1}{m_t s^2 + d_t s + k_t} \quad . \tag{3.10}$$

Coupling the environment to the target dynamics by substituting (3.8) into (3.9) results in the nominal dynamics of the closed loop system. In the Laplace domain these become

$$\hat{x}(s) = \frac{m_t s^2 + d_t s + k_t}{m_t s^2 + d_t s + k_t + k_e} \hat{x}_r(s) \tag{3.11}$$

The roots of this transfer function are calculated to

$$s_{1/2} = \frac{-d_t \pm \sqrt{d_t^2 - 4 m_t \left(k_t + k_e \right)}}{2 m_t} \quad , \tag{3.12}$$

from which it can be seen that (3.11) is stable if $d_t > 0$ assuming all other parameters are greater than zero. Generally speaking, for any *passive* environment transfer function $G_e(s)$, the closed loop transfer function

$$T_{x_r, x}(s) = \frac{1}{1 - G_{ve}(s) G_e(s)} \tag{3.13}$$

is stable, if $G_{ve}(s)$ is positive real [42, pp. 277].

3.4 Impedance Control

In this control approach, the controller acts as a mechanical impedance. This means that the controller takes movement as an input variable and delivers a force as an output (see Section 3.2). This force can be directly connected to the manipulator input.

Substituting (3.9) into (3.7), the impedance control law follows directly to

$$\tau = m \ddot{x} - m_t \left(\ddot{x} - \ddot{x}_r \right) - d_t \left(\dot{x} - \dot{x}_r \right) - k_t \left(x - x_r \right) \quad . \tag{3.14}$$
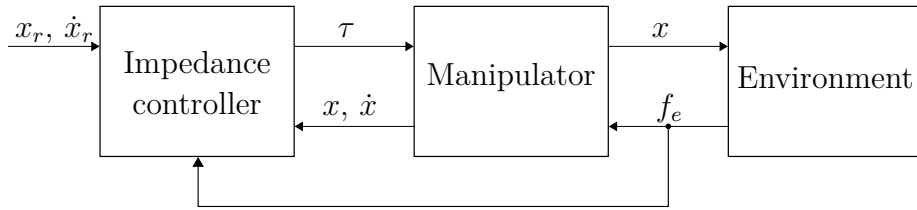
Figure 3.4: Schematic overview of the impedance control loop.

The impedance controller applies a force to the manipulator proportional to the deviation of the actual movement of the manipulator from the virtual equilibrium trajectory. (3.14) also shows that, in order to implement an impedance control law, it is not necessary to measure the force between manipulator and environment directly. In contrast it influences the control law indirectly via the acceleration of the manipulator which has to be known instead. To include rather a force measurement than the acceleration, (3.7) can be substituted into (3.14) to yield the control law [43]

$$\tau = \left(\frac{m}{m_t} - 1\right) f_e + m\ddot{x}_r - \frac{m}{m_t} \left(d_t \left(\dot{x} - \dot{x}_r\right) + k_t \left(x - x_r\right)\right) \quad . \tag{3.15}$$

This is usually desired, as an acceleration measurement is often not available and obtaining $\ddot{x}$ via numerical differentiation increases the noise in the control loop. In the absence of modelling errors, the achieved closed-loop dynamics match exactly the closed-loop target dynamics (3.11). Figure 3.4 shows a schematic overview of the final control structure.

3.4.1 Properties and Limitations

The impedance control law (3.15) has remarkable similarity to a *proportional-derivative* (PD) position controller. This is especially true, if $m_t = m$ is chosen. The control law reduces to

$$\tau = -d_t \left(\dot{x} - \dot{x}_r\right) - k_t \left(x - x_r\right) \quad . \tag{3.16}$$

Hence, it is advisable to consider the desired target dynamics *already in the mechanical design process for the manipulator.* By doing so, the high frequency dynamics can be determined by the manipulator itself, which reduces control effort.

Clearly the manipulator controlled by (3.16) reacts to an external force with a movement deviation from the reference trajectory. This is intended by the control principle. However, this does not only include the desired response from coupling with the environment, but also disturbance forces like friction. Parameter uncertainties also lead to a steady state error, which cannot be compensated with this architecture. The disturbance rejection depends on the values of k_t target dynamics. This means, if good

disturbance rejection is needed, the impedance control approach is restricted to a high target stiffness.

Another important observation is that if the manipulator is already subject to damping $d \neq 0$ as illustrated in Figure 3.3a, this has to be considered during control law (3.15) by an additional feedforward term $d\dot{x}$. This is increasingly problematic, the smaller the targeted damping factor d_t as if d or $\dot{x}$ are not exactly known, the closed-loop might become unstable. In the presence of nonlinear friction, the situation is even more difficult from Section 2.2.1 it is known that this phenomenon can be very difficult to compensate completely. In order to achieve good impedance control performance, $d_t\dot{x}$ should be substantially larger than the nonlinear friction.

Figure 3.5 shows an example of the force response of an impedance-controlled floating mass, subject to different disturbances. The environmental contact with the manipulator is fixed in this example. Input to this simulation is a change in the setpoint of the reference trajectory from the origin to $x_r = -0.1\,\mathrm{m}$. The ideal response is illustrated with a dashed line. The effect of a parameter error is illustrated, where the simulated mass $\tilde{m}$ is set to 1.5 times the mass m known by the controller. It can be observed that this leads to a frequency error for the coupled oscillation mode between the nominal and the actual system response. For the third experiment, (3.7) is expanded with an additional Coulomb friction term to

$$m\ddot{x} = f_e + \tau - f_c \,\mathrm{sign}(v) \quad , \tag{3.17}$$

where $f_c = 5\,\mathrm{N}$ was used as simulation parameter. While the additional dissipative term has no effect on stability, the controller is not able to reproduce the target behaviour.

3.5 Admittance Control

According to the definition the admittance controller takes the external force f_e as input and computes a desired movement of the manipulator. As the manipulator is an admittance as well, the output of the admittance controller can not directly serve as input to the manipulator. In case the desired movement is a velocity, an inner velocity control loop must must be closed such that the manipulator follows the velocity commanded by the admittance controller. In this example, the controller yields a desired position and consequently, a position controller serves as connecting element.

Figure 3.6 shows a schematic overview of the admittance-controlled system with the different subsystems. The position-controlled manipulator together with the environment forms an impedance which interacts with the target system in the admittance controller. It can further be seen that, if perfect position control is assumed and therefore $x_d = x$, the manipulator becomes transparent. This means that the vir-
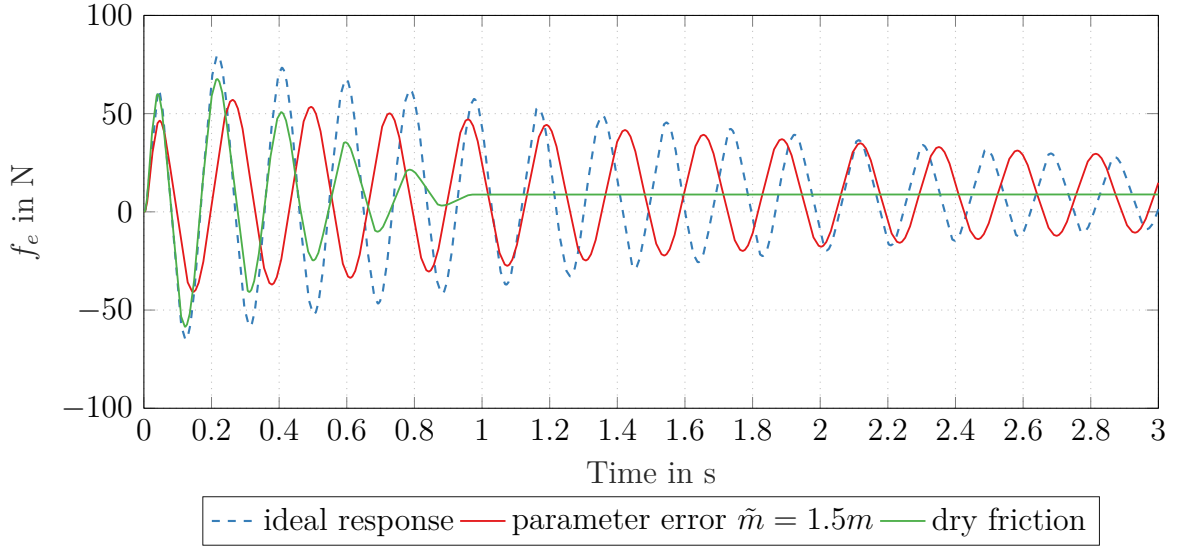
Figure 3.5: Force response of a floating mass, which is impedance-controlled subject to two exemplary disturbances. The blue dashed line shows the ideal interaction force after a setpoint change of the position. For simulation the following parameters were used: $m = 1.5\,\mathrm{kg}$, $m_t = 1\,\mathrm{kg}$, $d_t = 1\,\mathrm{Ns/m}$, $k_t = 100\,\mathrm{N/m}$, $k_e = 1000\,\mathrm{N/m}$.

tual environment is perfectly coupled to the actual environment. If the environment is not in contact with the manipulator, the admittance control loop is opened and the position-controlled manipulator remains.

To derive the admittance controller perfect position following is assumed. Then x can be replaced by x_d in (3.9), which yields

$$\left(m_t s^2 + d_t s + k_t\right)\left(\hat{x}_d(s) - \hat{x}_r(s)\right) = \hat{f}_e(s) \tag{3.18}$$

in the Laplace domain and after rearranging to

$$\hat{x}_d(s) = \frac{1}{m_t s^2 + d_t s + k_t}\hat{f}_e(s) + \hat{x}_r(s) \tag{3.19}$$

immediately reveals the admittance controller transfer function

$$G_{ad}(s) = G_{ve}(s) = \frac{1}{m_t s^2 + d_t s + k_t} \quad . \tag{3.20}$$

The desired position in this approach is calculated by $\hat{x}_d(s) = G_{ad}(s)\hat{f}_e(s)$. As a next step, the position control loop has to be considered. In order to do that, a PD-controller

$$\tau = k_p\left(x_d - x\right) - k_d \dot{x} \quad , \tag{3.21}$$
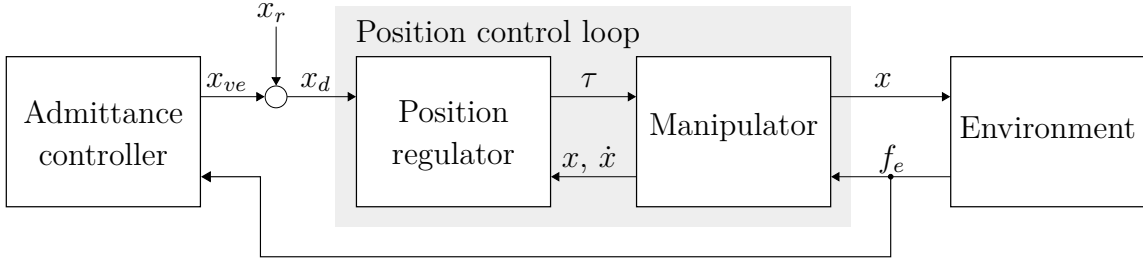
Figure 3.6: Schematic overview of the admittance control loop consisting of the admittance controller, the position-controlled manipulator and the environment.

is assumed as inner control law. It is important to note that this is not the only position control law applicable. The parameters k_p and k_d represent the proportional and the derivative feedback gains. Closing the position loop in (3.7) leads to

$$m\ddot{x} = f_e + k_p\,(x_d - x) - k_d\dot{x} \quad , \tag{3.22}$$

and the closed position loop can be expressed in the Laplace domain as

$$\hat{x}(s) = \frac{1}{ms^2 + k_d s + k_p}\left(k_p\hat{x}_d(s) + \hat{f}_e(s)\right) \quad , \tag{3.23}$$

or

$$\hat{x}(s) = G_p(s)\hat{x}_d(s) + G_d(s)\hat{f}_e(s) \tag{3.24}$$

with the abbreviations

$$G_p(s) = \frac{k_p}{ms^2 + k_d s + k_p} \tag{3.25a}$$

$$G_d(s) = \frac{1}{ms^2 + k_d s + k_p} \quad . \tag{3.25b}$$

$G_p(s)$ is the closed-loop transfer function of the position control loop. From the inner loop's point of view, the interaction force f_e acts as a disturbance force on the manipulator. Thus $G_d(s)$ is the disturbance transfer function from any force input to the position output. To derive the closed loop transfer function under admittance control, at first (3.23) is rearranged using the relationship $\hat{f}_e(s) = -k_e\hat{x}(s)$ to

$$(ms^2 + k_d s + k_t + k_e)\hat{x}(s) = k_p\hat{x}_d(s) \quad . \tag{3.26}$$

Substituting the admittance control law (3.20) into (3.26) leads to

$$(ms^2 + k_d s + k_t + k_e)\hat{x}(s) = k_p\left(-\frac{k_e}{m_t s^2 + d_t s + k_t}\hat{x}(s) + \hat{x}_0(s)\right) \quad , \tag{3.27}$$

where $\hat{x}(s)$ can be expressed as

$$\hat{x}(s) = \frac{k_p \left(m_t s^2 + d_t s + k_t\right)}{\left(m s^2 + k_d s + k_t + k_e\right)\left(m_t s^2 + d_t s + k_t\right) + k_p k_e}\hat{x}_0(s) \quad . \tag{3.28}$$

The stability of this transfer function can no longer be determined directly. The *Routh-Hurwitz* criterion provides a tool to derive parameter sets for which the transfer function is stable. It is also obvious that for $k_p \to \infty$, (3.28) reduces to the desired closed loop transfer function (3.11). In the following section, influence of different parameter constellations are investigated.

Impact of the environment stiffness on stability

According to (3.12), the coupled stability of the target dynamics with the environment stiffness in (3.11) does not depend on k_e. For $d_t^2 > 4m_t(k_t + k_e)$ the poles of the transfer function are a complex-conjugated pair. Increasing k_e only affects the imaginary part of the poles. This is not the case any more if a position controller with finite bandwidth has to be considered. Figure 3.7 shows the pole-zero map of the closed loop transfer function (3.28) for varying parameters of k_e. The left cluster of poles in Figure 3.7a is due to the position controller, whereas the mode close to the imaginary axis is due to the coupling mode between the target dynamics and the environment stiffness. The right plot shows a magnified view around the imaginary axis. As k_e increases, the complex conjugate pole pair moves towards the imaginary axis and the system eventually becomes unstable, which is *not* the case in the ideal coupling. Conversely, for fixed k_e, increasing the angular cutoff frequency

$$\omega_0 = \sqrt{\frac{k_p}{m}} \tag{3.29}$$

of the position control loop causes the poles of (3.28) to move towards the poles of the ideal system. $k_d = \frac{2k_p}{m}$ is chosen in this example to achieve a critically damped position control transfer function. Therefore, a minimum closed-loop bandwidth of the position-controlled system exists for which the interaction with a certain environment stiffness is stable. Figure 3.8 shows this relationship for different values of d_t. Increasing the damping factor of the VE decreases the minimum position controller bandwidth for stable interaction.

(a) all poles and zeros

(b) magnification of the dashed area
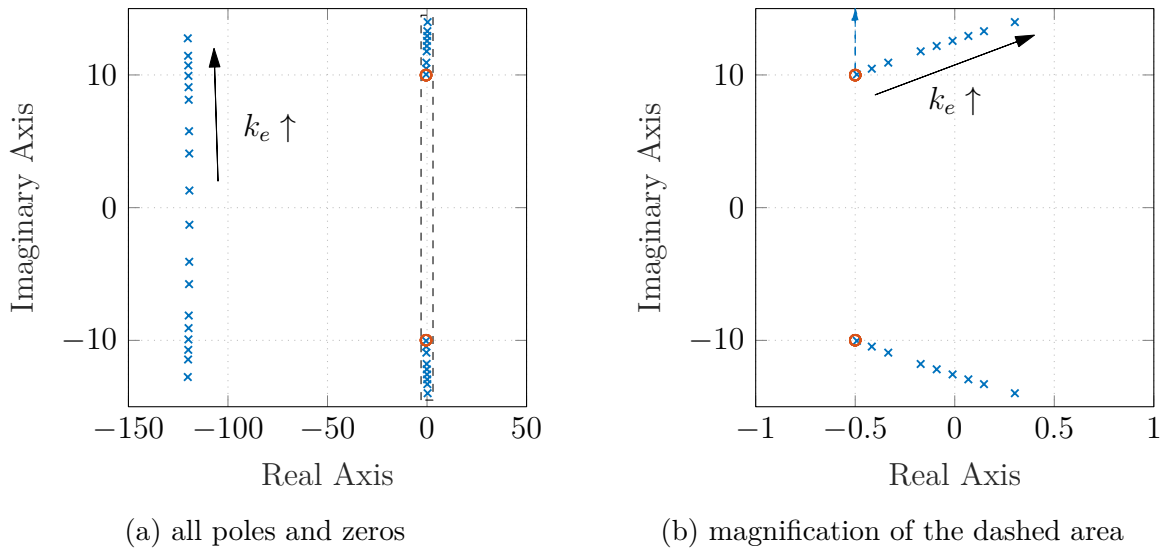
Figure 3.7: Pole-zero plot for the system (3.28) subject to varying k_e. The right plot shows the zoomed view of the area in the left plot surrounded with the dashed line. The blue arrows show how the poles shift in the ideally coupled case (3.11).
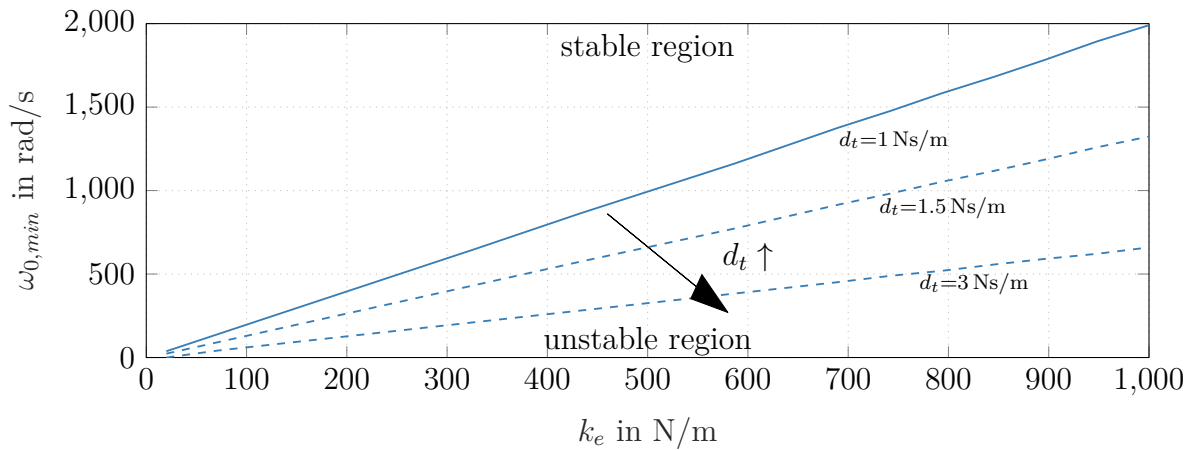
Figure 3.8: Minimum position controller cut-off angular frequency ω_0 needed for stable contact as a function of environment stiffness k_e.

3.5.1 Improved Admittance Control Law

The simple admittance control law (3.20) proposed in the last section has the disadvantage that the bandwidth of position control loop directly influences the maximum environment stiffness, for which the interaction control is stable. Substituting (3.20) into (3.30b) yields

$$\hat{x}(s) = G_p(s)\left[\hat{x}_r(s) + G_{ad}(s)\hat{f}_e(s)\right] + G_d(s)\hat{f}_e(s) \tag{3.30a}$$

$$= G_p(s)\hat{x}_r(s) + \left[G_p(s)G_{ad}(s) + G_d(s)\right]\hat{f}_e(s) \quad . \tag{3.30b}$$

Comparing (3.30b) to the desired linear motor response

$$\hat{x}(s) = G_p(s)\hat{x}_r(s) + G_{ve}(s)\hat{f}_e(s) \quad , \tag{3.31}$$

immediately provides the admittance control law

$$G_{ad}(s) = \left(G_{ve}(s) - G_d(s)\right)G_p^{-1}(s) \quad . \tag{3.32}$$

If $G_{ad}(s)$ is proper, the admittance controller can be implemented and the closed-loop transfer function

$$T_{x_r,x}^{ad}(s) = \frac{G_p(s)}{1 - G_{ve}(s)G_e(s)} \tag{3.33}$$

is stable if both, the position control loop and the virtual environment are stable. The difference between the improved admittance control law (3.32) and the simple admittance control law (3.20) is illustrated in Figure 3.9. Additionally, the impact of increasing the bandwidth of the position control loop is highlighted. The improved controller transfer function amplifies high-frequency components of the measured force. Hence, it is important to utilize force sensors with a high measurement bandwidth together with this admittance control law.

3.6 Sampling

It has been shown in the previous sections that under ideal circumstances, interaction controllers can be designed that ensure stable interaction between manipulator and environment regardless of environment parameters. However, controllers are usually implemented digitally and discretization effects must be considered. It turns out that discrete impedance controllers do not necessarily lead to stable coupled closed loop systems anymore [44]. The reason is that the sample-and-hold operator used to discretize the impedance controller does not preserve the passivity property of the originally continuous controller [45].
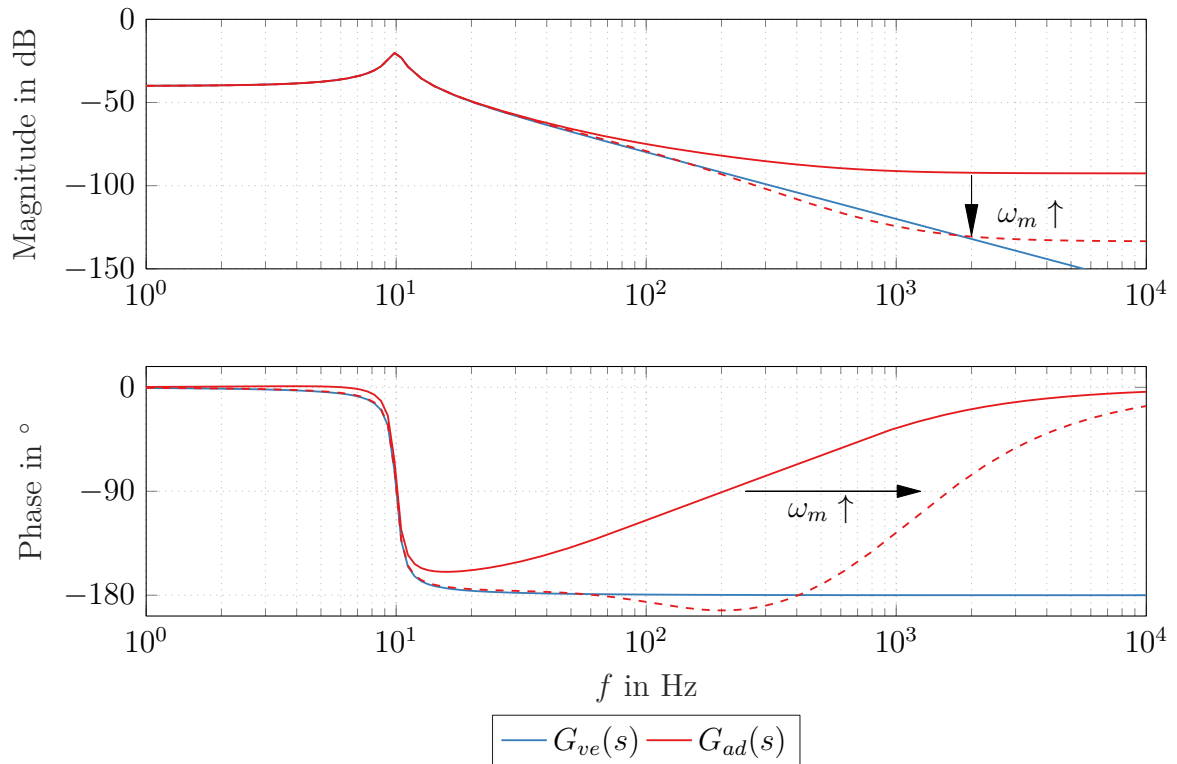
Figure 3.9: Comparison of the transfer functions of the simple admittance con-
troller (3.20) to the improved admittance controller (3.32). ω_m de-
notes the cut-off angular velocity of the position control loop. The
dashed line indicates the admittance control transfer function for
a higher value of ω_m. Thereby the amplification of high-frequency
components of the input can be decreased.
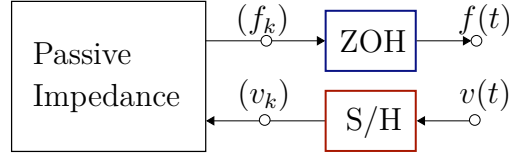
Figure 3.10: Coupling of a passive impedance to the corresponding continuous time power variables.

Remark 3.1 (Passivity). *A dynamic system*

$$\dot{\mathbf{x}} = f(\mathbf{x}, \mathbf{u}) \tag{3.34a}$$

$$\mathbf{y} = h(\mathbf{x}, \mathbf{u}) \quad , \tag{3.34b}$$

is said to be passive, *if a so called storage function* $V(\mathbf{x}) : \mathbb{R}^n \to \mathbb{R}^+$ *with* $V(\mathbf{0}) = 0$ *exists, such that the the inequality*

$$\int_0^t \mathbf{u}^{\mathrm{T}}(\tau)\mathbf{y}(\tau)\mathrm{d}\tau \geq V(\mathbf{x}(t)) - V(\mathbf{x}(0)) \tag{3.35}$$

is fulfilled $\forall t \geq 0$. *Consequently,*

$$\mathbf{u}^{\mathrm{T}}(t)\mathbf{y}(t) \geq \dot{V}(\mathbf{x}(t), \mathbf{u}(t)) \tag{3.36}$$

must hold as well. If $V(\mathbf{x})$ represents the energy of the system and $\mathbf{u}$ and $\mathbf{y}$ pairs of collocated power variables , (3.36) states that the power flow into the system must always be greater or equal than the change of energy stored in the system. [46, pp. 228-237]. In the case of $\mathbf{x}(0) = \mathbf{0}$, (3.35) reduces to

$$\int_0^t \mathbf{u}^{\mathrm{T}}(\tau)\mathbf{y}(\tau)\mathrm{d}\tau \geq 0 \quad , \tag{3.37}$$

which highlights that a passive system cannot produce energy.

To illustrate this property, the situation depictured in Figure 3.10 is considered. A continuous time velocity signal $v(t)$ is sampled every T_s seconds. Via a discrete passive impedance the corresponding force f_k is calculated, which is in turn translated back to the continuous domain via a *zero-order hold* (ZOH) operation. According to (3.37) at the continuous time port the inequality $f(t)v(t) \geq 0$ must be fulfilled $\forall t \geq 0$. Through the definition of the zero-order hold operation, the continuous force becomes

$$f(t) = f_k \quad t \in [kT_s, (k+1)T_s) \quad , \tag{3.38}$$

while $v(t)$ is defined by the external connection. This leads to situations where passivity cannot be ensured anymore. For example, if the continuous impedance is given by a damping element

$$f = dv \quad , d > 0 \tag{3.39}$$

then the discrete impedance becomes simply

$$f_k = kv_k \quad . \tag{3.40}$$

Clearly (3.39) is passive. **??** shows the situation if the discrete impedance (3.40) is coupled to the continuous interface for $d = 1\,\text{Ns/m}$. In the hatched areas, the passivity inequality (3.37) is violated, meaning that the subsystem produces energy instead of dissipating it. In case of d becoming too small, the coupled system may even become unstable.

Figure 3.11 illustrates in detail the effect of sampling on admittance control with the help of a unilateral contact as it occurs at the actual test rig between the manipulator and the environment (see Figure 1.2). It shows the force on the manipulator-environment interface f_m for a continuous admittance controller 3.32 compared to the force that occurs, when the same controller is discretized with a sampling rate of $T_s = 250\,\text{Hz}$. Furthermore, the displacement of the virtual environment x_{ve}, which is the output signal of the admittance controller and the actual manipulator position x are displayed. It is obvious that in the interval $0 \leq T_{delay} < T_s$ the discrete admittance control law can not react to the impact and thus the stiff position control law keeps the manipulator moving along the nominal trajectory. Ultimately, more energy is transferred to the environment with the discrete interaction controller, which can be seen from the difference in the maximum penetration depth Δx_p and the relationship $E_{pot} = \frac{k_e x_p^2}{2}$. In order to minimize this effect, the sampling rate has to be increased.

The issue of passivity preserving discretization has been addressed by several authors over the last two decades, mainly for the purpose of haptic control. Colgate and Schenkel [44] showed that physical damping must be present in order to dissipate the excess energy of the zero-order hold operation. In [45] Stramigioli et al. provide theoretical background for equivalent continuous and discrete-time energy flow. Several approaches deal with the case of *passification* of a given discrete impedance. Hannaford and Ryu [47] introduce a *passivity observer/ passivity controller* (PO/PC) structure to guarantee passivity under the assumption of constant velocity and force during a sampling interval. The principle of the PO/PC structure is to measure the energy flow

$$E_{obsv,k} = T_s \sum_{i=0}^{k} f_i v_i \tag{3.41}$$
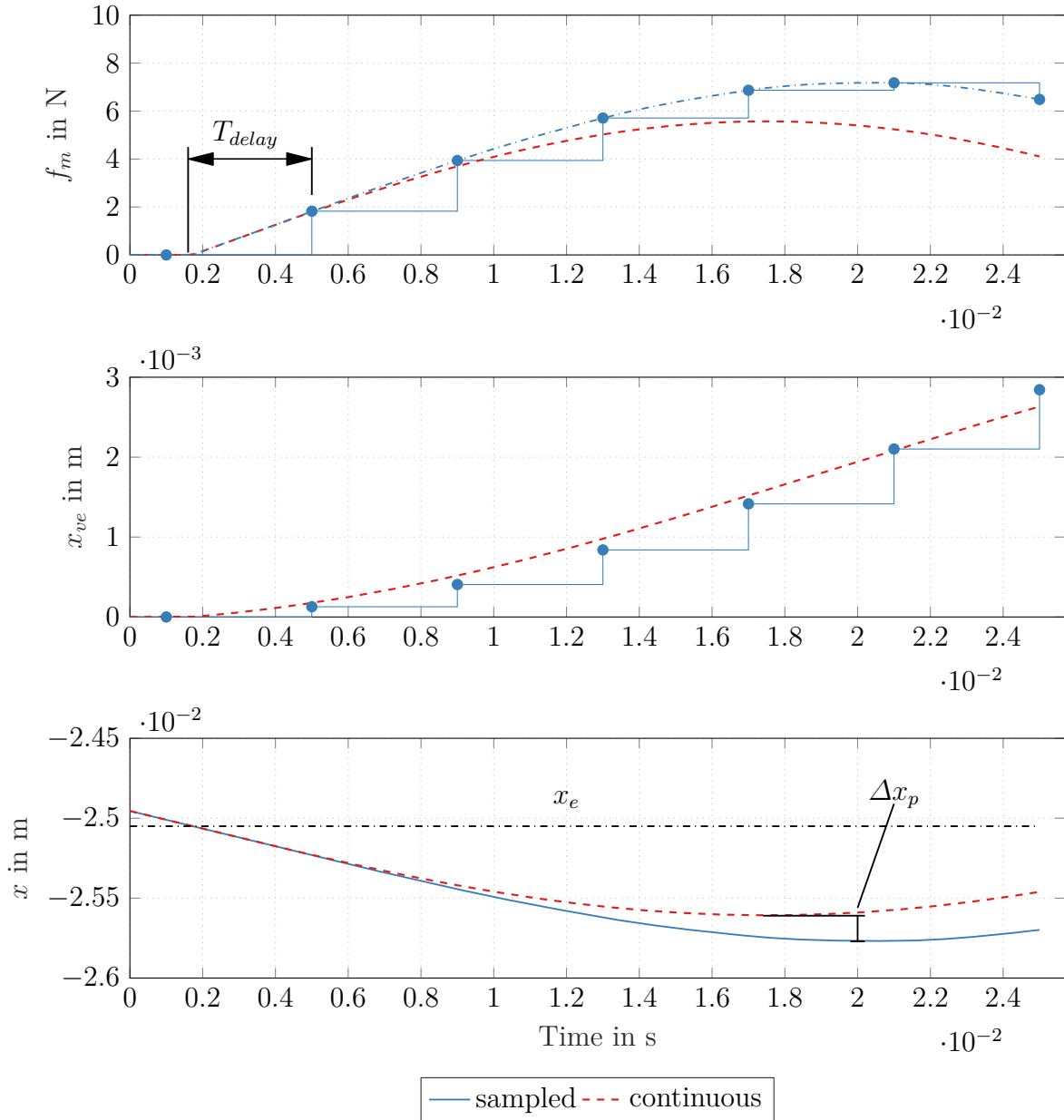
Figure 3.11: Effect of sampling on the admittance control performance. This plot shows the impact of the manipulator on a spring-like environment, located at $x_e = -0.025\,\mathrm{m}$ with a stiffness $k_e = 10\,\mathrm{kN/m}$. For $x < x_e$ contact is established. 3.32 is used as admittance control law. $\hat{x}_{ve}(s) = G_{ad}(z)\hat{f}_m(s)$ is the displacement deviation from the virtual equilibrium trajectory x_r due to the admittance controller.

into a subsystem, for example a discrete interaction controller, and absorb the excess
energy with an additional control signal. There are, however, some two problems which
make the approach not very practical:

- Considering the discrete-continuous interface Figure 3.10, either the force or the
  velocity are not constant during a sampling interval. The error is integrated in
  (3.41) over time.

- Obtaining an accurate velocity signal is sometimes difficult in practice if a ma-
  nipulator is only equipped with an position sensor. In Section 5.2 it is shown that
  this is an elaborate task for the linear motor used in this thesis.

To address these problems, the PO/PC structure was generalized in [48] for non-
constant velocities by determining the energy by

$$
\begin{aligned}
E_{obsv,k} &= \sum_{i=0}^{k-1} \int_{iT_s}^{(i+1)T_s} f(\tau)v(\tau)\mathrm{d}\tau \\
&= \sum_{i=0}^{k-1} f_i \int_{iT_s}^{(i+1)T_s} v(\tau)\mathrm{d}\tau \\
&= \sum_{i=0}^{k-1} f_i \left(x_{i+1} - x_i\right)\mathrm{d}\tau \quad .
\end{aligned}
\tag{3.42}
$$

The advantages of this method are that no velocity measurement is needed and that
the energy at time index k can be exactly determined as soon as the measurement x_k
is available. Furthermore, it is apparent in (3.42) that this scheme is only applicable
for an impedance controller. In the case of an admittance (controller), the velocity is
constant and the force changes in between two samples. To obtain the exact energy
as in (3.42), would require to measure the velocity and the integral of the force to be
measured.

   In [49, 50, 51] a method called *energy bounding algorithm* (EBA) is presented, which
aims to limit the energy produced by the zero-order hold to the maximum that can
be dissipated by the physical system. This is done by limiting the force forwarded to
the interaction controller. It is deduced by requiring the energy transferred into the
discrete system, i.e. the interaction controller, to be passive.

$$
\int f(\tau)v(\tau)\mathrm{d}\tau + \epsilon_0 \geq 0.
\tag{3.43}
$$

This condition is then discretized with similar reasoning as (3.42), resulting in the same
limitations for admittance control. Additionally, implementing the EBA for admittance
control may lead to much higher contact forces which must be compensated by adjusting
the reference trajectory [51].

3.7 Conclusion

In the last section, the principal interaction control laws for the impedance- and for the admittance control approach were derived. It was seen that the impedance controller is limited by the realizable target dynamics. To implement an admittance controller on a mechatronic system an additional motion control loop is required. This section wraps up the pros and cons of each approach in-depth to provide the basis for interaction control design for the linear motor modelled in Section 2.1.

The impedance control law (3.15) requires the first two derivatives of the virtual equilibrium trajectory x_r as well as a measurement of the position and the velocity of the manipulator. Generally, from (3.14) it can be seen that the transfer function of the impedance controller $G_{imp}(s) = G_{ve}^{-1}(s)$, is the inverse of the virtual environment and not proper for orders greater than one. To implement an impedance control law, the derivatives of the manipulator position must be known up to the order of the target dynamics. This limits the choice of practically implementable target dynamics for the impedance control approach. It can be implemented in the presence of very stiff environments. Furthermore, the presence of unmodelled dynamics and nonlinear friction greatly influences the achieved target dynamics, hereby further reducing the freedom of design.

On the other hand the admittance control law (3.20) only relies on a force measurement and the virtual reference trajectory does not necessarily even need to be continuously differentiable, meaning it can contain steps. Furthermore, the target dynamics are not restricted to be of second-order like in the example of the previous sections. In principle an arbitrary complex realizable transfer function can be chosen. However, an admittance controller requires the implementation of an inner position control loop around the manipulator because it is an admittance as well. In contrast to the impedance controller, the additional degree of freedom offer the possibility to compensate for disturbances. Unfortunately, an admittance control loop may become unstable when in contact with a stiff environment, if the inner transfer function $G_p(s)$ is not perfectly known. The performance of both control concepts suffers if sampling effects are introduced.

Chapter 4

Control Design

In the course of this chapter a suitable interaction control strategy for the linear motor, identified in Chapter 2 is developed. In the first section the control goals are summarized for which the interaction control algorithm is optimized. The following sections outline the derivation of the controller itself.

4.1 Control Goals

In mechanical hardware-in-the-loop simulations, metal on metal contacts may occur. The manipulator is an admittance, hence the environment must be described as impedance. The simplest way to model a stiff contact impedance, is by a mechanical stiffness. For example, in [8] the coupling stiffness is assumed to be $k_e = 25\,\text{kN/m}$. The controller should therefore be able to cope with large environment stiffness values. Additionally, during a HiL simulation, the linear motor typically is not always in contact with the environment.

The goals can be stated as follows

G1 *Transparency:* If coupled to the environment, the contact should behave as close as possible to the ideal behaviour. This means the contact should not be lost due to contact instability but also that no excessive damping should be present that unrealistically ensures contact.

G2 *Stability:* Interaction stability should not be compromised by the environment dynamics, assuming that an actual passive ideal system interaction should be realized in the HiL case.

G3 *Open loop performance:* When not in contact, the manipulator should accurately follow a position reference trajectory.

G4 *Flexibility:* The control goals defined above should be reached whereby posing minimal constraints to the target dynamics.

4.1.1 Target Dynamics

A second-order time invariant system

$$m_t \left(\ddot{x} - \ddot{x}_r \right) + d_t \left(\dot{x} - \dot{x}_r \right) + k_t \left(x - x_r \right) = f_e \tag{4.1}$$

is chosen as the virtual environment (VE) to be emulated by the manipulator. Even though this seems like an arbitrary restriction of the target dynamics, it should be noted that a higher order transfer function with distinct poles can be decomposed into individual modes which admit the form of second-order transfer functions. By placing one admittance controller per mode in parallel, higher order systems can be emulated. When introducing the displacement of the actual trajectory from the nominal trajectory as $x_{ve} = x - x_r$, (4.1) can be written in the Laplace domain as

$$\hat{x}_{ve}(s) = G_{ve}(s)\hat{f}_e(s) \quad , \tag{4.2}$$

with

$$G_{ve}(s) = \frac{1}{m_t s^2 + d_t s + k_t} \quad . \tag{4.3}$$

The range of the achievable target dynamic resonance frequencies

$$f_{t,res} = \frac{1}{2\pi} \sqrt{\frac{k_t}{m_t}} \quad , \tag{4.4}$$

is in the range of $1 \ldots 10\,\mathrm{Hz}$ for the present test rig.

4.2 Control Strategy

In Chapter 2 it was shown that the linear motor experiences a considerable amount of friction. As pointed out in Section 3.4.1 this limits an impedance control approach to VEs with very high target stiffness. Furthermore, an impedance control law would not allow to extend the dynamics to higher orders, which stands in conflict with control goal G4. Therefore an admittance control approach is chosen. Two controllers are designed in the following:

1. A *position controller* whose purpose is to make the linear motor accurately follow a given displacement reference while rejecting disturbances from friction and interaction of the linear motor with the environment.

2. Around the inner control loop, the *admittance control loop* is closed. It utilizes knowledge of the controlled linear motor to decouple the contact performance from the inner control loop as described in Section 3.5.1.

4.3 Position Control Strategy

As a starting point for controller design, the continuous-time system (2.3) is discretized to

$$\mathbf{x}_{k+1} = \mathbf{\Phi}\mathbf{x}_k + \mathbf{\Gamma}u_k + \mathbf{F}f_{d,k} \tag{4.5a}$$

$$y_k = \mathbf{c}^{\mathrm{T}}\mathbf{x}_k \quad . \tag{4.5b}$$

The linear motor has a position sensor, therefore $\mathbf{c}^{\mathrm{T}} = \begin{bmatrix} 1 & 0 \end{bmatrix}$. In the first design step, the disturbance input $f_{d,k}$ is neglected. This is justified, because later a feedforward friction compensator is applied.

4.3.1 Reference Model Following State-Space Controller Design

The goal is to design a state feedback controller such that the closed-loop system from desired input reference position to the position output can be described by LTI system dynamics. In literature, this task is also called the servo problem [52, pp. 147-156]. The desired dynamic behaviour is given by

$$\bar{\mathbf{x}}_{k+1} = \mathbf{\Phi}_m\bar{\mathbf{x}}_k + \mathbf{\Gamma}_m x_{d,k} \tag{4.6a}$$

$$\bar{y}_k = \mathbf{c}_m^{\mathrm{T}}\bar{\mathbf{x}}_k \quad . \tag{4.6b}$$

To make the linear motor follow these dynamics, a two-degrees-of-freedom approach

$$u_k = -\mathbf{k}^{\mathrm{T}}(\bar{\mathbf{x}}_k - \mathbf{x}_k) + \bar{u}_k \tag{4.7}$$

is utilized. The control signal u_k is made up of a feedback term $u_{fb,k} = -\mathbf{k}^{\mathrm{T}}(\bar{\mathbf{x}}_k - \mathbf{x}_k)$ whose purpose is to stabilize the trajectory $\mathbf{x}_k$ of the plant around the internal model trajectory $\bar{\mathbf{x}}_k$, and a feedforward signal $\bar{u}_k$. The feedback gain vector $\mathbf{k}^{\mathrm{T}}$ can be designed by means of pole placement or optimal control to achieve desired closed loop performance. In this thesis, the values of $\mathbf{k}^{\mathrm{T}}$ are derived my means of *linear-quadratic regulator* (LQR) design. Thus, the position control strategy is referred to as *reference model following LQR* (RLQR) controller below.

Investigating (4.7) one advantage of this control approach becomes apparent. The reference model (4.6) acts as an input filter to the reference trajectory. This allows

much larger values in $\mathbf{k}^{\mathrm{T}}$ to be chosen, which in turn improves the disturbance rejection. Furthermore, $\bar{\mathbf{x}}_k$ contains position and velocity reference $\bar{v}_k$ states. Due to this useful property, $\bar{v}_k$ can directly be utilized below for friction feedforward compensation, eliminating the need to numerically differentiate the input reference $x_{d,k}$.

Feed-Forward Signal Generation

The design of $\mathbf{k}^{\mathrm{T}}$ in the last section stabilizes the trajectory error $\mathbf{e}_k = \bar{\mathbf{x}}_k - \mathbf{x}_k$, but it is not assured that the actual output y_k follows the model output $\bar{y}_k$ exactly. This is the purpose of the feedforward signal $u_{ff,k} = \bar{u}_k$.

The plant system (4.5) as well as the reference system (4.6) can be represented as discrete transfer functions

$$G(z) = \mathbf{c}^{\mathrm{T}} \left(z\mathbf{E} - \mathbf{\Phi}\right)^{-1} \mathbf{\Gamma} \tag{4.8a}$$

$$G_m(z) = \mathbf{c}_m^{\mathrm{T}} \left(z\mathbf{E} - \mathbf{\Phi}_m\right)^{-1} \mathbf{\Gamma}_m \quad . \tag{4.8b}$$

To accomplish output following,

$$\bar{y}_z(z) = G_m(z)x_{d,z}(z) \stackrel{!}{=} G(z)\bar{u}_z(z) = y_z(z) \quad , \tag{4.9}$$

must hold and the feedforward control signal $\bar{u}_z(z)$ in the z-domain follows directly to

$$\bar{u}_z(z) = \frac{G_m(z)}{G(z)} x_{d,z}(z) \quad . \tag{4.10}$$

(4.10) reveals certain requirements that must be fulfilled in order to realize the feedforward signal. The relative degree of $G_m(z)$, which is defined as the difference between the degree of the numerator polynomial and the degree of the denominator polynomial, must be equal or smaller than the relative degree of $G(z)$. Furthermore, all zeros of $G(z)$ outside of the unit circle must be zeros of $G_m(z)$ as well.

From (2.2) it is known that the linear motor model is a second-order system and therefore the structure of $G(z)$ is of the form

$$G(z) = \frac{n_G(z)}{d_G(z)} = \frac{b_0 + b_1 z + b_2 z^2}{a_0 + a_1 z + a_2 z^2} \quad . \tag{4.11}$$

Note that with zero-order hold discretization almost all resulting discrete systems have a relative degree of one (see [53, p. 434]) and in this case $b_2 = 0$ in (4.11). The reference

model is chosen to have second-order behaviour as well. To derive the discrete model $G_m(z)$, at first a continuous system

$$\dot{\bar{\mathbf{x}}} = \underbrace{\begin{bmatrix} 0 & 1 \\ -\omega_m^2 & -2\xi_m\omega_m \end{bmatrix}}_{A_m} \bar{\mathbf{x}} + \underbrace{\begin{bmatrix} 0 \\ \omega_m^2 \end{bmatrix}}_{\mathbf{b}_m} \tag{4.12a}$$

$$\bar{y} = \underbrace{\begin{bmatrix} 1 & 0 \end{bmatrix}}_{\mathbf{c}_m^{\mathrm{T}}} x_d \tag{4.12b}$$

is chosen, with ξ_m as damping parameter and ω_m as angular cut-off frequency respectively. The denominator of $G_m(z)$ follows directly to

$$d_{G_m}(z) = \det\left[z\mathbf{I} - \exp(\mathbf{A}_m T_s)\right] \quad. \tag{4.13}$$

It is then desirable to choose the nominator of $G_m(z)$ equal to the denominator of $G(z)$. The resulting model transfer function becomes

$$G_m(z) = A\frac{n_{G_m}(z)}{d_{G_m}(z)} = A\frac{n_G(z)}{d_G(z)} = A\frac{b_0 + b_1 z + b_2 z^2}{\bar{a}_0 + \bar{a}_1 z + z^2} \quad. \tag{4.14}$$

A is a parameter that allows to adjust the system's steady-state gain. This choice of $G_m(z)$ has the effect that (4.10) under the consideration of (4.11) and (4.14) reduces to

$$\bar{u}_z(z) = A\frac{a_0 + a_1 z + a_2 z^2}{\bar{a}_0 + \bar{a}_1 z + z^2} x_{d,z}(z) \quad. \tag{4.15}$$

In order to obtain the time-domain sequence $(\bar{u}_k)$, a state-space realization of (4.15) is generated (see [53, p. 440]):

$$\bar{\mathbf{x}}_{k+1} = \begin{bmatrix} 0 & 1 \\ -\bar{a}_0 & -\bar{a}_1 \end{bmatrix} \bar{\mathbf{x}}_k + \begin{bmatrix} 0 \\ 1 \end{bmatrix} x_{d,k} \tag{4.16a}$$

$$\bar{u}_k = \underbrace{\begin{bmatrix} a_0 - a_2\bar{a}_0 & a_1 - a_2\bar{a}_1 \end{bmatrix}}_{\bar{\mathbf{c}}_m^{\mathrm{T}}} \bar{\mathbf{x}}_k + \underbrace{Aa_2}_{r_m} x_{d,k} \quad. \tag{4.16b}$$

It can be seen in (4.16) that if the discrete reference system is present in the *controllability canonical form*, the feedforward control signal $\bar{u}_k$ can directly be calculated from the reference state vector $\bar{\mathbf{x}}_k$ and the reference input $x_{d,k}$. Substituting (4.16b) into (4.7) results in the control law

$$u_k = -\mathbf{k}^{\mathrm{T}}(\bar{\mathbf{x}}_k - \mathbf{x}_k) + \bar{\mathbf{c}}_m^{\mathrm{T}}\bar{\mathbf{x}}_k + r_m x_{d,k} \quad. \tag{4.17}$$

It is worth noting that the ZOH discretization of (4.12) does not result in the *controllability canonical form* representation. However, it is straightforward to determine the

according linear transformation $\bar{\mathbf{z}}_k = \mathbf{T}\bar{\mathbf{x}}_k$. It is noted that the resulting states $\bar{\mathbf{z}}_k$ lose their physical meaning as positions and velocities. If one chooses to simulate the reference system in the controllable canonical form, and apply the control law (4.17), the states $\bar{\mathbf{x}}_k$ must be substituted by $\mathbf{T}^{-1}\bar{\mathbf{z}}_k$, where $\mathbf{T}^{-1}$ denotes the inverse transformation.

The Measurement State-Vector $\mathbf{x}_k$

In the control design above it was assumed that the full state vector of the linear motor $\mathbf{x}_k = \begin{bmatrix} x_k & v_k \end{bmatrix}^{\mathrm{T}}$ is available via measurement. In fact the linear motor has only a position sensor. The standard method to obtain an estimate of the state-vector is to design a state-observer, which can be extended with additional disturbance estimation [52, pp. 145-146] of the form

$$\begin{bmatrix} \hat{\mathbf{x}}_{k+1} \\ \hat{f}_{d,k+1} \end{bmatrix} = \begin{bmatrix} \mathbf{\Phi} & \mathbf{\Gamma} \\ \mathbf{0}^{\mathrm{T}} & 1 \end{bmatrix} \begin{bmatrix} \hat{\mathbf{x}}_k \\ \hat{f}_{d,k} \end{bmatrix} + \begin{bmatrix} \mathbf{\Gamma} \\ 0 \end{bmatrix} u_k + \begin{bmatrix} \hat{\mathbf{k}} \\ \hat{k}_f \end{bmatrix} \left(y_k - \mathbf{c}^{\mathrm{T}}\hat{\mathbf{x}}_k \right) \quad . \tag{4.18}$$

In combination with the RLQR controller (4.17) this approach is called RLQG below. When implemented as the position controller for the linear motor (2.2), the RLQG approach however does not yield satisfying results. The reason for this is mainly attributed to the large Coulomb friction component which acts on the linear motor. For every reversal of the velocity, the Coulomb friction force jumps between $\pm f_c$ and the assumption of a *constant-but-unknown* disturbance in (4.18) is violated. As a result velocities in the vicinity of zero cannot be estimated accurately, which negatively affects the controller's trajectory following capability by causing stick-slip motion. These characteristics are especially problematic when considering the admittance control setup. Jerky movement of the manipulator is amplified via the environment coupling to the measured force, which is fed back via the admittance controller to cause undesired oscillations. To overcome this problem, an additional acceleration sensor has been installed on the linear motor. Its signal is blended together with the position signal in order to obtain a more accurate estimation $\tilde{\mathbf{x}}_k^{\mathrm{T}} = \begin{bmatrix} \tilde{x}_k & \tilde{v}_k \end{bmatrix}$ of the state vector. The sensor fusion algorithm is presented in Section 5.2. Consequently, the state vector $\mathbf{x}_k$ in (4.17) has to be replaced by $\tilde{\mathbf{x}}_k$. To highlight the fact that a virtual measurement signal of the velocity is generated through sensor fusion, the combination of the RLQR controller with the sensor fusion algorithm (5.3) is referred to as RLQRv below.

4.3.2 Known Disturbance Feedforward

The coupling forces that arise when the linear motor is in contact with an environment act as unknown disturbances for the position control loop. It is desirable to minimize

their effects to the position following performance. Since a measurement of the external forces $f_{e,k}$ is available, it is possible to compensate for these forces simply by feedforwarding the measured disturbance as

$$\bar{u}_{e,k} = \frac{1}{K_f} f_{e,k} \quad . \tag{4.19}$$

This approach can only be applied if the force measurement can be assumed to have no delay and sufficiently high bandwidth. It has to be considered, however, that the external force correlates with the linear motor position. This means that a feedback loop is closed via the measured disturbance feedforward signal which may destabilize the closed-loop.

As during interaction the external force correlates with the linear motor position, a feedback loop is closed which may destabilize the closed-loop otherwise.

4.3.3 Friction Feedforward

The control law (4.17) leads to a stable closed-loop behaviour. However, due to the friction term in (4.11) and the fact that no integrator is present in the feedback loop, a steady-state regulation error occurs. Furthermore, around the change of sign of the motor velocity, the stick-slip phenomenon can be observed. To overcome these problems, the control law (4.17) is expanded with a friction feedforward term, based on the static friction model identified in Section 2.2.1. Together with the known disturbance feedforward term from (4.19) the final control law becomes

$$u_k = -\mathbf{k}^{\mathrm{T}}(\bar{\mathbf{x}}_k - \mathbf{x}_k) + \bar{\mathbf{c}}_m^{\mathrm{T}} \bar{\mathbf{x}}_k + r_m x_{d,k} + \frac{1}{K_i} \left(\bar{f}_{f,k}(\bar{v}_k) - f_{e,k} \right) \tag{4.20a}$$

$$\bar{f}_{f,k}(\bar{v}_k) = f_0 + \left(f_c + f_{s,a} e^{-\left| \frac{\bar{v}_k}{v_s} \right|} \right) \frac{2}{\pi} \arctan\left(k_{tan} \bar{v}_k \right) \quad . \tag{4.20b}$$

The corresponding control parameters used for implementation are given in Table B.2 and Table B.3. The final control strategy is illustrated in Figure 4.1.
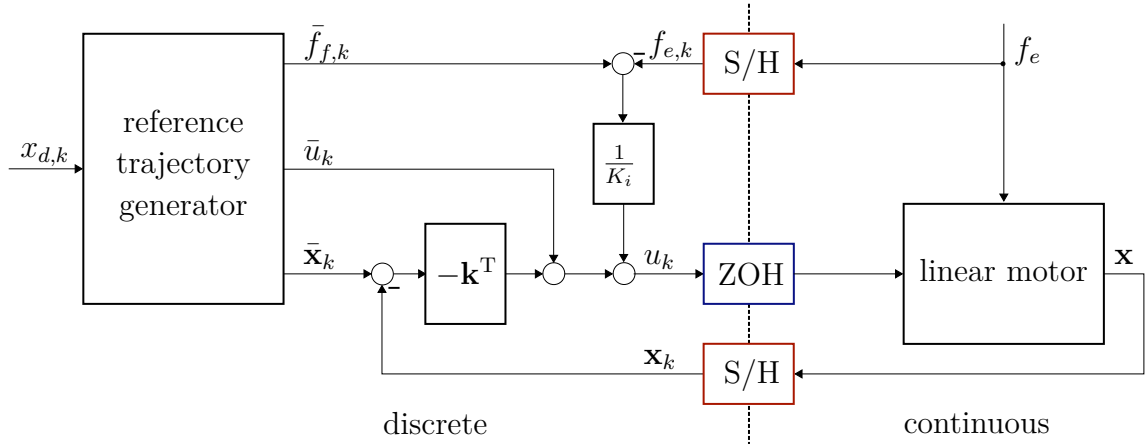
Figure 4.1: Block diagram of the position control structure.

4.4 Admittance Control Strategy

The simple admittance control law proposed in Section 3.5 has the disadvantage that the bandwidth of the position control loop directly influences the maximum environment stiffness for which the interaction control is stable. In the following section, an admittance control law that compensates for the inner control loop similar to Section 3.5.1 is derived.

As a result of the last section, the position-controlled linear motor can be described with the transfer function $G_m(z)$. Friction effects and environmental coupling are already compensated at this point. In the z-domain, the linear motor position can then be expressed as

$$x_z(z) = G_m(z) \left[x_{r,z}(z) + G_{ad}(z) f_{e,z}(z) \right] \quad . \tag{4.21}$$

Comparing (4.21) to the desired linear motor response

$$x_z(z) = G_m(z) x_{r,z}(z) + G_{ve}(z) f_{e,z}(z) \quad , \tag{4.22}$$

yields the admittance controller transfer function

$$G_{ad}(z) = \frac{G_{ve}(z)}{G_m(z)} \quad . \tag{4.23}$$

Compared to the control law (3.32) it does not include the disturbance-input to position-output transfer function. The losed-loop stability including the admittance controller (4.23) is independent of the inner control loop and depends on the environment, the sampling rate and the VE parameters (see A.1). In order to further reduce these dependencies, in the next section an adaptive algorithm is derived. Under the assumption

of known environment dynamics the admittance control law is adapted such that the closed-loop dynamics match exactly the ideal dynamics of the desired continuous system.

4.4.1 Adaptive Admittance Controller

In this section it is assumed that an estimate of the environment impedance transfer function $\hat{G}_e(s)$ is available each timestep, for example by means of online identification presented in Section 2.3. For simplicity it is further assumed that the environment consists of a single stiffness and $G_e(s) = k_e$ [46, pp. 237]. A static spring without damping represents also the worst-case passive linear environment as it is not able to dissipate any excess energy. Furthermore, $G_{ve}(s)$ is assumed of second-order as defined in (4.3) with

$$0 < d_t < 2\sqrt{k_t m_t} \tag{4.24}$$

fulfilled (oscillatory dynamics).

The idea of the *adaptive admittance controller* (AAC) is to calculate the ideal closed-loop transfer function $T^i_{x_r,x}(s)$ based on the known transfer functions $G_{ve}(s)$ and $\hat{G}_e(s)$ which after discretizing yields the stable transfer function $T^i_{x_r,x}(z)$. Subsequently, the admittance controller $G_{ad}(z)$ is adapted such that the actual closed-loop transfer function $T_{x_r,x}(z)$ has the same poles as $T^i_{x_r,x}(z)$. Closed-loop stability of $T_{x_r,x}(z)$ can be guaranteed if $\hat{k}_e = k_e$ is fulfilled.

The target closed-loop dynamics for this situation were already derived in (3.11), which can be represented with the transfer functions $G_{ve}(s)$ and $G_e(s)$ as

$$T^i_{x_r,x}(s) = \frac{1}{1 + G_{ve}(s)G_e(s)} \quad . \tag{4.25}$$

Discretizing yields

$$T^i_{x_r,x}(z) = \frac{n_i(z)}{(z - z_{1,i})(z - z_{2,i})} \quad , \tag{4.26}$$

where $n_i(z)$ represents the numerator polynomial, and the poles $z_{k,i}$ are calculated via

$$z_{k,i} = exp\left(\frac{-d_t \pm \sqrt{d_t^2 - 4m_t(k_t + k_e)}}{2m_t}T_s\right) \quad . \tag{4.27}$$

To derive the actual closed loop transfer function, Figure 4.2 shows the situation of the admittance-controlled linear motor in contact with an environment. The closed-
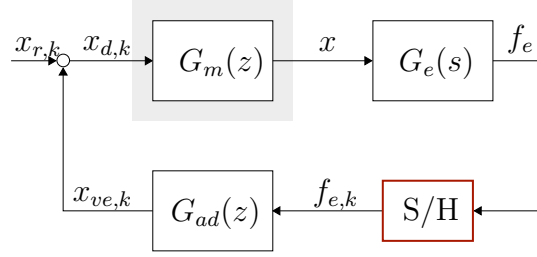
Figure 4.2: Block diagram of the admittance control structure in contact with an environment.

loop transfer function from the reference input x_r to x follows with the admittance controller (4.23) to

$$T_{x_r,x}(z) = \frac{G_m(z)}{1 + G_{ve}(z)G_e(z)} \quad . \tag{4.28}$$

$G_m(z)$ is stable and can be separated to $T_{x_r,x}(z) = G_m(z)\bar{T}_{x_r,x}(z)$. Assuming zero-order hold discretization, the discrete VE transfer function can be written as

$$G_{ve}(z) = \frac{n_1 z + n_0}{(z - z_1)(z - z_2)}, \tag{4.29}$$

and the term $\bar{T}_{x_r,x}(z)$ is expanded to

$$\bar{T}_{x_r,x}(z) = \frac{n(z)}{(z - z_1)(z - z_2) + (n_1 z + n_0)k_e} \quad . \tag{4.30}$$

The goal of the AAC is to match the denominators of $\bar{T}_{x_r,x}(z)$ and $T^i_{x_r,x}(z)$ by increasing the damping parameter of the virtual environment. This means that with (4.26) and (4.30)

$$z^2 + (k_e n_1 - \bar{z}_1 - \bar{z}_2)z + \bar{z}_1\bar{z}_2 + k_e n_0 \stackrel{!}{=} z^2 + (-z_{1,i} - z_{2,i})z + z_{1,i}z_{2,i} \tag{4.31}$$

must hold for every polynomial coefficient. $\bar{z}_i$ are the poles of the augmented VE $\bar{G}_{ve}(z)$ that fulfil the above equation. Because of (4.24) the poles of the ideal transfer function are a pair of complex conjugate values, $z_{1,i} = z^*_{2,i}$ and the same is assumed for $\bar{z}_k$. Then, the coefficients of the lowest order polynomial coefficients in (4.31) become

$$k_e n_0 + \bar{z}\bar{z}^* = z_i z^*_i \tag{4.32a}$$

$$k_e n_0 + e^{(\bar{s}+\bar{s}^*)T_s} = e^{(s_i+s^*_i)T_s} \tag{4.32b}$$

$$, \tag{4.32c}$$

which can be further simplified with $s + s^* = 2\,\mathrm{Re}\{s\}$ to

$$k_e n_0 + e^{-\frac{\bar{d}_t}{m_t}T_s} = e^{-\frac{d_t}{m_t}T_s} \quad . \tag{4.33}$$

Substituting the estimate of the environment stiffness $\hat{k}_e$ into (4.33) and solving for the damping factor of the augmented VE

$$\bar{d}_t = -\frac{m_t}{T_s}\ln\left(e^{-\frac{d_t}{m_t}T_s} - \hat{k}_e n_0\right) \quad , \tag{4.34}$$

leads to the updated admittance control law

$$\bar{G}_{ad}(z) = \frac{\bar{G}_{ve}(z)}{G_m(z)} \quad , \tag{4.35}$$

where

$$\bar{G}_{ve}(z) = \mathcal{Z}\left\{\frac{1}{m_t s^2 + \bar{d}_t s + k_t}\right\} \quad . \tag{4.36}$$

The adaption algorithm performs the calculations (4.34), (4.36) and (4.35) every time a new estimate $\hat{k}_e$ is available. When contact is lost, the algorithm switches automatically to the original admittance control transfer function (4.23). The effect of the adaption algorithm is illustrated in Figure 4.3. For this simulation example, an environment stiffness $k_e = 11\,\mathrm{kN/m}$ and a sampling time $T_s = 0.2\,\mathrm{ms}$ is chosen. With these parameters the closed-loop system is unstable if the standard admittance controller (4.23) is used. This behaviour can also be verified with (4.33). Figure 4.3a shows the original discrete VE $G_{ve}(z)$ in comparison with the VE transfer function $\bar{G}_{ve}(z)$ which results from the adaption. The admittance controller is composed from $\bar{G}_{ve}(z)$, according to (4.35). It does not only stabilize the closed-loop but the resulting transfer function also resembles perfectly the desired one (see Figure 4.3b).

(a) Original and adapted VE

(b) Closed-loop transfer functions
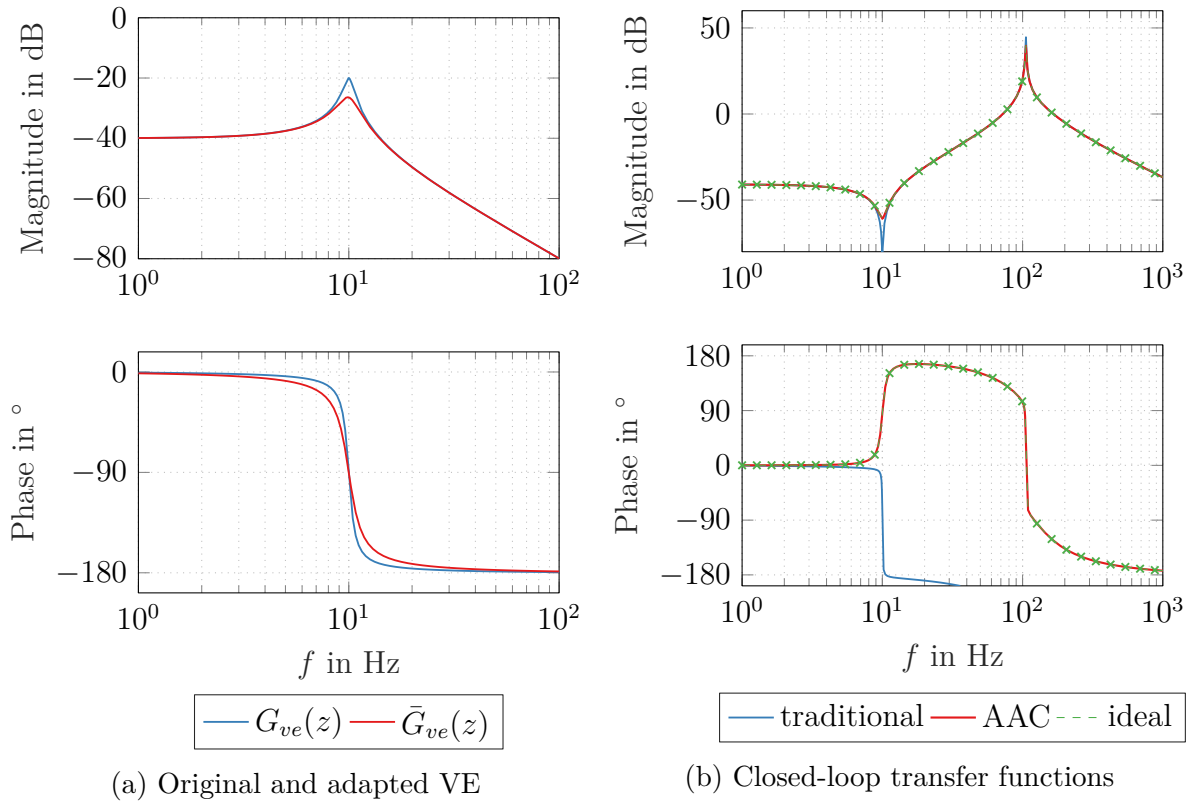
Figure 4.3: Effect of the AAC to the augmented VE and the discrete closed-loop transfer functions. Following parameters are used: $k_e = 11\,\text{kN/m}$, $T_s = 0.0002\,\text{s}$ and $G_{ve}(s)$ according to Table B.4

.

4.5 Conclusion

The final control structure is illustrated in Figure 4.4. Compared with traditional admittance control, the structure developed in this section features an environment estimation block and an adaptive admittance control transfer function. The next section deals with the implementation of the velocity measurement emulation.
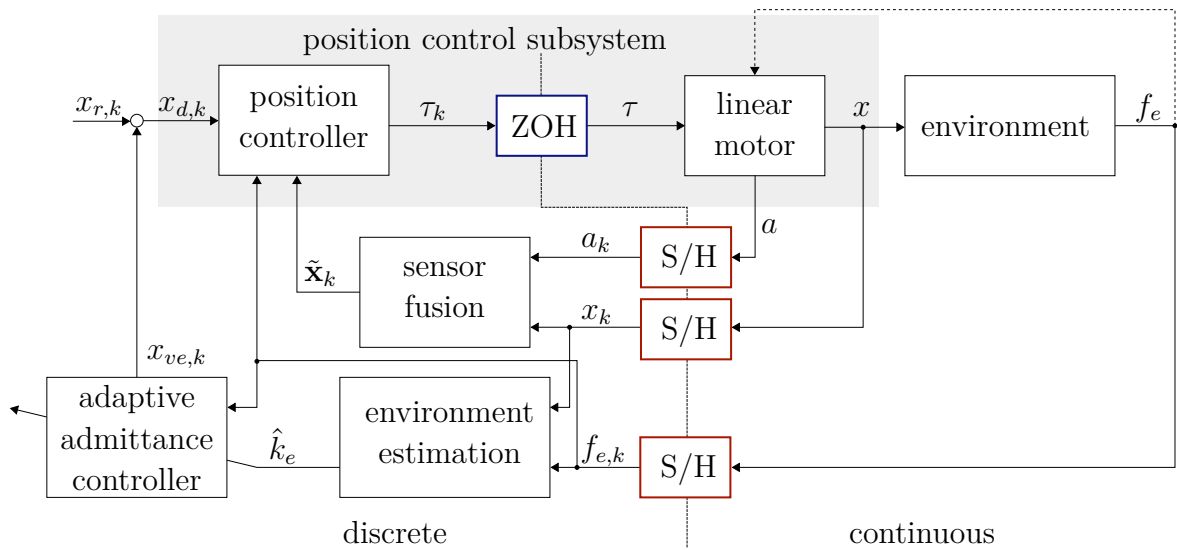
Figure 4.4: Complete interaction control structure.

Chapter 5

Implementation

This chapter covers details on the implementation of the control algorithms developed in the last Chapter.

5.1 Test Rig Hardware

The controllers developed in the last chapter are implemented digitally on a `dSPACE` `MicroLabBox` rapid prototyping box. The linear motor is a `LinMot` PS01-23x80F which is connected to the `MicroLabBox` via a local LAN connection. It features an integrated position measurement, which emulates an incremental encoder interface. The quantization interval of the position measurement is $16\,\mu$m. A `KM26z` force sensor of `ME-Meßsysteme` is used with a maximum measurement range of $50\,$N and a natural frequency of $5\,$kHz.

5.2 Velocity Signal Synthesis

As pointed out in Section 4.3.1, a state-observer approach to obtain the linear motor velocity produces unsatisfactory results. Numerical differentiation does not improve the situation either because this operation increases the noise in the signal. Low pass filtering, on the other hand, causes lag and is therefore no option either. To overcome this problem, a `TLA288D01` mechanical impedance sensor [54] from PCB Piezotronics is attached to the mounting plate of the linear motor. It features an acceleration measurement port that can be used in connection with a 482C05 signal conditioner also from PCB Piezotronics [55]. The acceleration sensor has a high-pass characteristic, which means that is not possible to measure static accelerations. The obtained signal is further afflicted with offset and considerable noise due to its sensitivity. All these
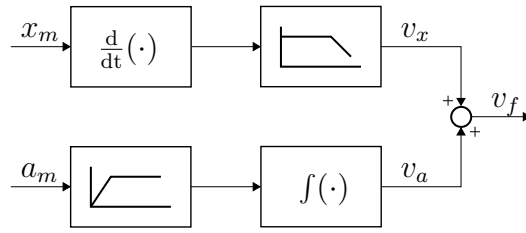
Figure 5.1: Schematic view of a sensor fusion approach of an acceleration- and a position signal to obtain a velocity estimate.

negative properties hardly influence the application of the acceleration sensor in the sensor fusion application as the following paragraphs will show.

5.2.1 Sensor Fusion Principle

Figure 5.1 shows an intuitive approach to a sensor fusion algorithm to obtain a velocity signal by combining information of a measured position signal x with an an acceleration measurement a. x is numerically differentiated and subsequently filtered by a low-pass $G_{lp}(s)$. This procedure removes noise and results in a velocity estimate v_x which suffers from phase lag as mentioned before. The acceleration signal, in turn, is filtered by through a high-pass filter $G_{hp}(s)$ to remove the offset. Integrating the filtered signal leads to a velocity component v_a, which contains only the high-frequency components. The integration operation also removes noise from the signal. The signal v_a does not suffer from phase lag. Both intermediate signals are then combined to obtain the velocity $\tilde{v}$. The high-pass and the low-pass filter are chosen such that $G_{hp}(s) + G_{lp}(s) = 1$, yielding complementary filters.

5.2.2 Observer-Based Approach

Another sensor fusion approach is presented by Zhu and Lamarche in [56]. It is based on designing a state-space observer for the linear double integrator system

$$\frac{\mathrm{d}}{\mathrm{dt}} \begin{bmatrix} x \\ v \end{bmatrix} = \underbrace{\begin{bmatrix} 0 & 1 \\ 0 & 0 \end{bmatrix}}_{\mathbf{A}_x} \begin{bmatrix} x \\ v \end{bmatrix} + \underbrace{\begin{bmatrix} 0 \\ 1 \end{bmatrix}}_{\mathbf{B}_x} a \tag{5.1}$$

An offset of the acceleration measurement can be considered by $a_m = a + c$. The Luenberger observer follows directly to

$$\frac{\mathrm{d}}{\mathrm{dt}} \begin{bmatrix} \tilde{x} \\ \tilde{v} \\ \tilde{c} \end{bmatrix} = \begin{bmatrix} 0 & 1 & 0 \\ 0 & 0 & -1 \\ 0 & 0 & 0 \end{bmatrix} \begin{bmatrix} \tilde{x} \\ \tilde{v} \\ \tilde{c} \end{bmatrix} + \begin{bmatrix} 0 \\ 1 \\ 0 \end{bmatrix} a_m + \mathbf{L} (x_m - \tilde{x}) \quad . \tag{5.2}$$

where the observer matrix $\mathbf{L}$ determines the influence of each of the two measurements on the estimated values. The observer-based approach provides very similar results as the filter-based approach in the previous section regarding velocity reconstruction. Additionally, however, the observer structure delivers a position signal with smoothed out quantization noise. Therefore this approach is chosen in this work to provide the measurements for the position controller. For the digital implementation, (5.2) is discretized to

$$
\begin{bmatrix} \tilde{\mathbf{x}}_{k+1} \\ c_{k+1} \end{bmatrix} = \begin{bmatrix} \boldsymbol{\Phi}_x & \boldsymbol{\Phi}_{xc} \\ \mathbf{0} & 1 \end{bmatrix} \begin{bmatrix} \tilde{\mathbf{x}}_k \\ c_k \end{bmatrix} + \begin{bmatrix} \boldsymbol{\Gamma}_x \\ 0 \end{bmatrix} a_{m,k} + \mathbf{L_d} \left(x_{m,k} - \tilde{x}_k \right) \quad . \tag{5.3}
$$

with the *zero-order hold* procedure.

Figure 5.2 shows the effectiveness of the sensor fusion approach and the shortcomings of the linear state observer structure (4.18) for the linear motor with large friction. While the velocity estimate from the observer is acceptable when the velocity sign does not change, it fails once v reaches zero. This happens because the assumption $f_{d,k} = \text{const}$ is violated as the effective friction force changes. Even with friction feedforward compensation the situation does not improve much, since especially around zero velocity the static model of Section 2.2.1 is only a rough approximation of the rather complex friction phenomena. In contrast, Figure 5.2b and Figure 5.2d show that the sensor fusion scheme (5.2) is able to provide a good velocity measurement. As an immediate effect, the position controller is able to significantly reduce linear motor sticking around a change of velocity sign.

(a) $f = 0.25\,\text{Hz}$, linear observer

(b) $f = 0.25\,\text{Hz}$, sensor fusion

(c) $f = 2\,\text{Hz}$, linear observer

(d) $f = 2\,\text{Hz}$, sensor fusion
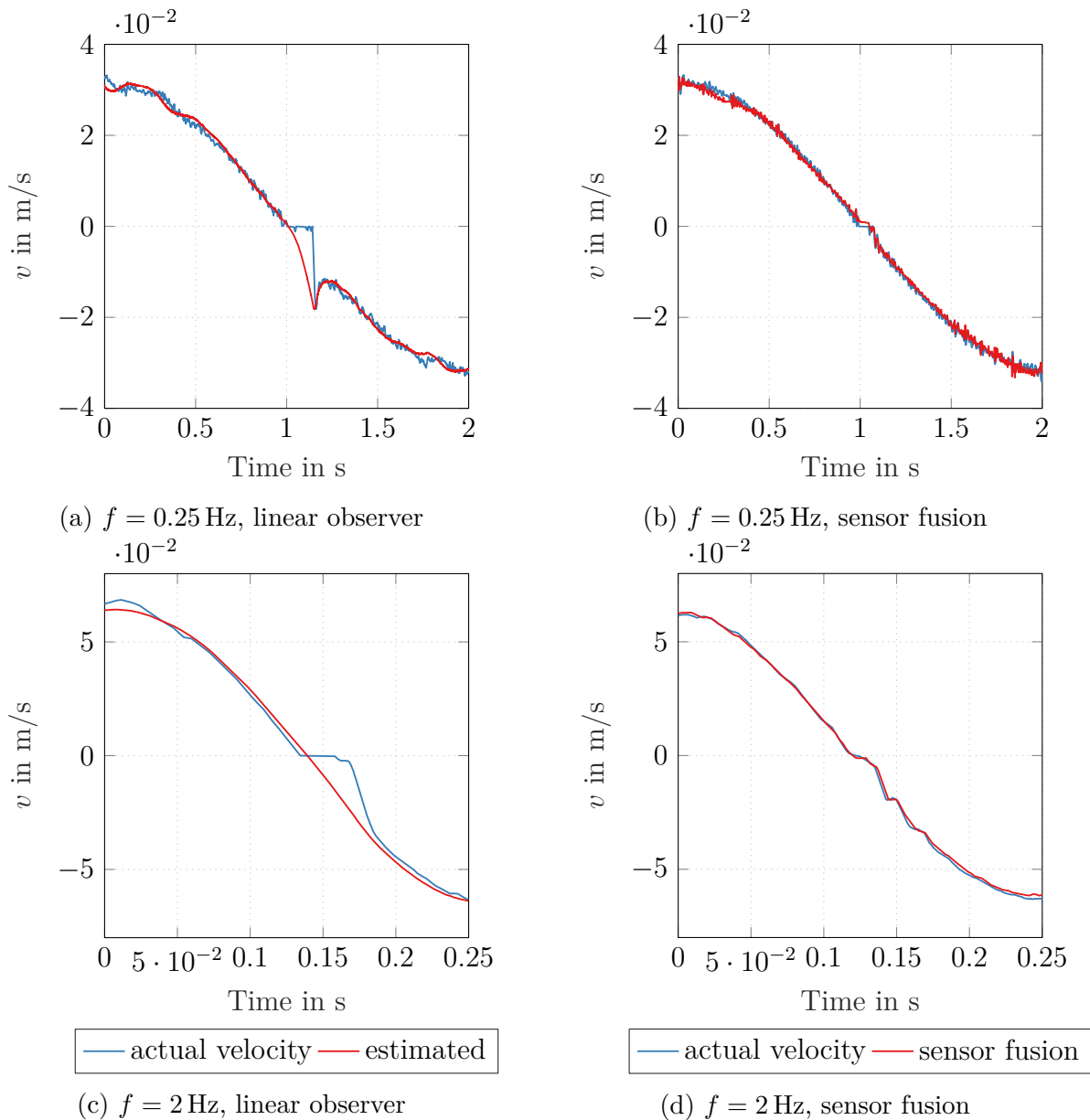
Figure 5.2: Actual linear motor velocity (blue line) obtained by offline filtering the measured position signal compared to the velocity estimate obtained by the linear observer (4.18) (a,c) and sensor fusion (5.2) (b,d). The linear motor was actuated to follow sine references with an amplitude $A = 2\,\text{cm}$ in (a,b) and $A = 5\,\text{mm}$ in (c,d). The linear motor barely gets stuck in (b,d) compared to (a,c) because the updated velocity measure is already incorporated into the controller in these experiments.

Chapter 6

Experimental Results

In this chapter, measurement results from the interaction control test rig are presented. It is divided into two parts: The first part is solely dedicated to the linear motor position control loop. Each component of the control strategy, developed in Section 4.3, is examined for its contribution to the control goal. The effectiveness of the sensor fusion approach to reduce sticking of the linear motor is shown. Additionally, the friction feedforward method as described in Section 4.3.3 is examined for practicability. The section concludes with a study of the disturbance rejection properties of the position-controlled linear motor.

The second part of this chapter focuses on the closed admittance loop. The effectiveness of the admittance controller to reproduce the desired model behaviour is examined by measurements which are compared to simulations of the contact scenario. This section further focuses on the influence of the inner control loop settings, especially the friction compensation approach, on the interaction behaviour. Ultimately, the ability of the adaptive admittance control approach, presented in Section 4.4.1 is shown.

6.1 Position Control Loop

In Chapter 4, nonlinear friction in combination with the absence of a velocity measurement has been identified as the main factors to compromise position control performance. Their influence on the measurement results are therefore examined at first.

6.1.1 Influence of Velocity Measurement

Figure 6.1 shows the internal model and measured position $\bar{x}$ and x and the position error with respect to a sine reference trajectory with a frequency $f = 0.25\,\text{Hz}$ and an amplitude of $A = 2\,\text{cm}$. Moreover, the velocities $\bar{v}$ and v of the internal model and the actual linear motor, respectively, are shown, including the velocity error. As the actual

velocity is not measured for the traditional RLQG controller with state observer, the position measurement is filtered and differentiated with a *Savitzky-Golay* filter [57]. In this experiment, the friction feedforward is not active.

It can be seen that the observer-based RLQG controller cannot keep track of the reference trajectory at velocity reversal and the linear motor gets stuck. Apart from this behaviour, it shows a similar error characteristic as the RLQRv. This can be attributed to the state estimation error, which has its maximum around zero velocity (see Figure 5.2). Thus, the controller does not quickly register that the linear motor sticking and cannot act accordingly.

Including the synthesized velocity signal into the control scheme immediately improves the position-following performance. The linear motor still stalls, but the effect is much less severe than with the observer-based approach.

Figure 6.2 shows the situation for a reference trajectory with an amplitude of $A = 5\,\mathrm{mm}$ and a frequency of $f = 2\,\mathrm{Hz}$. Again, the flat peak phenomenon occurs, particularly in the observer-based design. In this case however, the position trajectory realized with the observer-based controller lags visibly behind the reference model.

From the measurements it can be concluded that simple position measurement is insufficient to accurately control systems with static friction. With regard to interaction control, two problematic phenomena are observed: Firstly, sticking of the linear motor, which causes jerky motion and induces significant disturbance at multiples of the reference signal frequency. Secondly, phase lag of the actual linear motor motion compared to the reference model occurs. This additional lag is not considered in the admittance control law and may compromise contact stability.
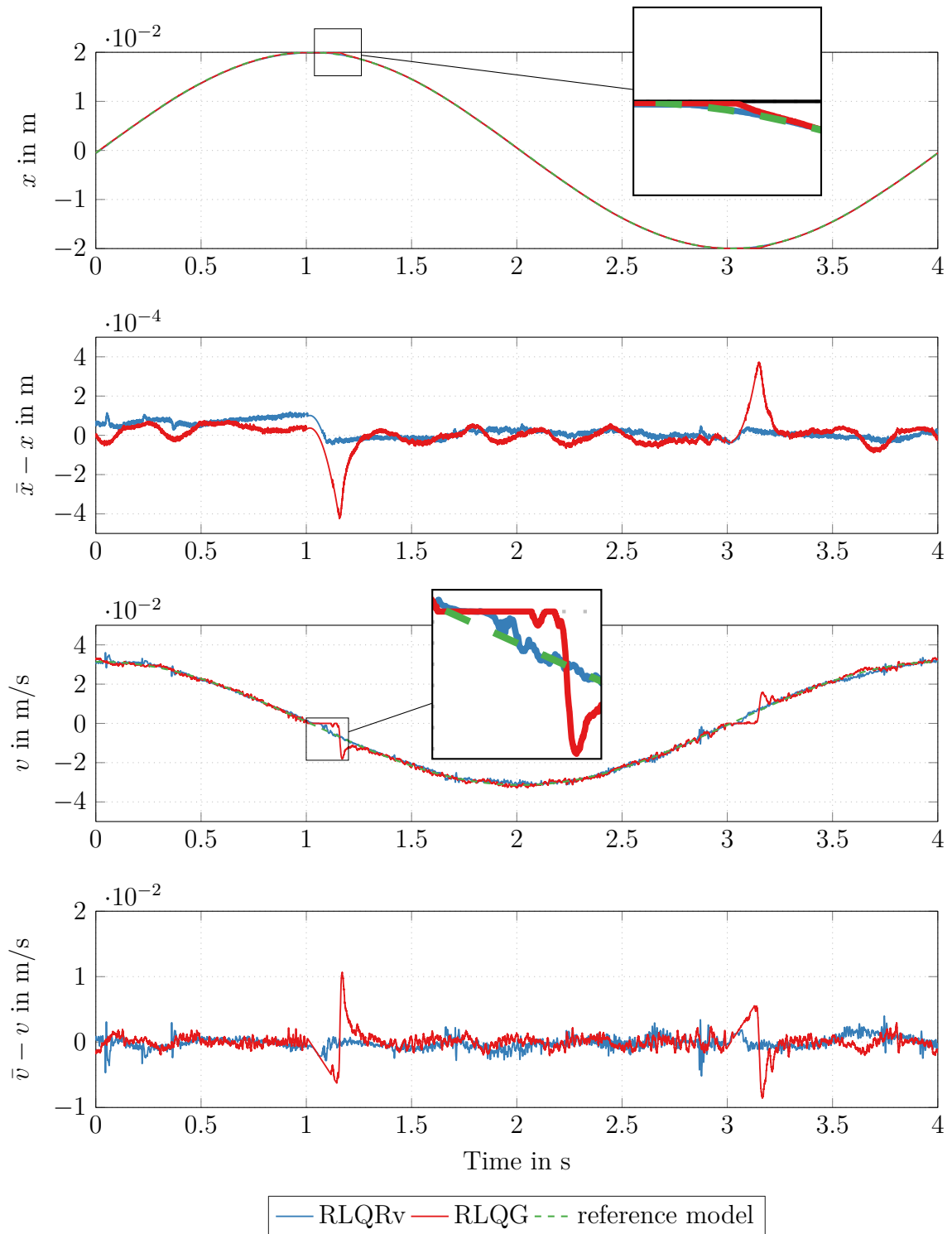
Figure 6.1: Model reference following capability of the RLQRv to the RLQG for a reference signal x_d with $A = 2\,\text{cm}$ and $f = 0.25\,\text{Hz}$.
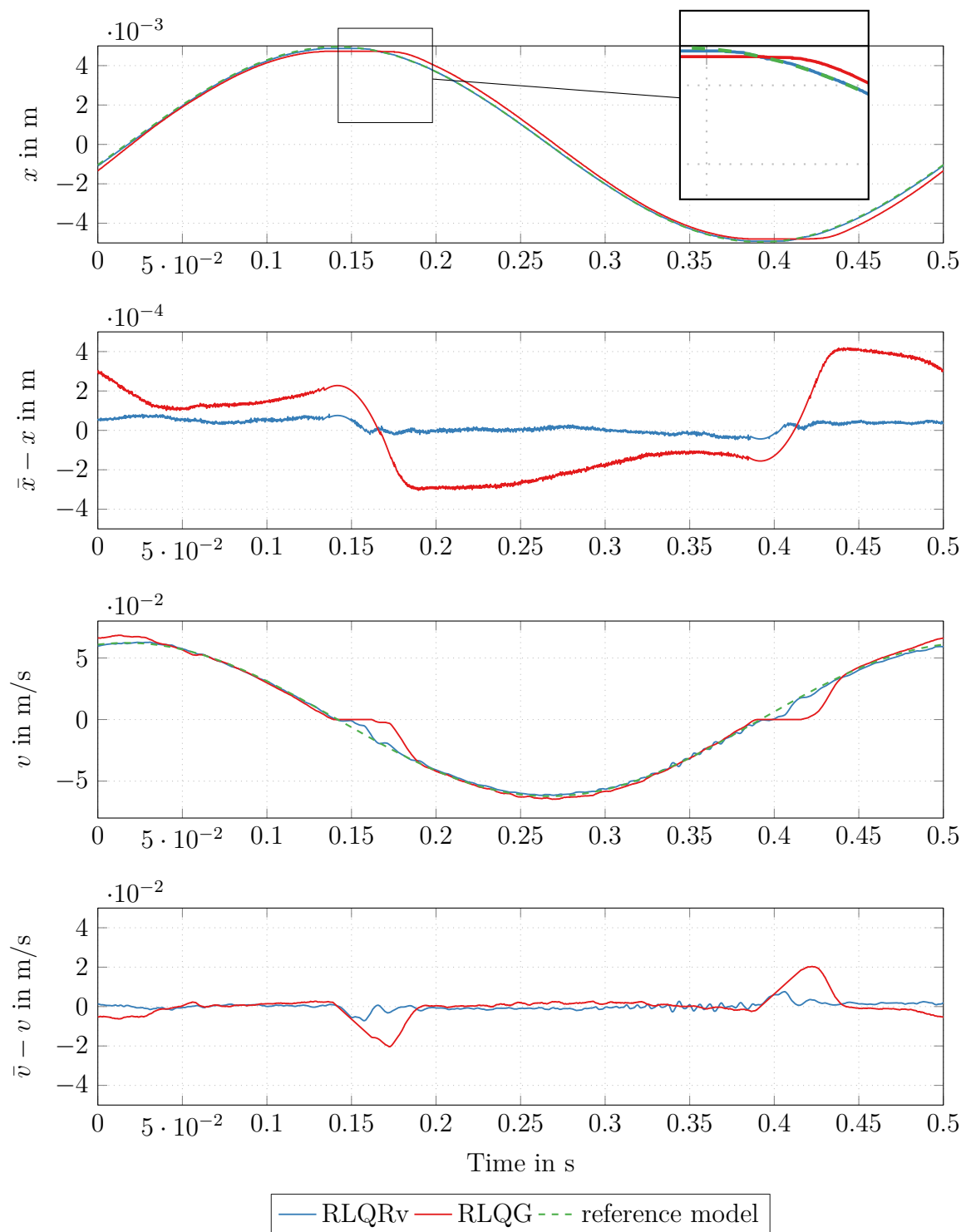
Figure 6.2: Model reference following capability of the RLQRv to the RLQG for a reference signal x_d with $A = 5\,\text{mm}$ and $f = 2\,\text{Hz}$.

6.1.2 Influence of Friction Feed-forward

In this section, the effect of friction compensation on the position control loop is examined. The RLQRv approach serves as underlying position controller. The experiments of the last section are repeated with the linear motor, but this time with additional friction feedforward. Figure 6.3 again shows the position and velocity signals, together with the corresponding errors with respect to the internal reference model. It can be seen that the feedforward term slightly improves the position following accuracy. In Figure 6.4, the impact of the feedforward term is more evident. The linear motor does hardly get stuck any more. Instead, the velocity error around velocity reversal lashes out in the opposite direction as compared with the measurement without feedforward. This clearly indicates overcompensation which may be attributed to the friction identification approach described in Section 2.2.1, where static friction parameters result by averaging over the whole end-effector workspace.

For a final comparison of the position control experiments, Table 6.1 shows the *mean-squared-error* (MSE) between the actual linear motor position and the reference model position for different controller configurations. It underlines that particularly in the case of higher frequencies, the sensor fusion approach significantly improved position accuracy. Table 6.1 also shows a comparison between two slightly different feedforward concepts. The column *Coulomb + Stribeck* denotes that the full feedforward term (4.20b) is applied. The Stribeck term $f_{s,a}$ can be set to zero for a more conservative feedforward law, where overcompensation is less likely to happen. The column *Coulomb* contains the MSE for measurements with this configuration. Interestingly, for the reference trajectory with $f = 2\,\mathrm{Hz}$, including only Coulomb friction in the feedforward results in a lower MSE compared to the full friction model. This may be caused by the overcompensation, which happens with the full model (see 6.4).

| | Controller | | | |
| | RLQG | RLQRv | | |
Feedforward **Trajectory**	no	no	Coulomb	Coulomb + Stribeck
$A = 2\,\mathrm{cm}$, $f = 0.25\,\mathrm{Hz}$	4.826	1.857	0.414	0.277
$A = 5\,\mathrm{mm}$, $f = 2\,\mathrm{Hz}$	52.048	1.465	0.394	0.611

Table 6.1: *Mean-squared-error* for the position controller with different feedforward configurations.
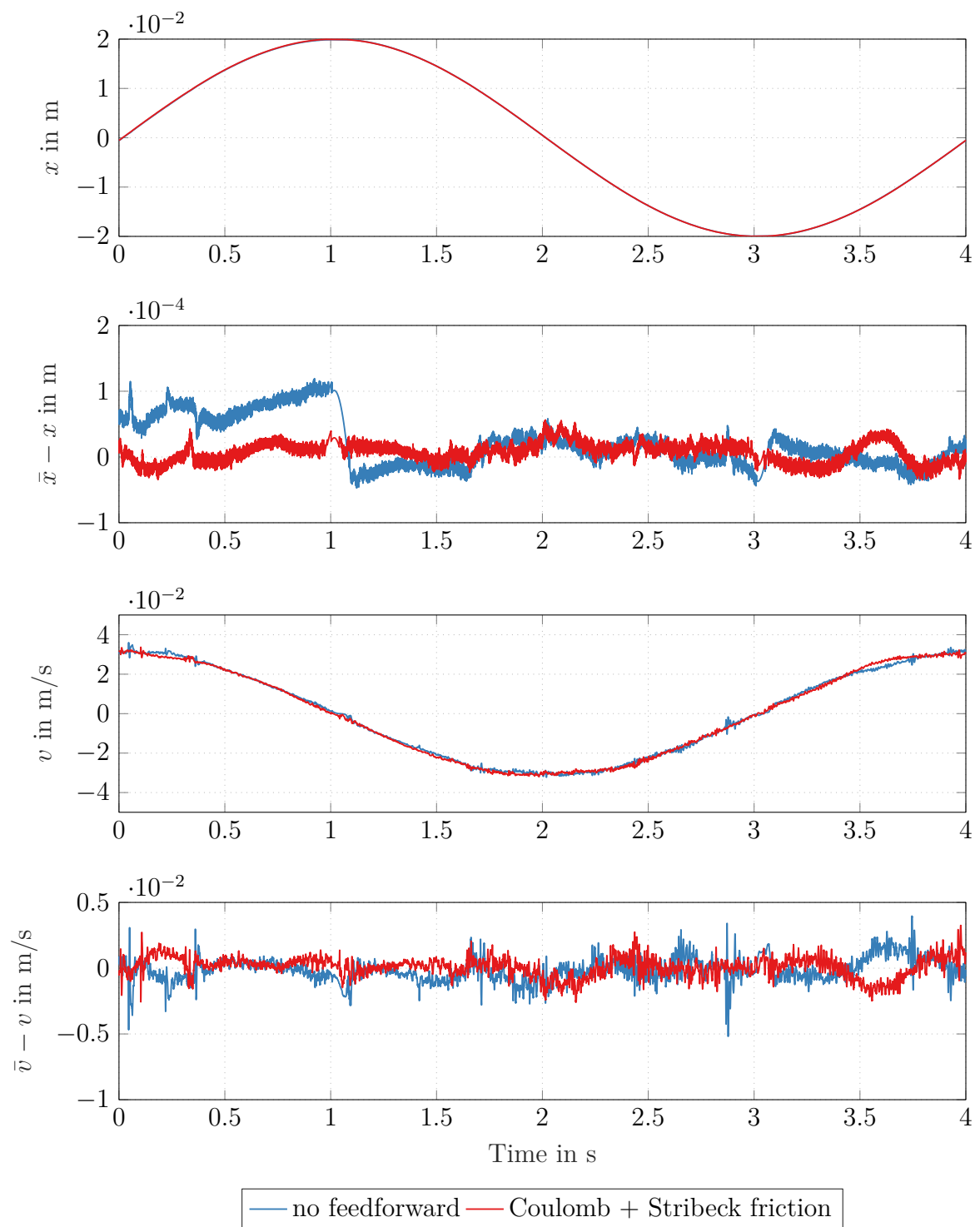
Figure 6.3: Influence of friction compensation on the model reference following capability for a reference signal x_d with $A = 2\,\mathrm{cm}$ and $f = 0.25\,\mathrm{Hz}$.
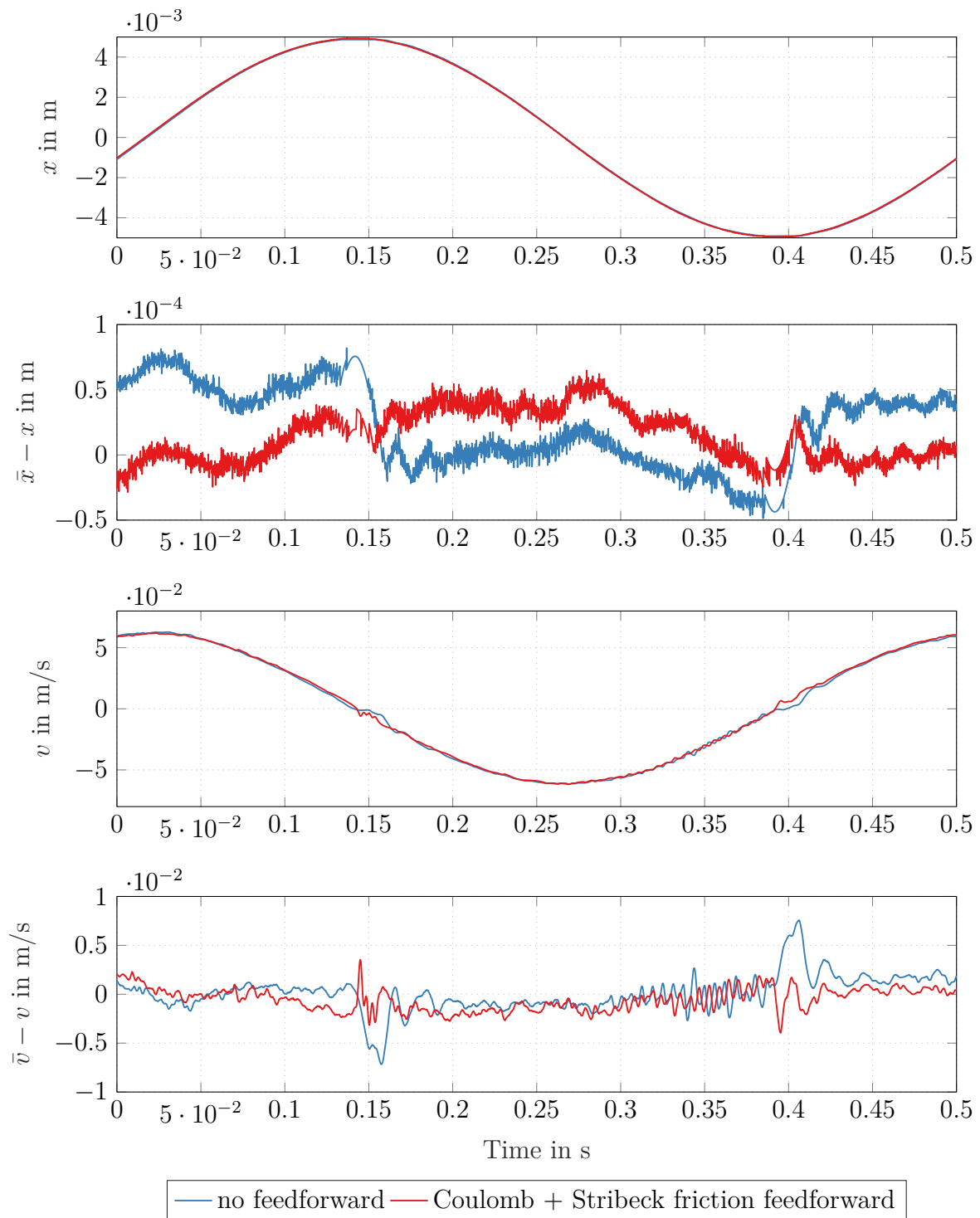
Figure 6.4: Influence of friction compensation on the model reference following capability for a reference signal x_d with $A = 0.005\,\text{cm}$ and $f = 2\,\text{Hz}$.

6.1.3 Disturbance Rejection

In Section 4.3.2, compensation of the known disturbance, by feedforward of the measured external force f_e was introduced to minimize coupling between the manipulator mass with the environment. To evaluate the effectiveness of this approach, an external force is applied to the manipulator, while it is commanded in resting position $x_d = 0$. In addition to the measurement feedforward, the position controller is active in this experiment. Figure 6.5 shows the deviation from the commanded position and the applied force. The maximum error stays within $4\,\text{LSB}$ of the position encoder, which justifies the assumption in 4.4 that the external force feedback from the environment to the manipulator can be neglected.
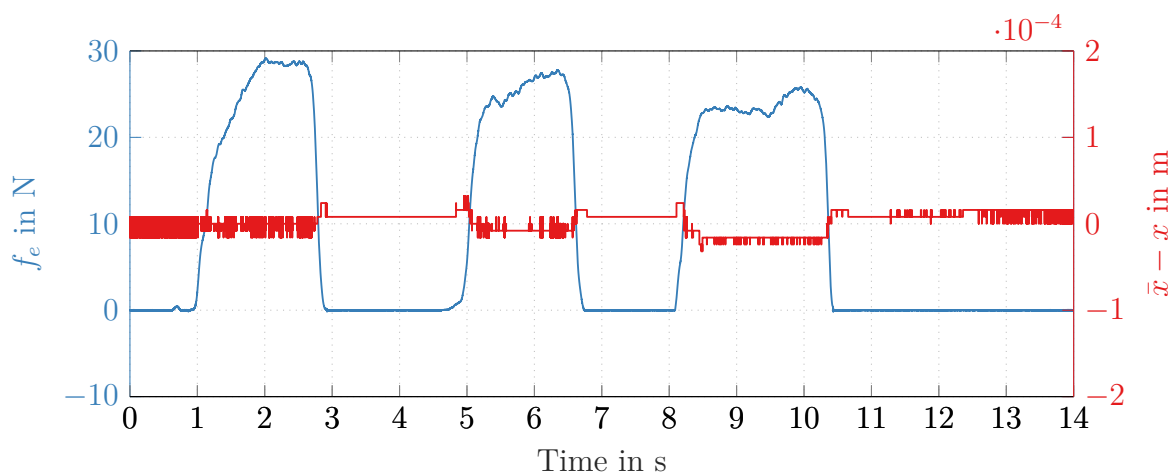
Figure 6.5: Disturbance rejection performance of the position controller.

6.2 Admittance Control Loop

In order to test the performance of the admittance controller developed in Section 4.4, contact experiments are conducted as shown in Figure 6.6. The linear motor is commanded a nominal equilibrium trajectory x_r, which establishes contact with the sample environment. x_r is designed to be at least two times continuously differentiable and $\dot{x}_r = 0$ between two set points $x_{r,0}$ and $x_{r,1}$ during contact establishment. This approach ensures that the manipulator hits the test object always with the same kinetic energy. The parameter $T_{approach}$ defines the time interval of a setpoint change of x_r and determines the impact velocity.

In this section, the standard admittance control law (4.23) is used as interaction controller. A second-order transfer function as in (4.3) is configured as virtual environment, with parameters according to Table B.4. The first series of experiments aim to assess the accuracy of reproducing the desired contact dynamics. Subsequently, the influence of the inner control loop on the interaction control performance is investigated. This chapter concludes with a comparison of the adaptive admittance control approach with the standard admittance control law. Evaluating (A.14) with the parameters of the discretized VE reveals that, with a sampling time of $T_s = 0.2\,\text{ms}$, the closed loop system should be stable for $k_e \leq 10\,\text{kN/m}$ with no adaption. If not explicitly stated otherwise, the RLQRv control law (4.20) with sensor fusion procedure (5.3) is used as position controller.
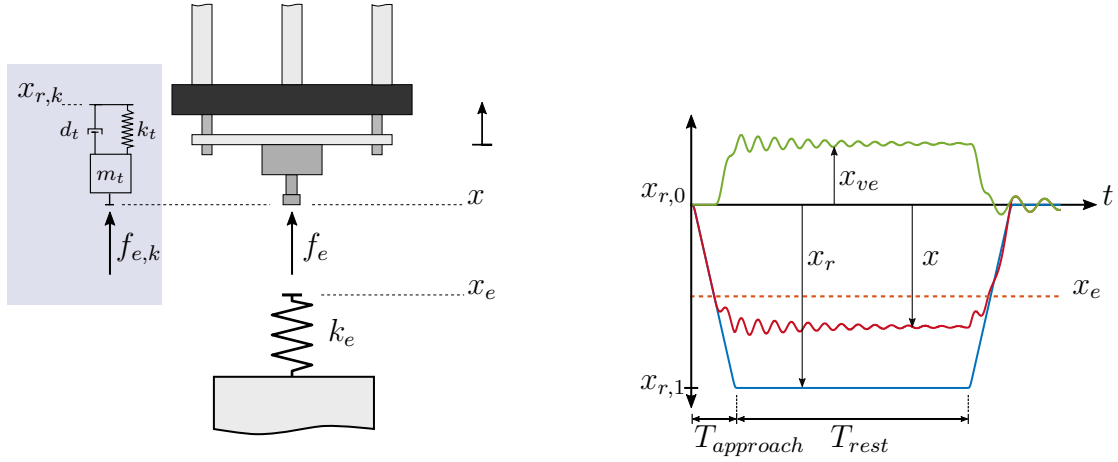
Figure 6.6: Experimental setup for evaluation of the interaction control performance. The plot to the right shows exemplary trajectories of an approach, contact and retreat scenario. $T_{approach}$ determines the impact velocity of the manipulator.

6.2.1 Interaction Performance

The performance of the interaction controller can be assessed by considering three aspects. First of all, the manipulator should follow a reference trajectory in free space. By using an admittance controller with underlying position control loop, this requirement is trivially fulfilled. The following section will therefore exclusively focus on contact situations. Secondly, upon impact the controller should react swiftly enough, such that no force overshoot compared to the ideal behaviour occurs. The third consideration refers to the accuracy the manipulator in achieving the desired closed loop behaviour when continuously in contact. According to (3.11) the ideal closed loop results in a second-order system if the environment can be modelled as linear spring. Its oscillatory behaviour can be described by the decay factor α and the damped natural frequency f_{cl}, which can be calculated to

$$\alpha = \frac{d_t}{2m_t} \tag{6.1a}$$

$$f_{cl} = \frac{1}{2\pi}\sqrt{\frac{(k_e + k_t)}{m_t} - \frac{d_t^2}{m_t}} \tag{6.1b}$$

with the help off (3.12). The steady-state force

$$f_\infty = \frac{k_e k_t}{k_e + k_t}\left(x_e - x_{r,1}\right) \tag{6.2}$$

for constant penetration depth $x_p = x_e - x_{r,1}$ results from substituting $\hat{x}_p(s)$ into (3.11) and applying the *final value theorem* under the consideration of $\hat{f}_e(s) = k_e\hat{x}(s)$.

	Reference Trajectory	
	I	**II**
$T_{approach}$	$1\,\text{s}$	$5\,\text{s}$
T_{rest}	$2\,\text{s}$	
$x_{r,0}$	$0\,\text{m}$	
$x_{r,1}$	$-0.05\,\text{m}$	

Table 6.2: Reference trajectory parameters

Figure 6.7 shows the position and force signals for simulations of an interaction experiment with the setup Figure 6.6, VE parameters according to Table B.4 and a steel spring with $k_e = 2\,\text{k/Nm}$ at the position $x_e = -0.02\,\text{m}$. The reference trajectory parameters are listed in Table 6.2. On basis of the envelope and frequency of the oscillation it is possible to examine, if the desired dynamic behaviour is achieved. In Figure 6.7b a slower impact velocity is chosen compared to Figure 6.7a, which results in a smaller amplitude of the oscillations after impact. It can be observed that the steady state is almost reached, before the manipulator retreats from the environment. Furthermore, it can be seen from the position signals that the amplitude of the position oscillations is in the range of $1.5\,\text{mm}$ in Figure 6.7a and well below in Figure 6.7b. This highlights the importance of accurate position control, as every position error is amplified by k_e to an error in measured force. For all experiments below, the reference trajectory parameters I or II from Table 6.2 are used.

Figure 6.8 shows the measured manipulator position x_m, the interaction force f_e and the amplitude spectrum of f_e for the manipulator interacting with a steel spring with $k_e = 2\,\text{kN/m}$ for reference trajectory I. Additionally, the simulation results from Figure 6.7a are plotted again in Figure 6.8. The comparison of the force peak at first impact ($t = 0.5\,\text{s}$) between the measurement and the simulation shows that the admittance controller is able to react fast enough to prevent force overshoot. After bouncing off once, the manipulator establishes contact with the spring. The envelope of the measured force signal shows a smaller decay rate of the oscillation amplitude than the simulated force. This means that the actual interaction is less damped than the ideal dynamics. The comparison of the force amplitude spectra from the measurement with the simulation confirms that the actual achieved contact dynamics are in good agreement with the desired behaviour.
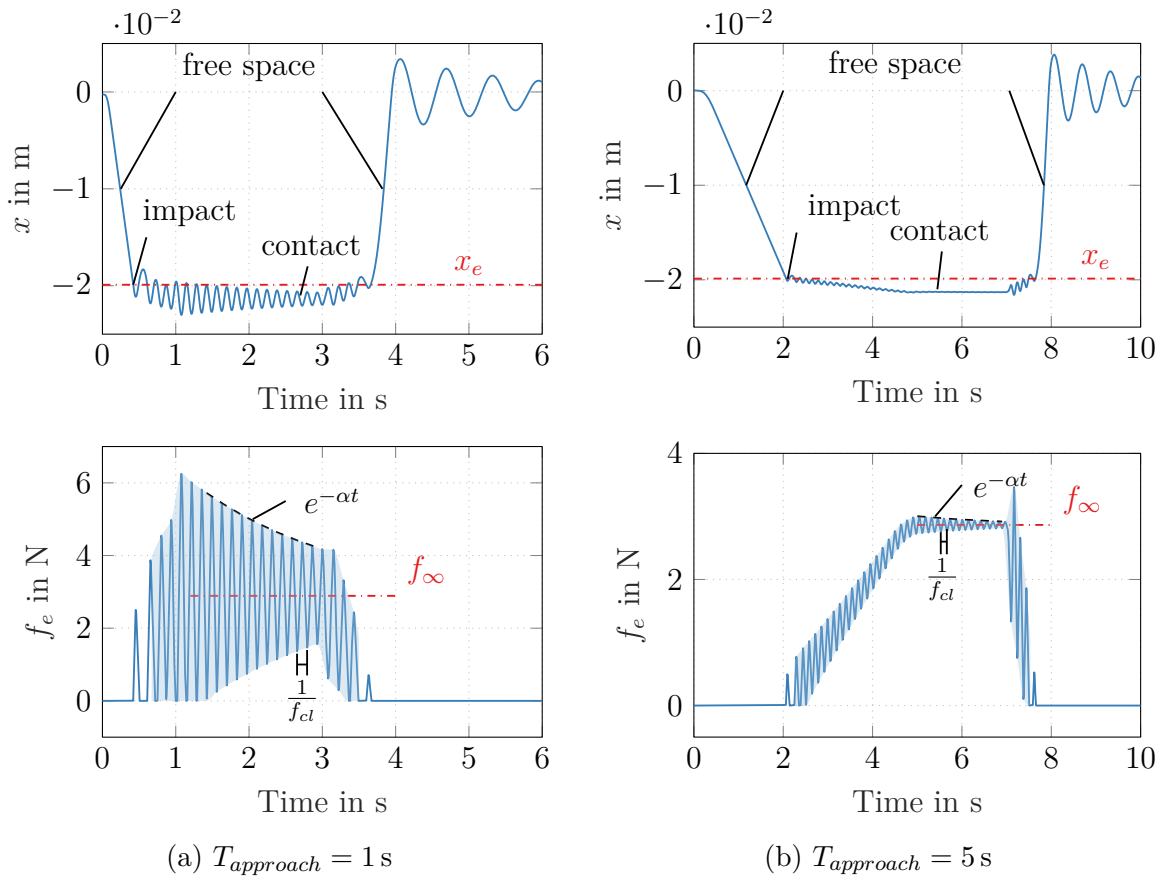
Figure 6.7: Simulated manipulator position and contact force for ideal admittance control with $k_e = 2\,\mathrm{k/Nm}$ and VE parameters according to Table B.4 for two different approach velocities and $x_{r,1} = -0.05\,\mathrm{m}$, $T_{rest} = 2\,\mathrm{s}$. In contact oscillations occur with the natural frequency f_{cl}, the decay rate α and the static interaction force f_∞ which is approached for constant x_r.
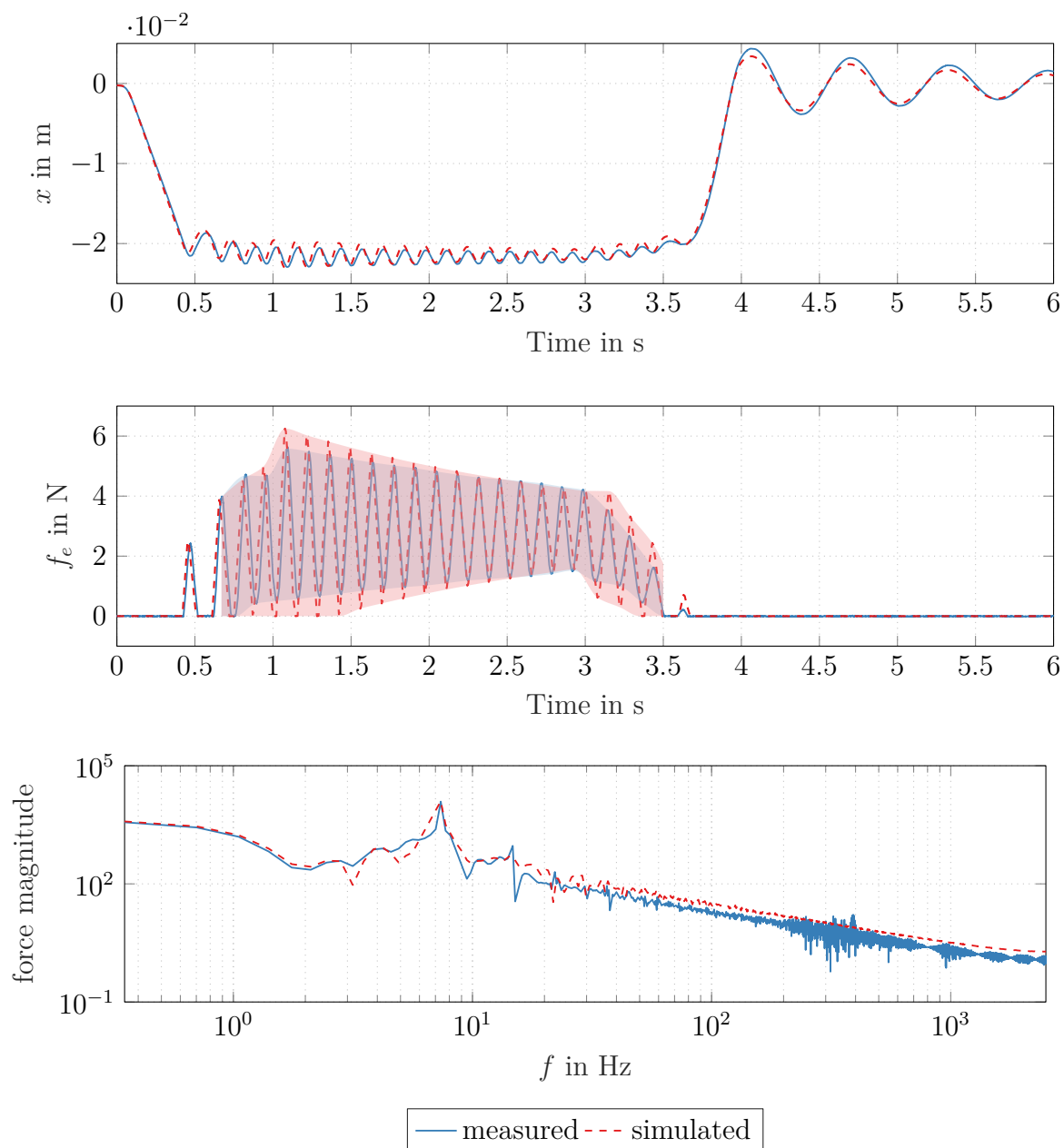
Figure 6.8: Linear motor in contact with a steel spring with $k_e = 2\,\text{kN/m}$ and $T_{approach} = 1\,\text{s}$. The first force peak after impact is almost identical to the simulation, while the decay rate of the measurement is smaller than in the simulation. The force magnitude plot shows that the desired dynamic behaviour can almost be reached.

Figure 6.9 shows the resulting position and force trajectories of the same experiment, but this time with $T_{approach} = 5\,\mathrm{s}$. Again, the simulation of the optimal admittance control is also plotted for comparison. In this experiment, the measured force decays faster than the simulated one, but instead of reaching a stationary force level, a limit cycle occurs. This could be the consequence of friction overcompensation, which was discovered in Section 6.1.2. Another possibility is that the linear motor position control loop reaches its accuracy limits, as the position oscillations during the limit cycle reach an amplitude of just $0.1\,\mathrm{mm}$. During impact and retreat, the force agrees well with the simulation. For the measurements the amplitude spectrum shows notable peaks at three and five times the calculated closed loop natural frequency which supports the claim that friction compensation might not work accurately enough.
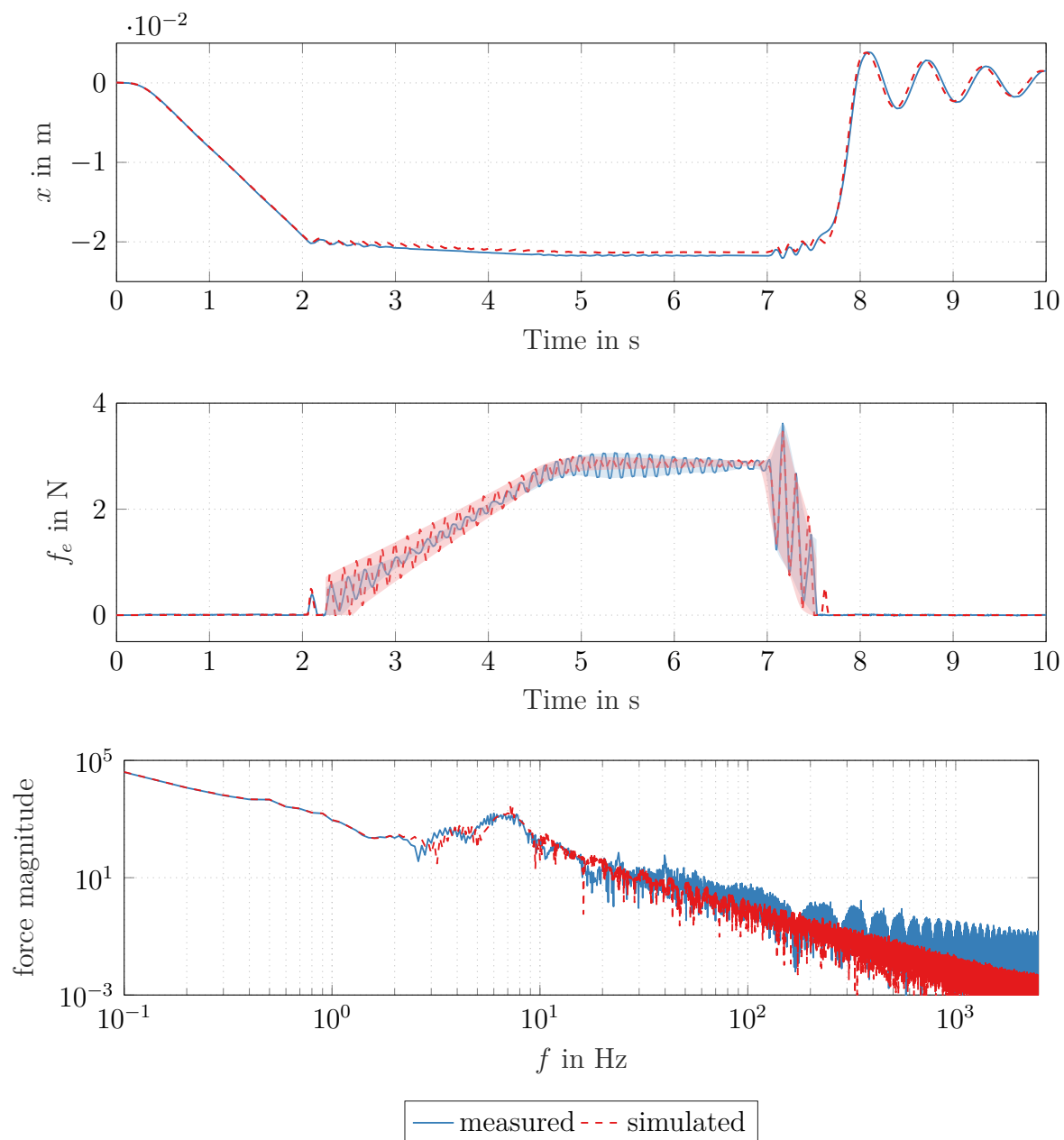
Figure 6.9: Linear motor in contact with a steel spring with $k_e = 2\,\text{kN/m}$ and $T_{approach} = 5\,\text{s}$. The measured force does not decay to a stationary level, but a limit cycle occurs. In the force magnitude spectrum peaks can be seen at odd multiples of the closed-loop natural frequency, which suggest insufficient friction compensation.

Practical Limits of the Admittance Controller

In order to investigate the practical limits of the admittance control strategy, further contact experiments are conducted with environments with increased stiffness. The value k_e of the different objects is identified before the experiment in position control mode. The linear motor is commanded reference trajectory I in the following experiments. Figure 6.10 shows the contact force as well as the force spectra for three objects with $k_e \in \{6\,\text{kN/m}, 10\,\text{kN/m}, 75\,\text{kN/m}\}$. The stiffness $k_e = 10\,\text{kN/m}$ is just the stability boundary for the admittance control parameters Table B.4, while $k_e = 75\,\text{kN/m}$ lies well beyond the stable parameter range. In addition to the measurements, also simulations of the experiment are plotted again to visualize the force trajectory in the ideal case.

Several observations can be made in Figure 6.10. The force peaks after the first impacts agree very well with the simulated values and show no overshoot. This means that the interaction control loop reacts fast enough to let the manipulator absorb a sudden impact. Secondly, the closed loop measurement show no unstable behaviour. Indeed, the manipulator bounces off the object with $k_e = 75\,\text{kN/m}$. However, at some point static contact is established, only to be lost spontaneously after a short time period. Figure 6.10c shows a brief oscillatory behaviour of the manipulator after establishing contact which vanishes and a static contact force results. This behaviour might again be the result of not ideally compensated friction and unmodelled material damping in the environment.

The force amplitude spectra for all experiments in Figure 6.10 show that the actually achieved closed loop dynamics only match the constant component of the desired behaviour. It has to be kept in mind though that the force oscillations in these three correspond to a position oscillation amplitude of $100\,\mu\text{m}$. In contrast, the quantization interval of the position sensor is $16\,\mu\text{m}$ and the achieved position tracking error of the position controller is in the range of $50\,\mu\text{m}$ (see Section 6.1). Hence, the motion control limits as well as the limits of the test rig are reached with these experiments.

An important conclusion is that the disturbances resulting from imperfections in the position control overshadow the destabilizing effects due to sampling. Thus, the adaptive admittance controller proposed in Section 4.4.1 offers renders useless in this case. Furthermore, the importance of accurate motion control in the admittance control scheme is highlighted.

(a) $k_e = 6\,\mathrm{kN/m}$

(b) $k_e = 6\,\mathrm{kN/m}$

(c) $k_e = 10\,\mathrm{kN/m}$

(d) $k_e = 10\,\mathrm{kN/m}$

— measured --- simulated

(e) $k_e = 75\,\mathrm{kN/m}$

— measured --- simulated

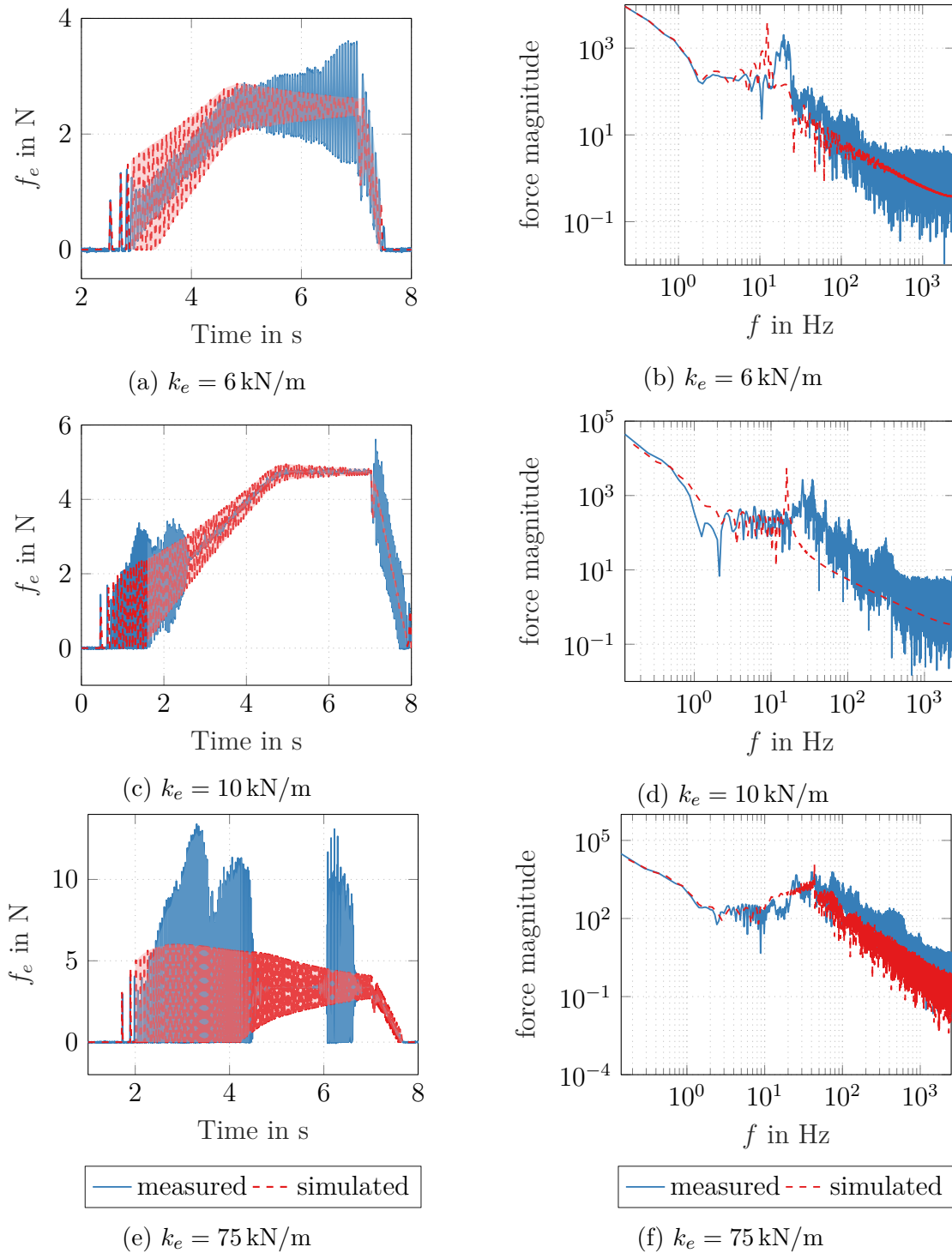(f) $k_e = 75\,\mathrm{kN/m}$

Figure 6.10: Force signal in time- and frequency domain for contact experiments with various environments with higher stiffness. Compared ot the ideal simulated behaviour, the closed-loop oscillations occur at higher frequencies. Also static contact is established and lost again, which is not desired and a indicator that the position-control loop reaches its limits.

6.2.2 Influence of the Inner Control Loop

The results of the experiments in the last section motivate to investigate the influence of different position control loop configurations on the interaction control performance.

Friction Compensation Method

As in the last section, overcompensation of friction is suggested as a possible source of the occurring limit cycles, it is of interest to compare the previous control approach to more conservative designs. The experimental setup is the same as in the last section. Only the type of friction feedforward is changed.

In the following experiment no friction compensation term is applied to the position control law. Figure 6.11 shows the measured forces which occur, when the linear motor approaches the spring as described in Section 6.2. In this case the force amplitude does not decay at all, but seems to develop into a limit cycle. This behaviour is expected, as Section 6.1.2 showed that absence of friction compensation leads to an additional phase lag in the position response of the manipulator, which may destabilize the closed interaction control loop.

If only the Coulomb friction is fed forward, Figure 6.12a shows that for comparably large position amplitudes, the contact behaviour is almost the same as when feedforward includes the Stribeck term as well. However, when approaching the environment more slowly, a limit cycle develops with a higher amplitude than with the model including Stribeck friction.

Summarizing the results so far, it can be said that the friction compensation is crucial for the performance of interaction control. To further improve the interaction control results, more sophisticated friction models would have to be used. But as pointed out in Section 2.2.1, friction is a rather complex phenomenon and difficult to describe. A constructive approach might be to consider the desired environment dynamics earlier in the system design and construct the manipulator accordingly.

Different Position Control Method

To conclude the survey of the influence of the inner control loop to the interaction performance, a different position control approach is compared to the position control architecture which was used so far. The *model following control* (MFC) approach has the same objective as the RLQR, namely shaping the closed loop transfer function such that it behaves like a predefined dynamic model.

The MFC used in this section is tuned such that the closed loop position following performance is similar to that of the RLQR controlled manipulator. The main differences of the MFC to the implemented RLQRv are that the MFC has no acceleration

(a) $T_{approach} = 1\,\text{s}$

(b) $T_{approach} = 5\,\text{s}$
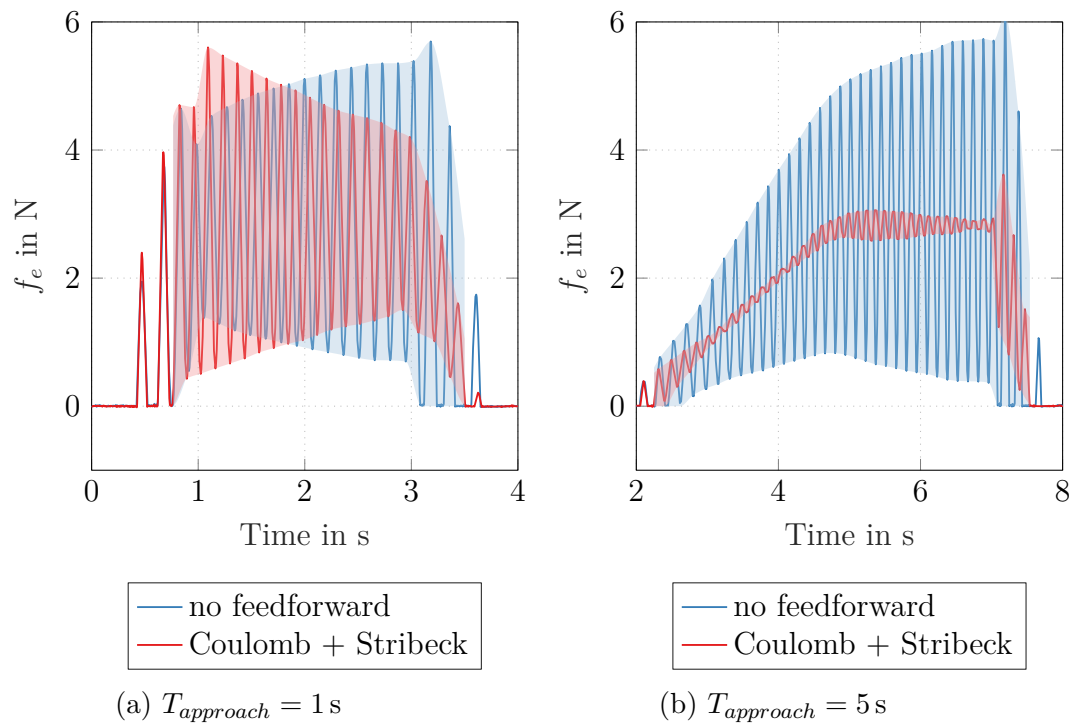
Figure 6.11: Admittance control behaviour in contact with a steel spring with and without friction feedforward in the inner control loop. The behaviour for the first impact is the same for both configurations, but without friction feedforward the oscillation amplitude swings up in contact.

(a) $T_{approach} = 1\,\mathrm{s}$ (b) $T_{approach} = 5\,\mathrm{s}$
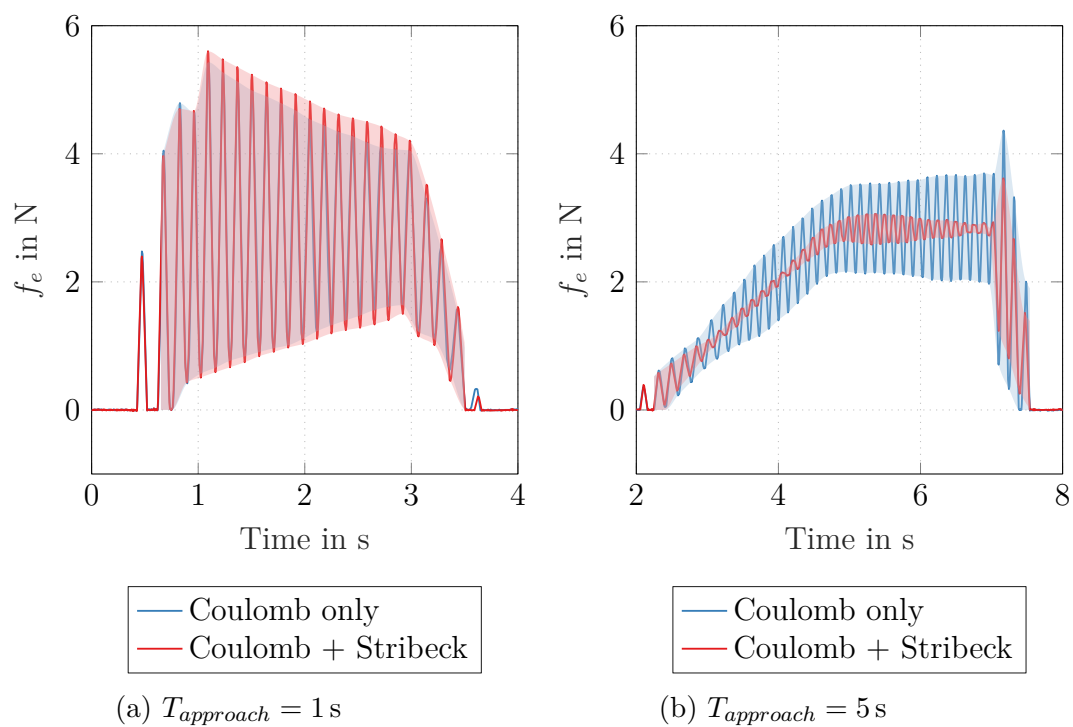
Figure 6.12: Influence of different static friction compensation methods on the admittance control performance at different approaching speeds. If the oscillation amplitudes are large as in (a), both approaches perform very similar. If the impact velocity is decreased, only feedforwarding Coulomb friction causes a limit cycle with larger amplitude as is Coulomb and Stribeck friction is fed forward. (See Figure 6.7b for a simulation of the ideally coupled case)
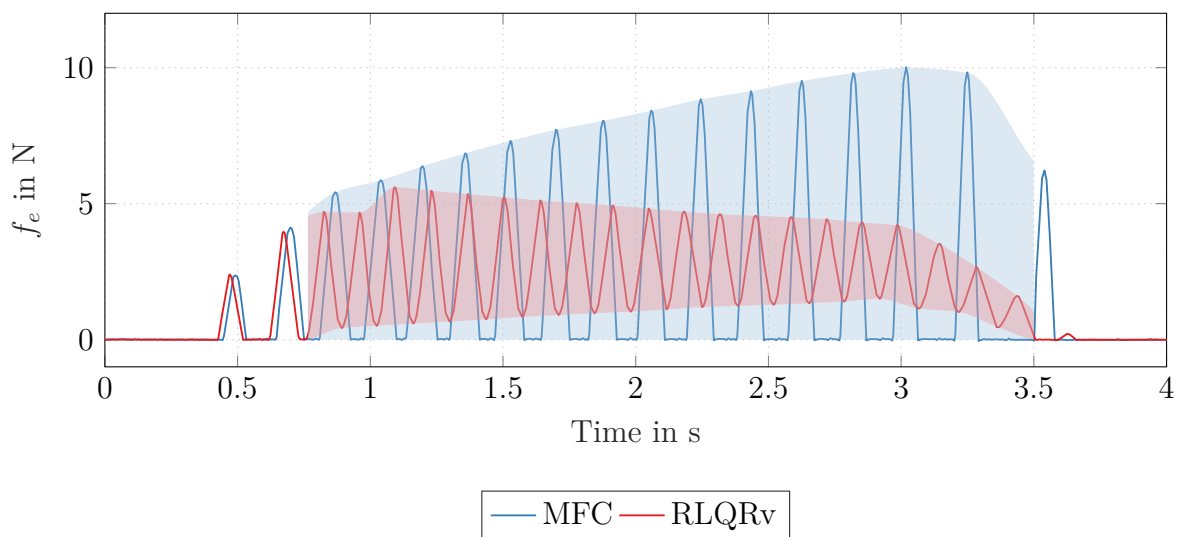
Figure 6.13: Admittance control performance when a MFC serves as position controller instead of the RLQRv. $k_e = 2\,\mathrm{kN/m}$ and $T_{approach} = 5\,\mathrm{s}$ in this case. With the MFC, no stable interaction can be established, whereas with the RLQGv closed loop dynamics are close to the ideal solution (see Figure 6.8).

measurement available and has to rely on position feedback only. Furthermore, it compensates for disturbances via an integrator in the controller transfer function compared to the feedforward compensator of the RLQRv. One obvious disadvantage of this setup is that it cannot prevent the linear motor from getting stuck, because it has to occur first, before the integrator term can start to correct the deviation from the nominal trajectory. Apart from this drawback, the MFC performs as well as the RLQRv without friction compensation in following position trajectories with respect to the reference model. Figure 6.13 shows the measured contact for an interaction experiment with the same parameters as in Section 6.2.1. Surprisingly, if the MFC is used as position controller, the closed loop is unstable, although the manipulator behaves according reference model. This behaviour might be triggered by the integrator which is coupled into the interaction control loop as soon as the contact is established. This experiment leads to the conclusion that the choice of the inner loops control algorithm can have a huge impact on the interaction control performance.

6.2.3 Adaptive Admittance Controller

Section 6.2.1 showed that limitations in the position tracking ability of the linear motor distort the interaction control performance of the test rig. For environments which are
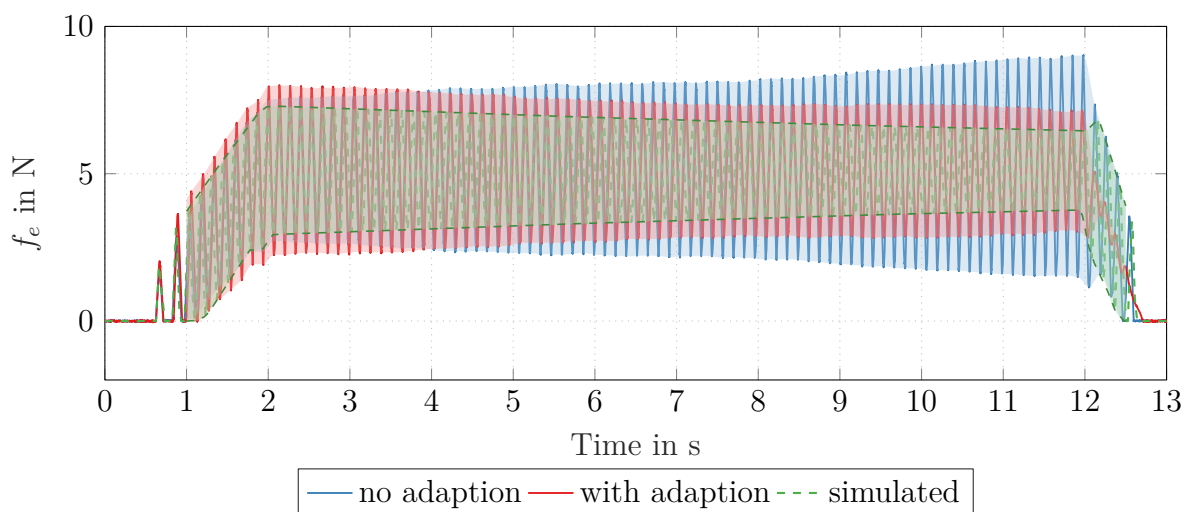
Figure 6.14: Verification of the stabilizing effect of the AAC, when in contact
with an environment with $k_e = 2\,\mathrm{kN/m}$. For this experiment the
VE damping factor $d_t = 0.1\,\mathrm{Ns/m}$ is chosen. While the closed-
loop is unstable with the traditional admittance control law, it
can be stabilized with the adaptive control law. With both ap-
proaches, the oscillations in closed-loop are larger that expected
from a simulation.

close to the stability limit, disturbances caused by tracking cannot be distinguished
from other error sources. In order to prove the concept of the adaptive admittance
control approach, the maximum environment stiffness that results in stable coupling,
should be in a range, where motion tracking problems are not an issue. Therefore, in
this section, the VE damping parameter is lowered to $d_t = 0.1\,\mathrm{Ns/m}$, which limits the
stable environment range to $k_e \leq 1\,\mathrm{kN/m}$.

Figure 6.14 shows the force for an interaction experiment with $k_e = 2\,\mathrm{kN/m}$ and
$T_{approach} = 1\,\mathrm{s}$. It is obvious that without adaption of the control law, the amplitude of
the force oscillaitions increases over time, whereas it decreases when using the adaptive
control law. Compared to the simulation the measured force oscillations are larger in
amplitude. It has to be mentioned that it is very difficult to emulate VEs with such little
damping on this particular test rig. This is because imperfect friction compensation
and material damping affect the achieved trajectory more, when the desired damping
by the VE is small.

Chapter 7

Resumee and Outlook

The previous chapters showed, that of the two indirect force control approaches impedance- and admittance control, the latter is the most promising candidate for implementation in a mechanical HiL application. Reasons include more freedom of design to chose environment dynamics and the possibility to account for disturbances that act on the manipulator, such as friction. Drawbacks are high demands on the motion control loop and possible instability due to non-passive behaviour of the digital controller. Both problems have been accounted for in this thesis.

A state-space reference model following control structure proved to be an optimal approach to be implemented as position controller for a linear motor which is subject to considerable friction forces. It offers the possibility to incorporate velocity measurements as well as friction feedforward compensation methods. Fusion of an acceleration sensor signal with the position measurement provided an accurate synthesized velocity measurement, which drastically improved tracking performance at small velocities.

In order to stabilize the admittance control loop regardless of target dynamics, environment stiffness and sampling time, an adaptive admittance controller was developed. It relies on online estimation of the environment stiffness and updating the discrete admittance controller to achieve ideal coupling.

Interaction experiments with different objects were conducted on a mechanical test rig to evaluate the performance of the developed concepts. As one aspect of this work was to assess the practicability of different control approaches, essential outcomes should be repeated in the following:

- *Impedance control* can be successfully implemented only if the virtual environment dynamics to be realized are in a range to reject disturbances other than arising from coupling with the environment.

- A performant *admittance control* law incorporates the inverse of the position-control loop transfer function, which in turn should be known as exactly as pos-

sible. The most promising approach seems to be to define a desired dynamic behaviour of the inner control loop and subsequently solve the occuring servo problem.

- If the sampling rate is sufficiently high, the performance of the admittance control is limited mainly by the position control loop. Different position-control approaches that nominally yield the same closed-loop tracking dynamics are differently well suited for the task.

- Accurate friction compensation is crucial to obtain stationary contact with an environment. Velocity feedback in combination with a static feedforward compensation yields acceptable performance with parameters that are relatively easy to identify. Position feedback alone is insufficient because of the large lag between disturbance input and measurement.

Despite the VE in the experiments being only of second-order, the presented approach can easily be expanded to arbitrarily large linear transfer functions, for example one resulting from finite element modelling. This provides a starting point for future work on this topic. Theory shows that it is of utter importance to include the inverse of the position control transfer function in the admittance control law to ensure stable interaction. An interesting question is, how the proposed control framework can be extended to nonlinear VEs. As VE models can be complex and time consuming, future work could also cover the application of this approach in a multi-rate system, where some parts of the VE are simulated with different sampling rates.

Appendix A

Additional Derivations

A.1 Admittance Controller Stability Considerations

To investigate the the closed loop stability properties of the admittance control law

$$G_{ad}(z) = \frac{G_{ve}(z)}{G_m(z)} \tag{A.1}$$

it is assumed that the linear motor is in contact with an environment, which can be represented by a linear transfer function $G_e(s)$.

The closed loop system has then a structure as shown in Figure 4.2. $G_m(z)$ is the reference model transfer function to which the linear motor is controlled. $G_m(z)$ as well as $G_{ad}(z)$ and $G_e(s)$ are assumed to be stable. The time discrete transfer function from the reference input $x_{r,k}$ to the linear motor position x_k can then be derived:

$$
\begin{aligned}
T_{x_r,x}(z) &= \frac{G_m(z)}{1 + G_{ad}(z)G_m(z)G_e(z)} \\
&= \frac{G_m(z)}{1 + \frac{G_{ve}(z)}{G_m(z)}G_m(z)G_e(z)} \\
&= \frac{G_m(z)}{1 + G_{ve}(z)G_e(z)} \\
&= \frac{n_m(z)}{d_m(z)\left(1 + \frac{n_{ve}(z)}{d_{ve}(z)}\frac{n_e(z)}{d_n(z)}\right)} \\
&= \frac{n_m(z)d_{ve}(z)d_e(z)}{d_m(z)\left(d_{ve}(z)d_e(z) + n_{ve}(z)n_e(z)\right)} \quad .
\end{aligned}
\tag{A.2}
$$

$n(z)$ and $d(z)$ represent the numerator and the denominator polynomials of the corresponding transfer functions. The closed loop system is stable, if all poles of the

denominator polynomial of $T_{x_r,x}(z)$ lie within the unit circle.From the last line of (A.2) it can be seen that $d_m(z)$ can be separated and stability depends only on the polynomial

$$d_{ve}(z)d_e(z) + n_{ve}(z)n_e(z) \quad , \tag{A.3}$$

which consists of VE parameters and parameters of the generally unknown real environment. If $G_e(z)$ is known, Lemma A.1 provides a necessary condition for a quick check, if the system is stable. A *necessary and sufficient* numerical stability condition is given by *Jury's Stability Criterion* [52, pp. 81-82].

Lemma A.1 (Necessary stability condition for discrete systems)**.** *Given the denominator polynomial of a discrete closed loop system* $d(z) = a_n z^n + a_{n-1} z^{n-1} \ldots a_1 z + a_0$ *is known. Based on* Vieta's formulas*, a necessary condition for the stability of the closed loop system can be formulated.*

$$\prod_{i=1}^{n}(z - z_i) = z^n + (z_1 + z_2 + \ldots + z_n)z^{n-1} + \cdots + z_1 z_2 \ldots z_{n-1}z_n \tag{A.4a}$$

$$= a_n z^n + a_{n-1} z^{n-1} \ldots a_1 z + a_0 \tag{A.4b}$$

In (A.4) *is assumed that all poles are* real *or occur in* complex conjugated pairs. *Comparing the two lines of* (A.4) *shows that the coefficient* a_0 *is the product of all the zeros of* $d(z)$. *A necessary condition that all poles of* $d(z)$ *lie within the unit circle is given with*

$$\left| \frac{a_0}{a_n} \right| = \prod_{i=1}^{n} z_i < 1 \quad . \tag{A.5}$$

Proof. If $\prod_{i=1}^{n} z_i \geq 1$, then there must be one or more zeros z_i with $|z_i| \geq 1$ and the system is unstable. But (A.5) might still be fulfilled if one or more z_i lie outside of the unit circle. Therefore Lemma A.1 provides only a *necessary* condition. □

In the following, the results are specialized for the admittance controller of Section 4.4 and an ideal stiffness k_e as an environment. With these assumptions made, (A.3) reduces to

$$d_{ve}(z) + n_{ve}(z)k_e \quad . \tag{A.6}$$

When $G_{ve}(s)$ is discretized, its poles are mapped to the poles of $G_{ve}(z)$ via

$$z = e^{(s+i\omega)T_a} = e^{sT_a}e^{\omega T_a} = e^{sT_a}\left[\cos(\omega) + i\sin(\omega)\right] \tag{A.7}$$

$G_{ve}(s)$ in (4.3) is of order two with poles that are calculated to

$$s_{1/2} = \frac{-d_t \pm \sqrt{d_t^2 - 4m_t(k_t + k_e)}}{2m_t} \quad . \tag{A.8}$$

Therefore $n_{ve}(z)$ can be represented as a polynomial of order two with complex conjugated zeroes:

$$d_{ve}(z) = (z + \underline{z}_{z,1})(z + \underline{z}_{z,2}) \qquad , \underline{z}_{z,1/2} = v_z \pm i v_{z,i} \qquad (A.9)$$

The property of stability is not lost under discretization and so $G_{ve}(z)$ must be stable as well.

The numerator polynomial $n_{ve}(z)$ is dependent on the discretization method and therefore cannot be determined so easy. For example using *zero-order hold* discretization, the order of the numerator is one less than the order of the denominator and $n_{ve}(z)$ takes the form

$$n_{ve}(z) = n_1 z + n_0 \quad . \qquad (A.10)$$

As mentioned, other forms are possible, but as the continuous system is causal, the discrete system must be causal as well, i.e. the order of $n_{ve}(z)$ must not exceed the order of $d_{ve}(z)$. So the most general form of the possible numerator polynomials is

$$n_{ve}(z) = n_2 z^2 + n_1 z + n_0 \quad , \qquad (A.11)$$

which we will use for further investigation.

Substituting (A.11) and (A.9) in (A.6) yields

$$(1 + n_2 k_e)z^2 + (n_1 k_e + \underline{z}_{z,1} + \underline{z}_{z,2})z + (\underline{z}_{z,1}\underline{z}_{z,1} + n_0 k_e) \quad , \qquad (A.12)$$

and applying Lemma A.1 to obtain the necessary stability condition

$$\underline{z}_{z,1}\underline{z}_{z,2} + n_0 k_e < 1 \quad . \qquad (A.13)$$

As the poles $\underline{z}_{z,i}$ and n_0 depend on the VE dynamics and the sampling time, with A.13 it is possible to quantify a value of k_e, for which the admittance control will fail for sure. If for the target dynamics $d_t < 2\sqrt{k_t m_t}$ holds, then $\underline{z}_{z,1} = \underline{z}_{z,2}$ and (A.13) becomes

$$|\underline{z}_z|^2 + n_0 k_e < 1 \quad . \qquad (A.14)$$

In this case, (A.13) is a *necessary* and *sufficient* condition for stability of the interaction control loop.

Appendix B

Parameters

Linear Motor

Parameter	Value	Description
m_{slider}	$0.34\,\mathrm{kg}$	slider mass
m_{shaft}	$0.86\,\mathrm{kg}$	combined shaft masses
m_{mag}	$0.52\,\mathrm{kg}$	magnetic spring moving mass
K_i	$9.68\,\mathrm{N/A}$	force constant
d	$21.12\,\mathrm{Ns/m}$	viscous friction parameter

Table B.1: Linear motor parameters

Control Parameters

Parameter	Value	Description
f_g	$1.3705\,\mathrm{N}$	constant disturbance force
f_c	$3.74\,\mathrm{N}$	Coulomb friction parameter
$f_{s,a}$	$4.3071\,\mathrm{N}$	Stribeck friction parameter
v_s	$0.0095\,\mathrm{m/s}$	Stribeck velocity
k_{tan}	$2500\,\mathrm{s/m}$	tangens smoothing function coefficient

Table B.2: Friction parameters

Parameter	Value	Description
T_s	0.2 ms	sampling time
$\omega_m/2\pi$	19 Hz	reference model crossover frequency
ξ_m	0.95	reference model damping factor
$\mathbf{k}^{\mathrm{T}}$	$\begin{bmatrix} -9.45 \cdot 10^3 & -95.88 \end{bmatrix}$	feedback vector
r_m	$2.47 \cdot 10^3$	feedforward parameter
$\bar{\mathbf{c}}_m^{\mathrm{T}}$	$\begin{bmatrix} -103.85 & 105.23 \end{bmatrix}$	transformed reference model output vector

Table B.3: RLQG controller parameters

Parameter	Value	Description
T_s	0.2 ms	sampling time
m_t	1 kg	target mass
d_t	1 Ns/m	target damping factor
k_t	100 N/m	target stiffness

Table B.4: Virtual environment parameters

Parameter	Value	Description
$\omega_m/2\pi$	19 Hz	reference model crossover frequency
ξ_m	0.95	reference model damping factor
z_o	$\{0.955, 0.945\}$	observer polynomial poles
$G_r(z)$	$10^4 \frac{2.429 - 4.803 z^{-1} + 2.374 z^{-2}}{1 - 1.870 z^{-1} + 0.870 z^{-2}}$	feedback controller transfer function
$G_{pf}(z)$	$\frac{1}{10^4} \frac{2.429 - 4.803 z^{-1} + 2.374 z^{-2}}{2184 - 4171 z^{-1} + 1991 z^{-2}}$	pre-filter transfer function

Table B.5: Model Following Controller

Bibliography

[1] M. Bacic. On hardware-in-the-loop simulation. In *Proceedings of the 44th IEEE Conference on Decision and Control*, pages 3194–3198, December 2005.

[2] L. Allen. Evolution of flight simulation. American Institute of Aeronautics and Astronautics, August 1993.

[3] J. Bélanger, P. Venne, and J.-N. Paquin. The what, where, and why of real-time simulation. *Planet RT*, pages 37–49, January 2010.

[4] R. Isermann, J. Schaffnit, and S. Sinsel. Hardware-in-the-loop simulation for the design and testing of engine-control systems. *Control Engineering Practice*, 7(5):643–653, May 1999.

[5] O. Gietelink, J. Ploeg, B. De Schutter, and M. Verhaegen. Development of advanced driver assistance systems with vehicle hardware-in-the-loop simulations. *Vehicle System Dynamics*, 44(7):569–590, July 2006.

[6] R. Priesner and S. Jakubek. Mechanical Impedance Control of Rotatory Test Beds. *IEEE Transactions on Industrial Electronics*, 61(11):6264–6274, November 2014.

[7] O. Konig, C. Hametner, G. Prochart, and S. Jakubek. Battery Emulation for Power-HIL Using Local Model Networks and Robust Impedance Control. *IEEE Transactions on Industrial Electronics*, 61(2):943–955, February 2014.

[8] G. Aschauer, A. Schirrer, M. Kozek, and S. Jakubek. Realtime-capable FE-based railway catenary emulation via pantograph test rig impedance control. *IFAC-PapersOnLine*, 50(1):8636–8641, July 2017.

[9] A. Facchinetti and S. Bruni. Hardware-in-the-loop hybrid simulation of pantograph–catenary interaction. *Journal of Sound and Vibration*, 331(12):2783–2797, June 2012.

[10] J. N. Verhille, A. Bouscayrol, P. J. Barre, and J. P. Hautier. Hardware-in-the-loop simulation of the traction system of an automatic subway. In *2007 European Conference on Power Electronics and Applications*, pages 1–9, September 2007.

[11] M. Kabutomori, T. Murai, S. Ota, and Y. Terumichi. Development of a test stand for Maglev vehicles using hardware-in-the-loop simulation. In *2017 11th International Symposium on Linear Drives for Industry Applications (LDIA)*, pages 1–5, September 2017.

[12] C. H. Chang, E. C. Chang, and H. L. Cheng. A High-Efficiency Solar Array Simulator Implemented by an LLC Resonant DC #x2013;DC Converter. *IEEE Transactions on Power Electronics*, 28(6):3039–3046, June 2013.

[13] A. Bouscayrol. Different types of Hardware-In-the-Loop simulation for electric drives. In *2008 IEEE International Symposium on Industrial Electronics*, pages 2146–2151, June 2008.

[14] A. Schirrer, G. Aschauer, E. Talic, M. Kozek, and S. Jakubek. Catenary emulation for hardware-in-the-loop pantograph testing with a model predictive energy-conserving control algorithm. *Mechatronics*, 41(Supplement C):17–28, February 2017.

[15] H. Gürocak. *Industrial Motion Control: Motor Selection, Drives, Controller Tuning, Applications.* John Wiley & Sons, Ltd, Chichester, UK, September 2015.

[16] C. C. de Wit, H. Olsson, K. J. Astrom, and P. Lischinsky. A new model for control of systems with friction. *IEEE Transactions on Automatic Control*, 40(3):419–425, March 1995.

[17] W. Townsend and J. Salisbury. The Effect of coulomb friction and stiction on force control. In *1987 IEEE International Conference on Robotics and Automation Proceedings*, volume 4, pages 883–889, March 1987.

[18] B. Armstrong-Helouvry. *Control of Machines with Friction.* Kluwer Academic Publishers, Boston, MA, 1991. OCLC: 863792163.

[19] C. Iurian, F. Ikhouane, J. Rodellar Benedé, and R. Griñó Cubero. Identification of a system with dry friction. Technical report, September 2005.

[20] H. Olsson, K. J. Åström, C. Canudas de Wit, M. Gäfvert, and P. Lischinsky. Friction Models and Friction Compensation. *European Journal of Control*, 4(3):176–195, January 1998.

[21] M. R. Kermani, R. V. Patel, and M. Moallem. Friction Identification and Compensation in Robotic Manipulators. *IEEE Transactions on Instrumentation and Measurement*, 56(6):2346–2353, December 2007.

[22] L. Freidovich, A. Robertsson, A. Shiriaev, and R. Johansson. LuGre-Model-Based Friction Compensation. *IEEE Transactions on Control Systems Technology*, 18(1):194–200, January 2010.

[23] M. Iwasaki, T. Shibata, and N. Matsui. Disturbance-observer-based nonlinear friction compensation in table drive system. *IEEE/ASME Transactions on Mechatronics*, 4(1):3–8, March 1999.

[24] J.-S. Mo, Z.-C. Qiu, J.-C. Wei, and X.-M. Zhang. Adaptive positioning control of an ultrasonic linear motor system. *Robotics and Computer-Integrated Manufacturing*, 44:156–173, April 2017.

[25] D. P. Hess and A. Soom. Friction at a Lubricated Line Contact Operating at Oscillating Sliding Velocities. *Journal of Tribology*, 112(1):147, 1990.

[26] J. A. Nelder and R. Mead. A Simplex Method for Function Minimization. *The Computer Journal*, 7(4):308–313, January 1965.

[27] A. Haddadi and K. Hashtrudi-Zaad. Online contact impedance identification for robotic systems. In *2008 IEEE/RSJ International Conference on Intelligent Robots and Systems*, pages 974–980, September 2008.

[28] D. Erickson, M. Weber, and I. Sharf. Contact Stiffness and Damping Estimation for Robotic Systems. *The International Journal of Robotics Research*, 22(1):41–57, January 2003.

[29] K. H. Hunt and F. R. E. Crossley. Coefficient of Restitution Interpreted as Damping in Vibroimpact. *Journal of Applied Mechanics*, 42(2):440–445, June 1975.

[30] D. J. Park and B. E. Jun. Selfperturbing recursive least squares algorithm with fast tracking capability. *Electronics Letters*, 28(6):558–559, March 1992.

[31] B. Siciliano and O. Khatib, editors. *Springer handbook of robotics*. Springer, Berlin, 2008. OCLC: ocn153562054.

[32] M. H. Raibert and J. J. Craig. Hybrid Position/Force Control of Manipulators. *Journal of Dynamic Systems, Measurement, and Control*, 103(2):126, 1981.

[33] J. J. Craig and M. H. Raibert. A systematic method of hybrid position/force control of a manipulator. In *Computer Software and Applications Conference, 1979. Proceedings. COMPSAC 79. The IEEE Computer Society's Third International*, pages 446–451, 1979.

[34] J. K. Salisbury. Active stiffness control of a manipulator in cartesian coordinates. In *1980 19th IEEE Conference on Decision and Control including the Symposium on Adaptive Processes*, pages 95–100, December 1980.

[35] S. Stramigioli. *Modeling and IPC control of interactive mechanical systems: a coordinate-free approach*. Number 266 in Lecture notes in control and information sciences. Springer, London : New York, 1st ed edition, 2001.

[36] N. Hogan. Impedance Control: An Approach to Manipulation: Part II—Implementation. *Journal of Dynamic Systems, Measurement, and Control*, 107(1):8–16, March 1985.

[37] C Ott, R. Mukherjee, and Y. Nakamura. Unified impedance and admittance control. In *Robotics and Automation (ICRA), 2010 IEEE International Conference on*, pages 554–561. IEEE, 2010.

[38] N. Hogan. Impedance Control: An Approach to Manipulation: Part I—Theory. *Journal of Dynamic Systems, Measurement, and Control*, 107(1):1–7, March 1985.

[39] A. Bemporad, G. Bianchini, F. Brogi, and G. Chesi. Passivity analysis of discrete-time hybrid systems using piecewise polynomial storage functions. In *Decision and Control, 2005 and 2005 European Control Conference. CDC-ECC'05. 44th IEEE Conference on*, pages 5421–5426. IEEE, 2005.

[40] A. Bemporad, G. Bianchini, F. Brogi, and F. Barbagli. PASSIVITY ANALYSIS AND PASSIFICATION OF DISCRETE-TIME HYBRID SYSTEMS. *IFAC Proceedings Volumes*, 38(1):391–396, January 2005.

[41] A. Bemporad, G. Bianchini, and F. Brogi. Passivity Analysis and Passification of Discrete-Time Hybrid Systems. *IEEE Transactions on Automatic Control*, 53(4):1004–1009, May 2008.

[42] M. Vukobratović, editor. *Dynamics and robust control of robot-environment interaction*. Number v. 2 in New frontiers in robotics. World Scientific Pub, Hackensack, NJ, 2009. OCLC: ocn236336337.

[43] C. Ott, R. Mukherjee, and Y. Nakamura. A Hybrid System Framework for Unified Impedance and Admittance Control. *Journal of Intelligent & Robotic Systems*, 78(3-4):359–375, June 2015.

[44] J. E. Colgate and G. Schenkel. Passivity of a class of sampled-data systems: Application to haptic interfaces. In *American Control Conference, 1994*, volume 3, pages 3236–3240. IEEE, 1994.

[45] S. Stramigioli, C. Secchi, A. J. van der Schaft, and C. Fantuzzi. A novel theory for sampled data system passivity. In *IEEE/RSJ International Conference on Intelligent Robots and Systems*, volume 2, pages 1936–1941 vol.2, 2002.

[46] Hassan K. Khalil. *Nonlinear systems*. Prentice Hall, Upper Saddle River, N.J, 3rd ed edition, 2002.

[47] B. Hannaford and J-H. Ryu. Time-domain passivity control of haptic interfaces. *IEEE Transactions on Robotics and Automation*, 18(1):1–10, February 2002.

[48] Jee-Hwan Ryu, Yoon Sang Kim, and B. Hannaford. Sampled- and continuous-time passivity and stability of virtual environments. *IEEE Transactions on Robotics*, 20(4):772–776, August 2004.

[49] J.-P Kim and J. Ryu. Stable haptic interaction control using energy bounding algorithm. In *Intelligent Robots and Systems, 2004.(IROS 2004). Proceedings. 2004 IEEE/RSJ International Conference on*, volume 2, pages 1210–1217. IEEE, 2004.

[50] J.-P. Kim and J. Ryu. Robustly Stable Haptic Interaction Control using an Energy-bounding Algorithm. *The International Journal of Robotics Research*, 29(6):666–679, May 2010.

[51] S. Kim, J.-P. Kim, and J. Ryu. Adaptive Energy-Bounding Approach for Robustly Stable Interaction Control of Impedance-Controlled Industrial Robot With Uncertain Environments. *IEEE/ASME Transactions on Mechatronics*, 19(4):1195–1205, August 2014.

[52] K. J. Åström and B. Wittenmark. *Computer-controlled systems : theory and design (3 ed.)*. Prentice-Hall, 1997.

[53] J. Lunze. *Regelungstechnik 2*. Springer-Lehrbuch. Springer Berlin Heidelberg, Berlin, Heidelberg, 2014.

[54] PCB Piezotronics. Model TLA288d01 Mechanical Impedance Sensor - Installation and Operating Manual.

[55] PCB Piezotronics. Model 482c05 Four-channel, ICP® Sensor Signal Conditioner - Installation and Operating Manual.

[56] W. H. Zhu and T. Lamarche. Velocity Estimation by Using Position and Acceleration Sensors. *IEEE Transactions on Industrial Electronics*, 54(5):2706–2715, October 2007.

[57] A. Savitzky and M. J. E. Golay. Smoothing and Differentiation of Data by Simplified Least Squares Procedures. *Analytical Chemistry*, 36(8):1627–1639, July 1964.

Eidesstattliche Erklärung

Ich erkläre eidesstattlich, dass ich die Arbeit selbständig angefertigt, keine anderen als die angegebenen Hilfsmittel benutzt und alle aus ungedruckten Quellen, gedruckter Literatur oder aus dem Internet im Wortlaut oder im wesentlichen Inhalt übernommenen Formulierungen und Konzepte gemäß den Richtlinien wissenschaftlicher Arbeiten zitiert, durch Fußnoten gekennzeichnet bzw. mit genauer Quellenangabe kenntlich gemacht habe.

Wien, am 20. April   2018

_____
Daniel Duller